International
Progress Report

IPR-02-31

Äspö Hard Rock Laboratory

True Block Scale project

Stochastic continuum modelling of flow and transport

J. Jamie Gómez-Hernández
Harrie-Jan Hendricks Franssen
Technical University of Valencia (UPV), Spain

Agustín Medina Sierra
Amaranta Marcuello
Jesús Carrera
Daniel Sendrós
Technical University of Barcelona (UPC), Spain

December 2002

Svensk Kärnbränslehantering AB
Swedish Nuclear Fuel
and Waste Management Co
Box 5864
SE-102 40 Stockholm Sweden
Tel +46 8 459 84 00
Fax +46 8 661 57 19

Äspö Hard Rock
Laboratory

Report no.
IPR-02-31
No.
F56K
Author
J. Jaime Gómez-Hernández
Harrie-Jan Hendricks Franssen
Agustín Medina Sierra
Amaranta Marcuello
Jesús Carrera
Daniel Sendrós
Date
Dec 2002
Checked by
Anders Winberg
Date
2003-03-14
Approved
Christer Svemar
Date
2003-12-16

Äspö Hard Rock Laboratory

True Block Scale project

Stochastic continuum modelling of flow and transport

J. Jamie Gómez-Hernández
Harrie-Jan Hendricks Franssen
Technical University of Valencia (UPV), Spain

Agustín Medina Sierra
Amaranta Marcuello
Jesús Carrera
Daniel Sendrós
Technical University of Barcelona (UPC), Spain

December 2002

Keywords: Conditional, continuum, coupling, realisations, sequential, solute, stochastic, transport

Abstract

This technical report describes the implementation of a stochastic continuum flow and transport model at the True Block Scale site. The main objective during the building of this model was to assess whether such a model could be built conditional to the available data including geometrical data, material parameter data and pressure responses.

The conclusion is that a stochastic continuum model can be built and the building process may help in understanding the role that the identified features play in the hydraulic behaviour of the site.

Sammanfattning

Denna tekniska rapport beskriver implementeringen av en stokastisk kontinuum modell av flöde och transport i den undersökta TRUE Block Scale volymen. Det huvudsakliga syftet under byggandet av modellen var att undersöka om en sådan modell kunde konstrueras betingad av tillgängliga data, inkluderande geometrisk information, materialegenskaper och tryckdata.

Slutsatsen är att en stokastisk kontinuum modell kan byggas och att konstruktionsprocessen kan bidra till ökad förståelse av den hydrauliska roll som olika strukturer spelar i den undersökta bergvolymen.

Executive Summary

This report presents a stochastic continuum flow and transport model of the TRUE Block Scale site at a scale of hundreds of metres. The flow model consists of a lattice of cubic blocks discretizing a volume centred at the potential location of the in situ tracer retention experiments.

The flow model has been built in a sequential manner. First the main structural features represented in the so-called October'97 hydrostructural model, are used to classify the model blocks including structures and not including structures (rock mass and existing background fractures). Then, the material properties measured or interpreted from hydraulic tests are assigned to the corresponding discretization blocks. Later, within each structure, the conductivity values are randomly generated using a conditional stochastic simulation approach in which spatial correlation is accounted for, and measured values are honoured. Finally, the resulting 3-D heterogeneous block of conductivities is perturbed until, first, the undisturbed heads and, second, the transient pressure responses, observed in the borehole piezometers are matched by the results of the numerical simulation of steady-state and transient flow within the simulation domain. For the latter step, boundary conditions are necessary, which are taken from a regional model of the site.

The above procedure can be repeated for several realisations for which the classification into blocks including structures and not including structures remains unaltered, but the conductivity distribution varies from one realisation to another. The process is computer intensive and only one realisation is presented and discussed.

After assessing the feasibility of such a model, the September'98 hydrostructural model together with the results from the interference tests carried out during the spring of 1998 were used to build a first conditional model fully based on quantitative data.

From the flow model based on the September'98 hydrostructural model, it was concluded that a stochastic continuum model conditioned to all the information described above can be built. The sequential nature of the conditioning process helps in understanding the implications that the observed pressure responses have on the hydraulic conductivity of the different structures. It may also help in detecting the need of including additional structures in the hydrostructural model in order to achieve the best reproduction of the observed pressure data.

Subsequent flow models were built as the hydrostructural model evolved, and more information on transient piezometric head evolution was available, more precisely two new calibration rounds were performed using the March'99 and March'00 hydrostructural models. The most important modifications in these two new calibration rounds were the inclusion of structures #21 and #22, and the use of the detailed hydraulic conductivity information derived using the POSIVA flow log tool.

Solute transport is assumed to take place in both, structure planes (defined in the structural model) and background fractures. The transport model is based on the flow model, so it also assumes that heterogeneity in the medium plays a basic role. Transport processes considered are dispersion, diffusion, sorption, first order decay, sink and sources.

Since the flow model is stochastic and produces multiple realisations consistent with hydraulic conductivity data and piezometric data, the transport model has been built using five of the conductivity fields provided. The transport model is smaller in size than the flow model. Because of this, the flow boundary conditions in the transport model are taken directly from the flow model.

The main difference between the flow and transport models stands on the numerical approach used to discretized the state equations. While the flow model uses finite differences, the transport model uses finite elements. This difference require a careful coupling between the two models, because both the size and shape of the elements are different. To solve this problem, an interface was developed to couple the flow model (hydraulic conductivities and boundary heads) with the transport model. The interfacing, however, leads to some smoothing of the conductivity field.

The transport model has evolved as new tracer tests were planned, and then performed. It starts with the predictions of phases A4 and A5. For these predictions, the initial transport parameters were obtained from the calibration of one of the preliminary tracer tests, tracer test PT-4. The predictions of phases A4 and A5 had different degrees of success; however, the knowledge gained in these predictions and its posterior calibration, together with all the information gather in the phase B tests, were used to adjust the transport parameters to finally make the predictions and posterior evaluation of phase C sorbing tracer tests.

The main conclusions from the transport model are that it has been possible to couple a finite difference flow model and a finite element transport, and that the resulting transport model can obtain in some cases reliable predictions.

Contents

List of Figures

List of Tables

1 Introduction

This report describes the work carried out for the stochastic continuum modelling of the in situ TRUE Block experiments. Stochastic continuum modelling of a fracture site is especially attractive for the ease with which different types of information regarding geometry, material properties and pressure response can be brought into the model. Incorporating the different types of information is done in a sequential manner that permits the analysis of the influence of the additional information on the material properties and flow behaviour of the block. In addition, the stochastic nature of the approach allows the analysis of the uncertainty associated with the imperfect knowledge of the medium being modelled.

The report is organised in two distinct sections, the first section is devoted to flow modelling and the second one to transport modelling. In the flow section, the feasibility of building a conditional stochastic continuum model is demonstrated, showing the sequential approach to conditioning, and how the addition of new information modifies the understanding and heterogeneity representation within the flow model.

The second section of the report is devoted to the transport model. This section is organised in four chapters. The first one is related to the assumptions of the transport model and its data needs. It is also briefly described the evolution of the model through the different phases of the True Block Scale project and the approximations that have been used.

The second section is related to the phase C blind predictions. One of the advantages of the stochastic continuum model is its ability to produce alternative representations of the flow parameters consistent with the input data. These alternative representations may be used to obtain confidence intervals and other statistical information on the model predictions. In this report only five realizations have been used to model transport. As shown in the evaluation section, even though all the conductivity fields represent adequately the flow data, their transport behaviour can be very different.

In the initial prediction phases, we did not include matrix diffusion processes in our model. However, we later thought that diffusion in the matrix may have an important effect in the transport of sorbing tracers. For this reason, we defined an “effective retention” parameter obtained with the help of a semianalytical code that includes matrix diffusion process. In addition, we made use of this semianalytical code to make also predictions, so we have two sets of predictions, one using the finite element code (with a heterogeneous field) and the other one using the semianalitycal code. As we discuss later, the fits are really similar, but one expects the heterogeneous model to fit better the “reality”, because it includes more information related to the site.

In the last chapter, we present the evaluation results using the three-dimensional finite element model, in which the transport parameters were calibrated using the breakthrough curves form phase C including explicitly the matrix diffusion effects in the model. Finally, some conclusions of the transport model are discussed.

2 Flow model assessment using the Oct'97 hydrostructural model

In this chapter, an assessment of the possibilities of stochastic continuum modelling by the self-calibrated model is carried out. At the time this assessment was done, the October'97 hydrostructural model represented the current combined understanding of the geology and hydrogeology in the modelling area; however, the hydraulic information available in the area of study had been collected as part of the logging activities during the drilling of the boreholes, but no explicit interference testing had been performed. The aims of this preliminary modelling work were:

- to establish a suitable modelling area, large enough for the later modelling of the tracer tests and with a discretization as fine as could be handled by the available computer code
- to evaluate the feasibility of the self-calibrated algorithm in a three-dimensional model with multiple structures and conditional to steady-state and transient piezometric heads
- to gain a preliminary understanding of the hydraulic functioning of the block in the surroundings of the potential tracer test area.

2.1 Model geometry

The model geometry used during the model assessment phase is based on the October'97 hydrostructural model by Hermanson (2001a) and it is slightly different from the model geometry used in the next chapter which benefits from additional hydraulic data and a re-evaluation of the structural model.

2.1.1 Discretization

The area modelled has an extension of 247 m by 227 m by 287 m and is discretized into 37 by 34 by 43 cubic cells of 6.67 m size[1]. The modelled area has been chosen so that all five main boreholes (KA2563A, KA2511A, KA3510A, KI0025F and KI0023B) are completely contained within it. (Boreholes KI0025F02 and KI0025F03, built later, are also included within the model domain). The model extends from 1790 m to 2037 m East, from 7050 m to 7277 m North, and from –570 m to –283 m bottom to top.

[1] The apparently odd choice for the size of the side of the discretization cells, was due to an initial interest in dividing every 100 m into an exact number of cells, if we chose 10 cells, then the cells were too large, if we chose 20 cells, there were too many cells, so we chose 15 cells, of 100/5 m in the side.

2.1.2 Structures

All structures are included deterministically in the model. For this purpose, each structure is modelled as a plane that is overlaid on the discretized model. Each of the model cells that is intersected by one of the structure planes is classified as including structures. The remaining cells are classified as not including structures. The twenty structures described in the technical report by Hermanson (2001a) have been used for this classification. As a result, 44% of the more than 50,000 cells are intersected by a deterministic structure, and 56% are not. The cells not including structures should not be interpreted as representing the rock matrix but as representing an equivalent medium including the rock matrix and the background fracturing that is not explicitly included in the structural model.

Figure 2-1 and 2-2 show the three-dimensional mask identifying the cells intersected by all deterministic structures. Figure 2-1 shows the intersections of the fracture planes with the faces of the modelled block and Figure 2-2 shows several slices through the 3D mask. The fracture planes, as it can be appreciated from the figures, extend all the way to the boundaries of the block, therefore, enhancing the connectivity compared to that implied by the shorter lengths assigned to the fractures in the October97 model by Hermanson (2001a). This enhanced connectivity will be corrected during the process of pressure conditioning by local modifications of the conductivity values of the cells representing the structure planes.

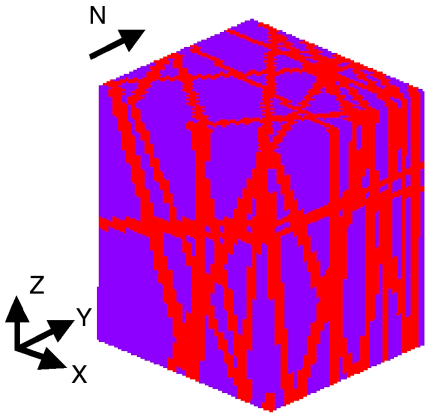

Figure 2-1. *Block mask showing the intersection of the fractures with the block boundaries. Based on the October97 structural model (Hermanson, 2001a).*

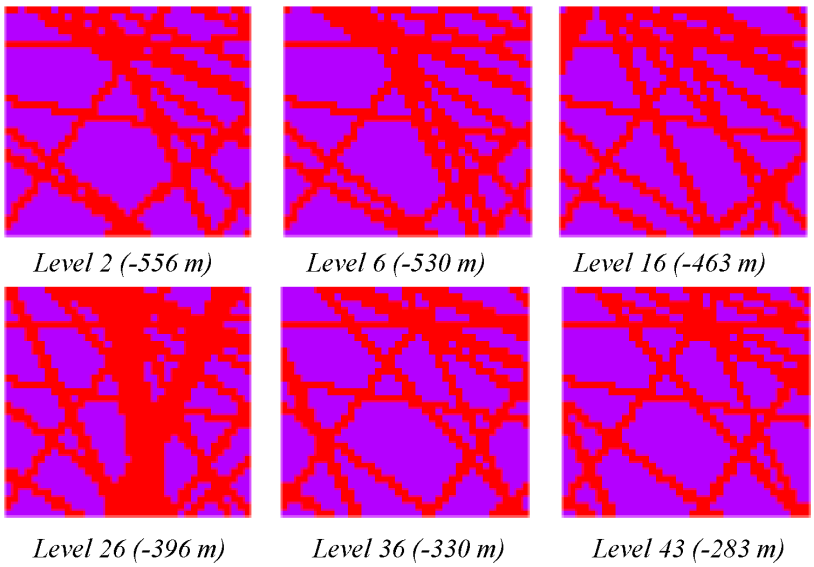

Figure 2-2. *Horizontal slices through the block in Figure 2-1.*

2.2 Material properties

Hydraulic conductivities are assigned to each of the individual structures independently. For each structure, a conditional realisation of conductivities drawn from a multi-lognormal distribution is generated. The conditioning values are derived from the transmissivities measured in the steady state 5 m double packer flow logging, which, in turn were obtained by Moye's formula (e.g., Gentzschein, 2001). These flow log data provide conditioning data at 21 cells in structures and at 101 cells not in structures. Their values are listed in Appendix 1.

The average log conductivity of the cells not in fractures is –10.2 $\log_{10}$ m/s and the variance is 1 $\log^2_{10}$ m/s, whereas in the fractured cells, the average is –6.5 $\log_{10}$ m/s and the variance 0.5 $\log^2_{10}$ m/s.

There were not enough data to compute experimental variograms, therefore, an isotropic spherical variogram was postulated with a range of 40 m. The range was chosen to introduce some continuity within the modelling block, but still being short enough to allow for some heterogeneity in the fracture planes. This range will also play a role during the phase of conditioning to piezometric heads, its value is reasonable to allow the fractures to be locally perturbed to achieve conditioning. Sensitivity tests to the presence of anisotropy and to the variogram range have not been performed.

During the calibration to the transient information, a constant storativity coefficient was used and equal to 2.0E-05. This value was chosen based on our experience from models in similar media and from the response times observed in the interferences observed during drilling.

2.3 Flow simulations

The solution of the groundwater flow equation is obtained by standard seven-point block-centred finite differences using the geometric mean of adjacent cells to compute the intercell hydraulic conductivities. The solution of the linear finite-difference system of nearly 50,000 equations is obtained by biconjungate preconditioned gradient with incomplete LU decomposition (Greenbaum, 1996). This method takes optimal advantage of the sparse nature of the conductance matrix and allows handling of the large conductivity contrasts that appear between adjacent cells. The conductance matrix is, in any case, highly unstable and some implementation refinements had to be performed in order to ensure convergence.

For the steady-state simulation, prescribed head values along the six boundaries of the parallelepiped are imposed. The values used were taken from the regional model by Svensson (1997). They impose an average gradient towards the tunnel galleries of about ten percent. In conjunction with the values taken from the regional model, the cells of the model block that were intersected by the underground openings are assigned a piezometric head corresponding to atmospheric pressure. A view of the prescribed heads on three of the faces of the parallelepiped is given in Figure 2-3.

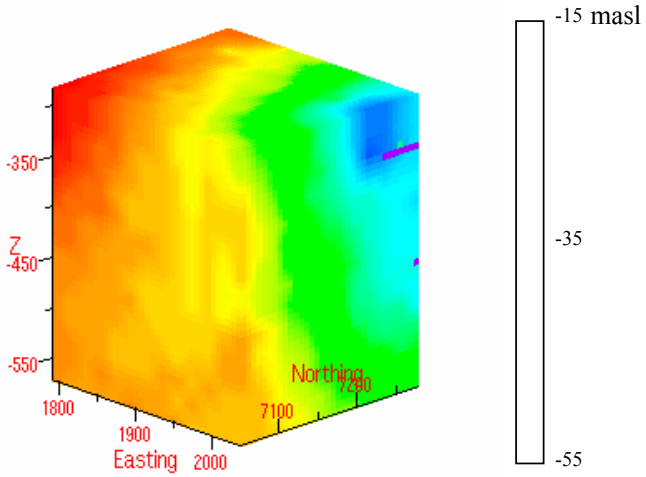

Figure 2-3. *Prescribed heads used as boundary conditions in m as used for the solution of the groundwater flow equation. Tunnel cell values are outside the colour range of the scale.*

2.4 Conditioning to measured piezometric head

The realisation of the conductivity field generated as discussed in section 2.2 will not, in general, reproduce the observed heads at the monitoring locations when the flow equation is solved using the boundary conditions shown in Figure 2-3. In order to condition the conductivity realisation to piezometric heads the self-calibrated algorithm is used (Gómez-Hernández et al., 1997), a perturbation conductivity realisation is computed that added to the seed realisation results in a new realisation in which the solution of the flow equation matches the measured piezometric heads. The perturbation is computed by non-linear optimisation. The details of the calculation can be looked up in the previously referred to paper, although a basic outline of the technique is given in Appendix 2.

Besides its fundamental objective of producing realisations conditional to both transmissivity and head measurements, the self-calibrated algorithm allows assessment of the impact that the conditioning data has on the spatial distribution of hydraulic conductivities. First, a realisation is generated conditional only to conductivity data, then, the realisation can be made conditional to steady-state heads, then it can be made conditional to transient heads including results of one or several interference tests. During the conditioning process, the evolution of the conductivity realisation can be monitored and some considerations can be made about the implications that the observed pressure responses have in internal connectivity of the block.

Figure 2-4 shows a conductivity field built by merging the realisations of hydraulic conductivities on the 20 structure planes with the generated background hydraulic conductivity distribution corresponding to the cells not including structures into a single block. As previously mentioned, this realisation is conditional to the 132 measured log hydraulic conductivity data values but does not take into account the piezometric head information. This field is referred to as the seed field.

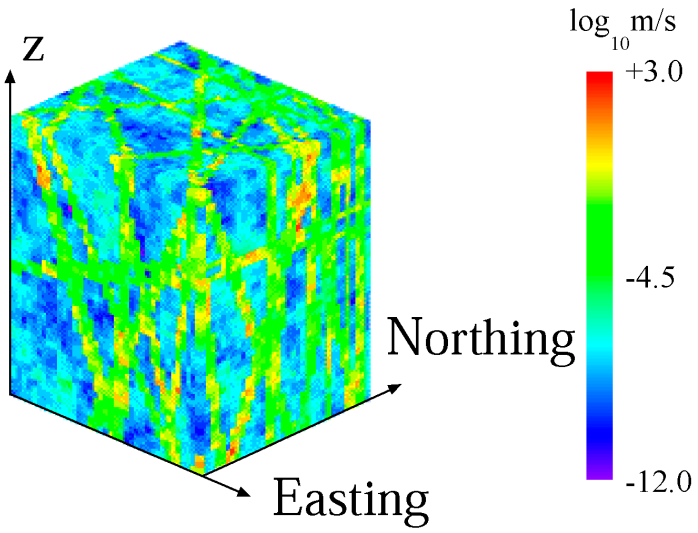

Figure 2-4. *Three-dimensional isometric view of the seed log hydraulic conductivity realisation. Scale is in log_{10}m/s.*

The so-called undisturbed piezometric heads measured at a number of borehole sections are considered as measured under a steady-state situation and are then used to condition the seed field in Figure 2-4. The values used and their co-ordinates are given in Table 2-1 with the co-ordinates referred to the origin of the model block. The application of the self-calibrated algorithm to the seed field in Figure 2-4 results in a new field in which the solution of the flow equation yields the set of conditioned heads provided in the last column of Table 2-1. As it can be seen in Figure 2-5 the conditioned field reproduces almost exactly the observed undisturbed values.

Figure 2-6 shows the field of perturbations that have to be applied to the block in Figure 2-4 to achieve conditioning to the steady-state head values. In this figure one can appreciate how the hydraulic conductivities in some structures are increased whereas in some others they are decreased. These perturbations do not necessarily have to be uniform throughout the entire structure plane, although in this particular case the shift of hydraulic conductivities is quite homogeneous in each fracture.

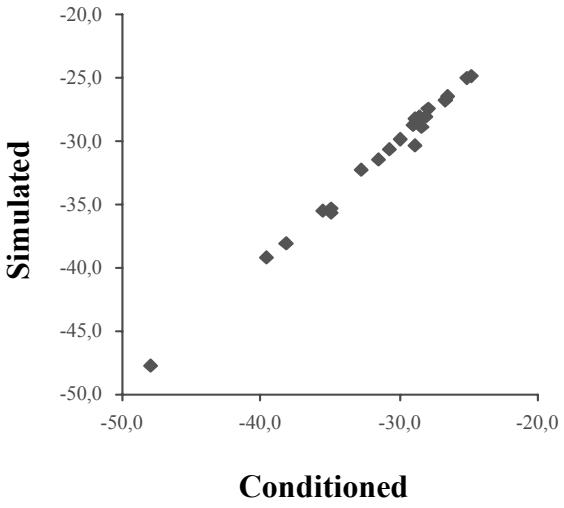

Figure 2-5. *Degree of conditioning to the steady-state heads achieved by the self-calibrated approach after perturbing the seed field in Figure 2-4 .*

Table 2-1 . Undisturbed piezometric head values used as conditioning data. Co-ordinates are in Äspö local system. Last column shows the piezometric head resulting from the solution of the flow equation in the conditioned conductivity field

x (m)	y (m)	z (m)	Measured head (m)	Conditioned head (m)
1869.9	7109.1	-455.3	-27.4	-27.9
1915.2	7140.1	-419.1	-30.7	-30.7
1958.1	7170.3	-383.1	-31.5	-31.5
1990.7	7192.7	-358.3	-35.4	-35.5
1940.3	7074.5	-499.1	-24.8	-24.8
1942.1	7088.7	-494.5	-25.1	-25.1
1946.7	7126.5	-482.5	-26.7	-26.7
1951.3	7163.3	-470.5	-28.1	-28.2
1954.1	7185.9	-462.7	-35.4	-34.9
1958.9	7224.7	-449.1	-38.1	-38.2
1830.7	7157.7	-539.5	-26.5	-26.6
1901.9	7198.3	-469.3	-28.9	-28.5
1912.7	7204.7	-459.9	-28.0	-28.6
1927.3	7213.1	-445.3	-32.2	-32.7
1963.1	7234.7	-408.3	-39.2	-39.6
1913.7	7181.7	-471.5	-30.3	-28.9
1917.7	7187.1	-469.1	-28.3	-28.9
1921.1	7192.7	-466.5	-28.7	-29.0
1928.7	7204.1	-461.3	-29.9	-29.9
1936.5	7215.5	-455.5	-35.7	-34.9
1946.7	7230.7	-448.9	-47.7	-47.9

Figure 2-7 shows a number of horizontal cross-sections of the simulated steady-state heads solution of the groundwater flow equation in the model block. Remember that the heads on all four sides of all sections were prescribed as given in Figure 2-3.

2.5 Conditioning to transient head data

The next step is to test the ability of the self-calibrated algorithm to condition the hydraulic conductivity realisation to transient piezometric head data in a three-dimensional fractured block. The only transient information available at this stage was from the compilation of activities during the drilling of some boreholes. More precisely, we used the pressure drawdown responses to the simultaneous drilling of boreholes KA2563A and KA3510A. Only qualitative information is available. More precisely, noticeable responses are observed in the four monitoring sections at KA3511A when borehole KA3510A hits fracture 5 at a depth of 47 m and when borehole KA2563A hits structures #4 (at 94 m depth), #5 (at 103 m depth) and either/both #6/#7 (at 153 m depth). No other significant response was observed when either borehole crossed any other interpreted structure.

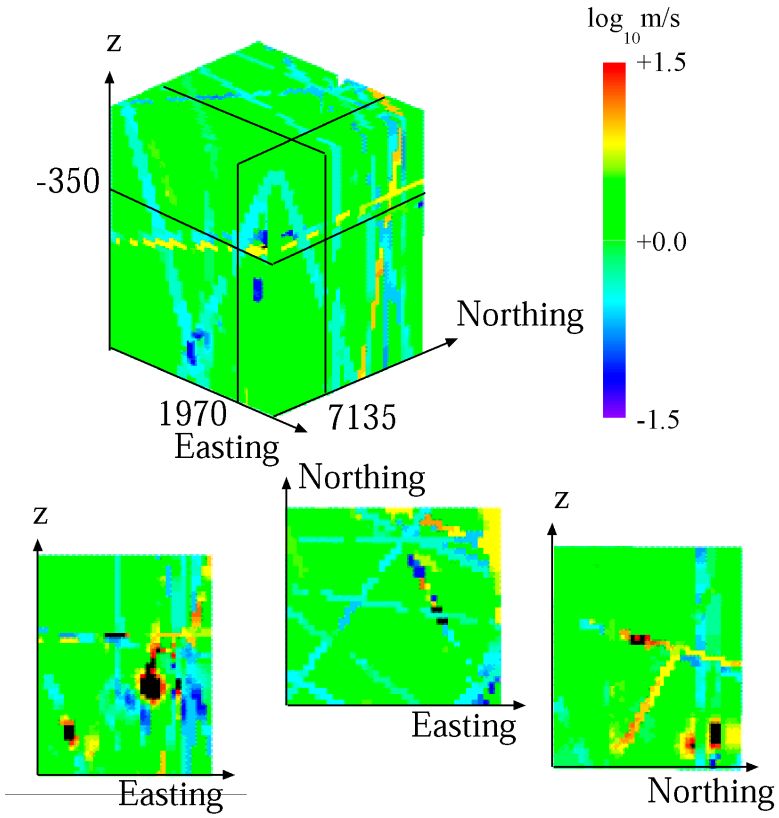

Figure 2-6. *Perturbation applied to the log hydraulic conductivity realisation in Figure 2-4 in order to achieve conditioning to the steady-state head conditioning data in Table 2-1*

The above behaviour was translated into transient conditioning information as follows: when an atmospheric pressure pulse travels through the block along the traces of the wells being drilled KA3510A and KA2563A at a speed of 6 m/d (roughly one discretization cell per day) pressure responses should be observed in the simulated borehole KA2511A with the same pattern as observed during the drilling. It is noted that the actual boundary conditions that would correspond to drilling a borehole are more complex than simply lowering the pressure at which the drilling bit is located down to atmospheric pressure.

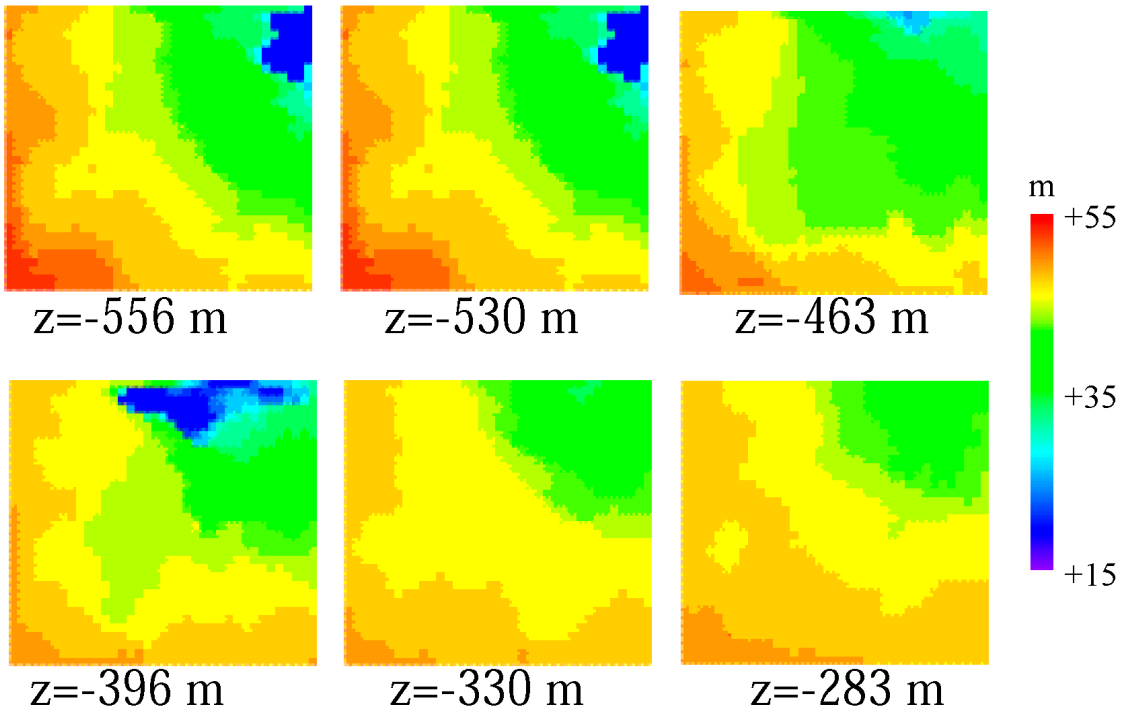

Figure 2-7. *Horizontal slices of the steady-state head solution on the conditional log hydraulic conductivity field obtained after perturbing the one of Figure 2-4*

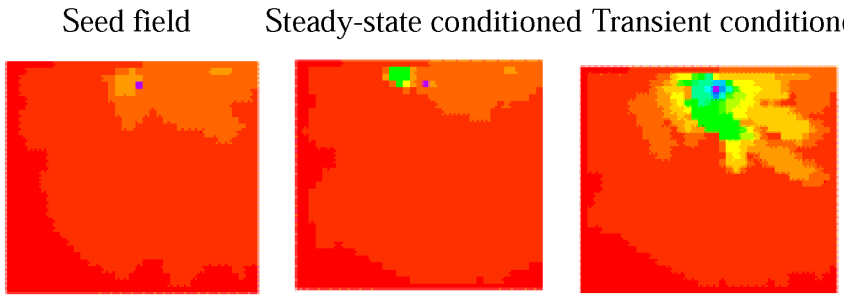

Figure 2-8. *Horizontal slices of the drawdowns simulated in the seed field of Figure 2-4, in the conductivity field conditional to steady-state heads and in the conductivity field conditioned to the transient information. The slice is taken at z=-472 m which correspond to the intersection between borehole KA3510A and fracture number 5 and at the time that the pressure pulse that is travelling down-the-hole has reached this plane.*

Figure 2-8 shows a horizontal slice at z = –472 (corresponding to the intersection of borehole KA3510A, at 47 m depth with structure #5) of the simulated drawdowns at the moment that the pressure pulse has been at that location for 8 hours. Three displays are shown, the first one corresponds to the simulation in the seed log hydraulic conductivity field of Figure 2-4, the second one in the log hydraulic conductivity field conditioned to steady-state head, and the last one in the log hydraulic conductivity field conditioned to both steady-state head and the transient head information. It is clear how, only after conditioning to the transient information, the propagation of the pulse along structure #5 is achieved.

Figures 2-9 to 2-11 show similar results to Figure 2-8 but corresponding to the instants at which the pressure pulse along borehole KA2563A intersects structure #4 (at 94 m depth), then structure #5 (at 103 m depth) and then structure #6 and #7 (at 153 m depth).

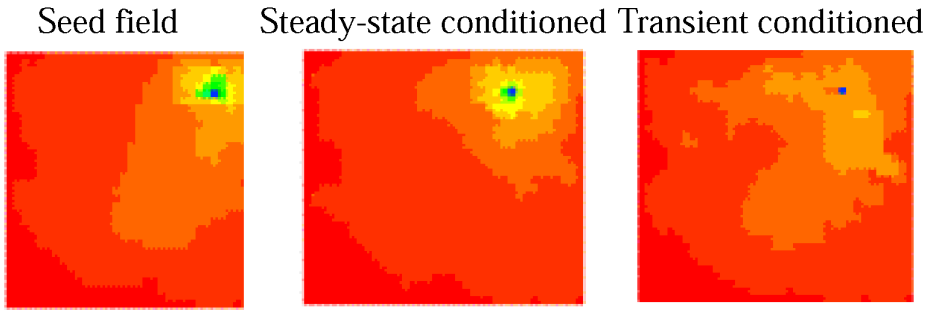

***Figure 2-9**. As in Figure 2-8. The slice is taken at z=–404 m which correspond to the intersection between borehole KA2563A and structure #4 and at the time that the pressure pulse that is travelling down the hole has reached this plane.*

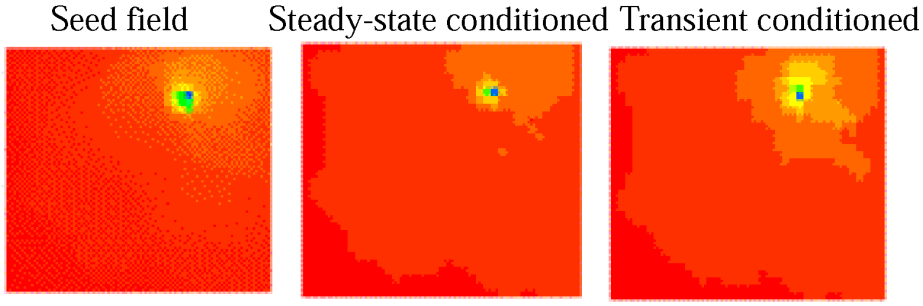

***Figure 2-10.** As in Figure 2-8. The slice is taken at z=–410 m which correspond to the intersection between borehole KA2563A and structure #5 and at the time that the pressure pulse that is travelling down the hole has reached this plane.*

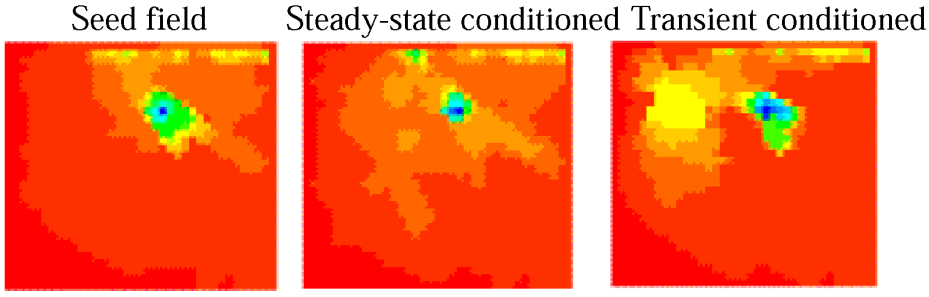

***Figure 2-11.** As in Figure 2-8. The slice is taken at z=–443 m which correspond to the intersection between borehole KA2563A and structure #5 and at the time that the pressure pulse that is travelling down the hole has reached this plane.*

The final conditioned log hydraulic conductivity field matches the hydraulic conductivity data at the measurement locations, reproduces the undisturbed heads where they had been reported and shows transient responses coherent with the log of events reported during the simultaneous drilling of boreholes KA3510A and KA2563A.

The conclusion from this assessment phase is that it seems possible to build a hydraulic model of the site at the 250 m scale using the stochastic continuum concept. However, it seems difficult to construct an ensemble of realisations that could be used for the analysis of uncertainty in flow (and transport) predictions. This is due to the large amount of computer power needed to generate each of the conditional realisations. The work described up to here presents the generation of a single conditional realisation. Multiple realisations should be generated conditional to the same information to reinforce the conclusions that are drawn on the basis of this individual realisation.

3 Conditional model of groundwater flow

After the data from the cross-hole tests performed during the spring of 1998 (Andersson et al., 2001) was available, the next objective is to build a log hydraulic conductivity model of the block of interest conditioned to this transient information which is more of a quantitative nature than the one used during the model assessment phase.

The aims of this phase are:

- to produce realisations of log hydraulic conductivity conditional to the available log hydraulic conductivity and interference test data
- to analyse, during the conditioning process, how the log hydraulic conductivity realisation evolves
- to draw some conclusions about the importance of some fractures in the hydraulic behaviour of the block

3.1 Model geometry

The model geometry is virtually the same as the one used during the model assessment phase described in chapter 2. The only (and important) difference regards the fractures included since a new structural model was available. The September'98 model (Hermanson, 2001b) benefits, respect to the October'97 model, of the information gathered after the drilling of borehole KI0023B, of additional hydraulic test information and of results of important interaction between structural geologists and hydrogeologists. Besides small changes in the geometry of the interpreted structures, the main difference between the two structural models is the inclusion of structure #13 which runs more or less parallel between structures #19 and #20 and which could play an important role in the envisaged future tracer experiments. Figure 3-1 displays the new three-dimensional block mask showing the intersection of all structures with the boundaries of the model block. A comparison with Figure 2-1 shows the differences between the two structural models.

The material properties are the same as in the model assessment phase, that is, the same log hydraulic conductivity conditioning data listed in Appendix 1 and the same statistics are used for the generation of the conditional realisations of each individual structure, once each structure has been generated, they are all merged together in a three-dimensional realisation together with the cells not including any structure.

3.2 Flow simulations

The flow simulations are carried out using the same numerical scheme as in the model assessment phase. The same set of prescribed heads described in 2-3, taken from Svensson (1997) model, are used for the simulation of steady-state conditions.

For the simulations of the interference tests (Andersson et al., 2001), the hydraulic heads on the six faces of the model block were set to zero and only drawdowns are simulated.

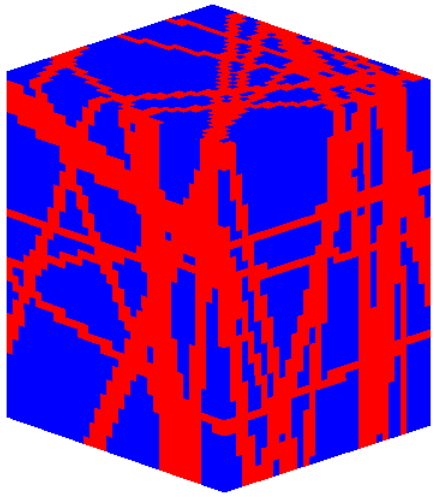

Figure 3-1. *Three-dimensional block mask showing the cells that are modelled as fractured blocks. Based on the September'98 structural model (Hermanson, 2001b)*

3.3 Conditioning to interference test data

The objective of this part of the analysis is to build a log hydraulic conductivity model based on a seed field generated according to the material properties listed above and with the distribution of fractures depicted in Figure 3-1. The initial intention was to build directly a realisation conditional to all nineteen cross-hole interference tests (Andersson et al., 2001); however, after the first tests, the task was beyond our computer capabilities. A decision was taken to select a subset of the interference tests and condition, initially, only to these tests. The attempt to condition to a subset of 7 tests, six short-term and a long-term one, in a single step was not viable: the conditioning step, which involves a heavy optimisation, did not converge. The solution was to include the tests sequentially, so that a log hydraulic conductivity field is made conditional to the cross-hole tests in increasing succession: a seed field is used to obtain a log hydraulic conductivity field conditional to one short-term test, the resulting field is used as a seed field to generate a new field conditioned to the previous short-term test plus an additional test, and so on. Following this procedure it was possible to generate the log hydraulic conductivity field shown in Figure 3-2, conditional to the tests listed in Table 3-1. Table 3-2 gives the monitoring locations used in the conditioning process using hydraulic heads. The selection of the tests was done with the following criteria. Tests #7 and #8 were chosen because they seemed to be easy to reproduce, matching

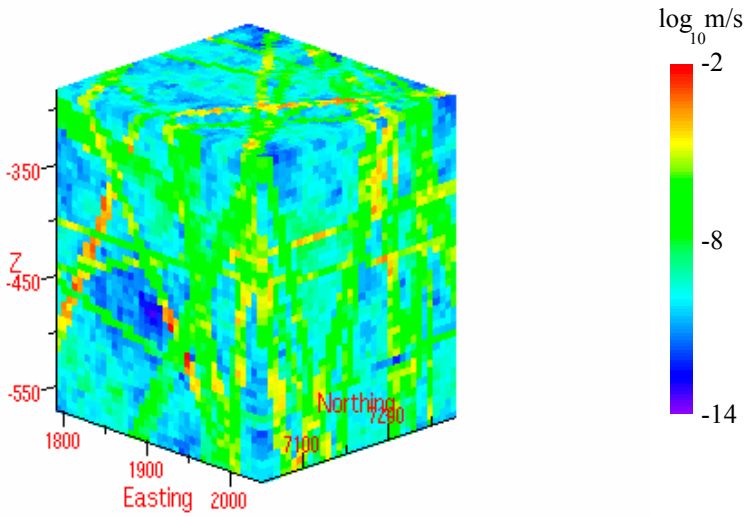

Figure 3-2. *Log hydraulic conductivity field conditioned to the interference tests in Table 3-1. Scale in log_{10} m/s*

them involves mostly making less permeable some of the fractures that were originally too connected in space. (Test #7 also affects structure #7 that could be a downstream boundary for the tracer test modelling.) Tests #9 and #12 focused on structure #19 one of the possible bounding features of the tracer tests domain. Test #13 produced significant responses at several locations, and test ESV-1c had been used for tracer testing and we wanted to make some contaminant transport simulations using the data from this tracer test on a conductivity field already conditioned to the hydraulic responses.

The process of conditioning to piezometric head is carried out using a non-linear optimisation algorithm. As opposed to the standard geostatistical conditioning, conditioning through optimisation does not ensure exact reproduction of the conditioning (measured) data. Figure 3-3 shows the degree of reproduction of the measured piezometric heads for each one of the six interference tests included. As it can be appreciated, the reproduction of the measured heads is not as good as desired, especially for test ESV-1c. The use of Tests #7, #8 and #12 in which the measured responses are either null or negligible helped in reducing some of the existing connectivity in the seed log hydraulic conductivity field. In these three tests, the seed conductivity field had several monitoring sections with simulated responses that after conditioning show no response. The most significant mismatches occur for Test ESV-1c, particularly with regard to structure #20: two of the sections that show good response in the field intercepted by structure #20 are not being matched in the simulation. Increasing the conductivity of this structure does not improve the match while it introduces too large discrepancies in the reproduction of Test #8. There is a need to connect the source section to structure #20. On the other hand the response at the source location and in sections P4 and P5 of KI0023B are very well reproduced.

Table 3-3 shows the evolution with conditioning of some statistics computed for each fracture. Notice that all structures start with mean values of log hydraulic conductivity around –6.5 $\log_{10}$m/s and some of them undergo important changes during the process of conditioning to piezometric head. Most noticeably, structure #5 increases its conductivity almost two orders of magnitude, and structure #7 decreases its conductivity one and a half order of magnitude. With regard to the structures close to the envisaged area for the tracer test, the most important change occurs in structure #19 that increases its average conductivity almost by an order of magnitude. The histograms of log hydraulic conductivity in the fractures evolve from close to Gaussian to negatively skewed with the net effect of an increase of in-plane structure heterogeneity. The structures in which this effect is most noticeable are #7, #8, #9 and #20. This negative skewness, which is due to the appearance of cells including structures with conductivities in the order of magnitude of the cells not including structures, can be understood as a correction to the enhanced connectivity introduced in the seed log hydraulic conductivity field, in which all structures are incorporated as planes extending to the boundaries of the model block.

Table 3-1. Interference tests to which the log hydraulic conductivity field of Figure 3-2 is conditioned

Test # [1]	Type	Source	Flow period (h)	Model cell for source	Fracture being tested
7	CH[2]	KI0025F:R3	0.5	(24, 11, 13)	?
8	CH	KI0025F:R5	0.5	(25, 20, 16)	#6, #7
9	CH	KI0025F:R2	0.5	(23, 6, 11)	#19
12	CH	KI0023B:P2	0.5	(17, 17, 13)	#19
13	CH	KA3573A:P1	0.5	(16, 33, 20)	#15
ESV-1c	CQ[3]	KI0023B:P6	384.0	(20, 21, 15)	#9

[1]Andersson et al. (2001) [2]Constant head test, [3]Constant flow test

Table 3-2. List of locations used to monitor piezometric heads during the interference tests listed in Table 3-1 and employed for the conditioning to the log hydraulic conductivity field of Figure 3-2

Monitoring location	Cell in model	Information provided
KI0025F:R1	(23, 4, 11)	Response observed during test #9
KI0025F:R2	(23, 6, 11)	Imposed head drawdown during test #9
KI0025F:R3	(24, 11, 13)	Imposed head drawdown during test #7, response observed during tests #9 and ESV-1c
KI0025F:R4	(24, 17 ,15)	Response observed during tests #7 and ESV-1c
KI0025F:R5	(25, 20, 16)	Imposed head drawdown during test #8, response observed during test #13
KI0025F:R6	(25, 26, 18)	Response observed during test #13
KA2511A:S2	(12, 9, 17)	No response observed in any test
KA2511A:S3	(19, 14, 23)	No response observed in any test
KA2511A:S4	(25, 18, 28)	No response observed in any test
KA2511A:S5	(30, 21, 32)	No response observed in any test
KA2563A:R1	(6, 16, 5)	Response observed during test ESV-1c
KA2563A:R4	(17, 22, 15)	Response observed during test ESV-1c
KA2563A:R5	(18, 23, 16)	Response observed during test ESV-1c
KA2563A:R6	(21, 25, 19)	Response observed during test ESV-1c
KA2563A:R7	(26, 28, 24)	No response observed in any test
KI0023B:P4	(19, 20, 15)	Response observed during test ESV-1c
KI0023B:P5	(19, 21, 15)	Response observed during test ESV-1c
KI0023B:P6	(20, 21, 15)	Source location for test ESV-1c
KI0023B:P7	(21, 23, 16)	Response observed during test ESV-1c
KI0023B:P8	(22, 25, 17)	Response observed during test #13
KI0023B:P9	(23, 27, 18)	Response observed during test #13
KA3510A:P1	(16, 30, 14)	No response observed during any test
KA3573A:P1	(16, 33, 20)	Imposed head drawdown test #12
KA3573A:P2	(16, 30, 19)	Response observed during test #12
KA3600F:P1	(11, 34, 20)	No response observed during any test
KA3600F:P2	(7, 33, 20)	Response observed during test #12

Figures 3-4 and 3-5 show horizontal cross-sections through the final conditioned log hydraulic conductivity field and through the perturbations applied to the seed field in order to arrive at the conditional field. These figures indicate that the perturbations are quite significant especially at the levels around –450 m. The contrast between cells including structures and cells not including structures, and some of the structures become very conductive, such as are structures #8 and #19. Figures 3-6, 3-7 and 3-8 show the final log hydraulic conductivity distributions in structures #8, #19 and #20 along with the associated perturbations applied to the seed log hydraulic conductivity field in order to arrive at the conditional realisation.

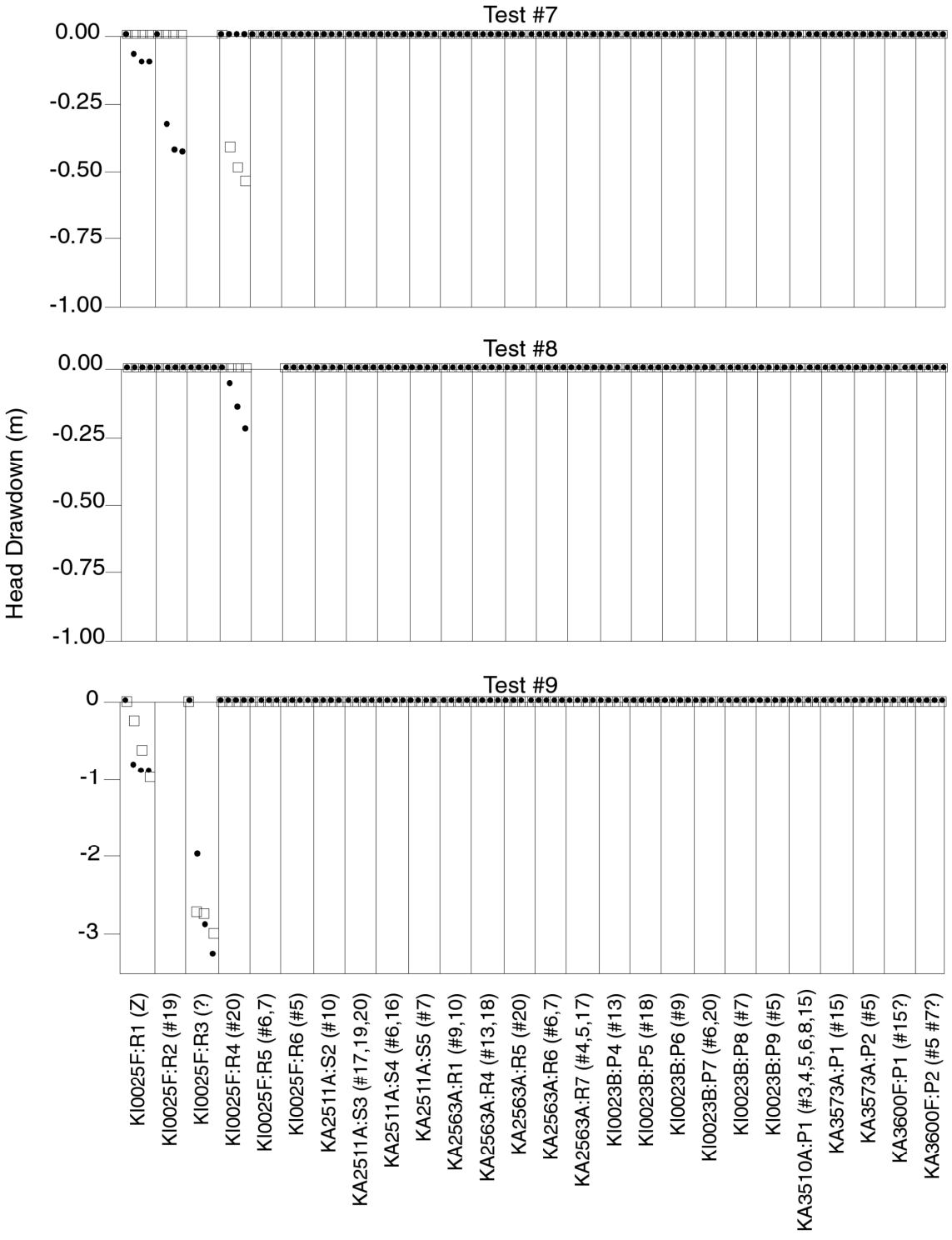

Figure 3-3a. *Reproduction of the observed heads in the log hydraulic conductivity realisation after conditioning. The squares represent the measurements, the dots, the simulated values. If the dots are inside the square the conditioning process was satisfactory. All 26 observation locations are displayed for each test. Each vertical bar represents the drawdown at the observation location for a period of 0.5 hours except for test ESV-1c in which the observations last 384 hours. Notice the variation of the scale of the head drawdown axis.*

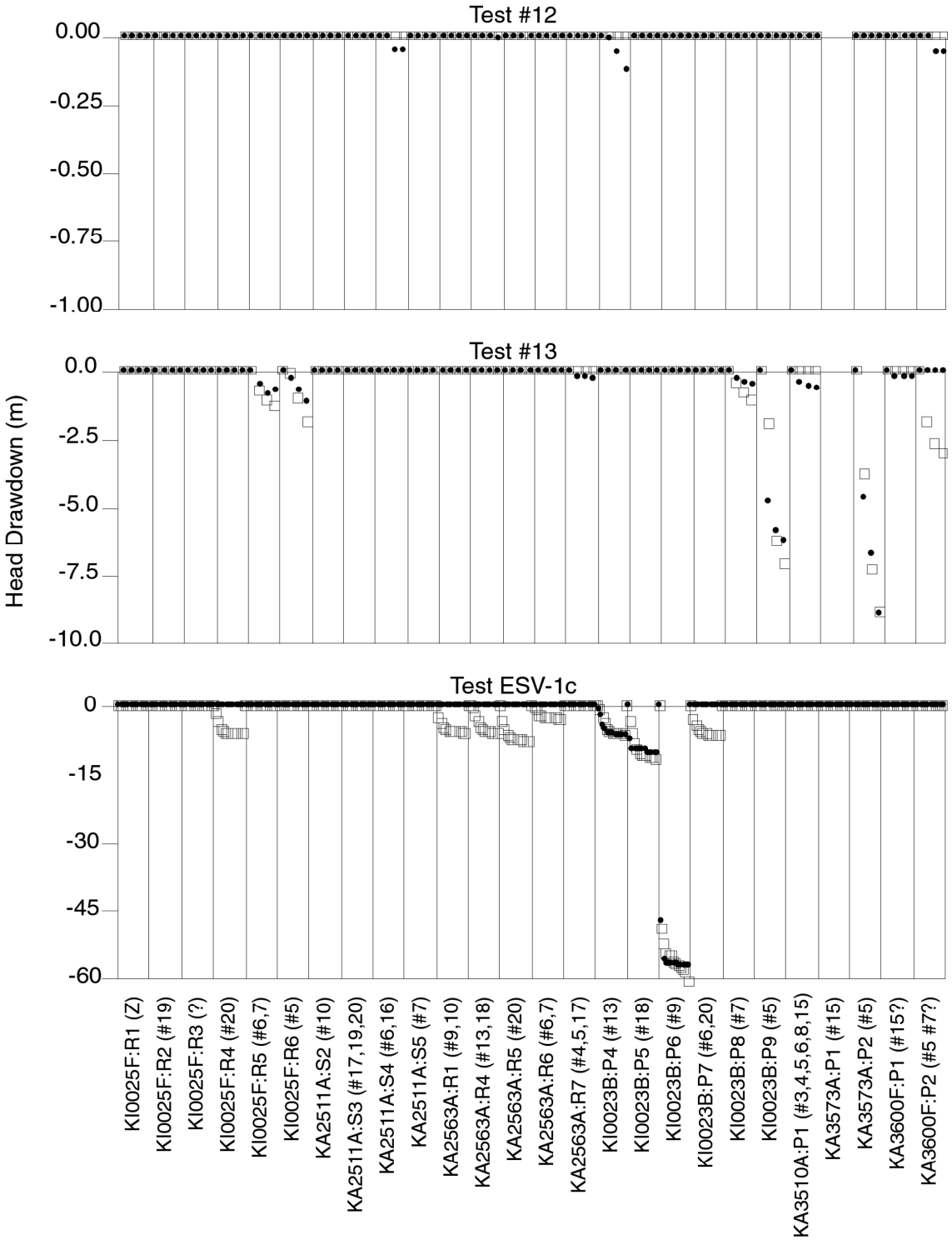

Figure 3-3b. *Continuation of Figure 3-3a (same caption).*

Figures 3-6 to 3-8 permit to appreciate the need for local heterogeneity within the structure planes in order to match the measured piezometric head. Locally the structure planes must contain areas of high and low hydraulic conductivities. This heterogeneity could be interpreted as heterogeneity in fracture aperture. It is also interesting to note how some structure intersections are clearly distinguishable within the structure planes due to their conductivity contrast with the rest of the structure planes, whereas some others remain camouflaged on the structure plane. During the conditioning phase, the cells at structure intersections were considered as part of the intersecting structures and the value assigned was the geometric mean of the value that the cell would have if it belonged to each structure independently.

Table 3-3. Evolution of fracture average hydraulic conductivities as piezometric head information is used in the conditioning process

Structure	Average hydraulic conductivity values on seed realisation	Average hydraulic conductivity values in realisation conditioned to steady-state head	Average hydraulic conductivity values in realisation conditioned to transient piezometric head	Change in average hydraulic conductivity between the seed realisation and the one conditioned to transient head
Background	-10.12	-9.83	-10.19	-0.07
#1	-6.47	-6.54	-6.54	-0.07
#2	-6.32	-6.22	-6.34	-0.02
#3	-6.47	-6.40	-6.46	+0.01
#4	-6.44	-7.30	-7.32	-0.88
#5	-6.55	-4.98	-4.62	+1.93
#6	-6.75	-8.18	-8.29	-1.54
#7	-6.39	-7.27	-7.37	-0.98
#8	-6.41	-4.78	-5.38	+1.03
#9	-6.56	-8.05	-8.02	-1.46
#10	-6.29	-7.57	-7.41	-1.12
#11	-6.55	-7.93	-7.77	-1.22
#13	-6.48	-6.55	-6.59	-0.11
#15	-6.51	-7.75	-7.59	-1.28
#16	-6.27	-5.42	-5.32	+0.95
#17	-6.28	-6.19	-5.90	+0.38
#18	-6.22	-6.77	-7.04	-0.82
#19	-6.40	-5.98	-5.52	+0.88
#20	-6.44	-6.35	-6.58	-0.14
#Z	-6.30	-7.20	-7.13	-0.83
EW-1	-6.30	-6.33	-6.32	-0.02

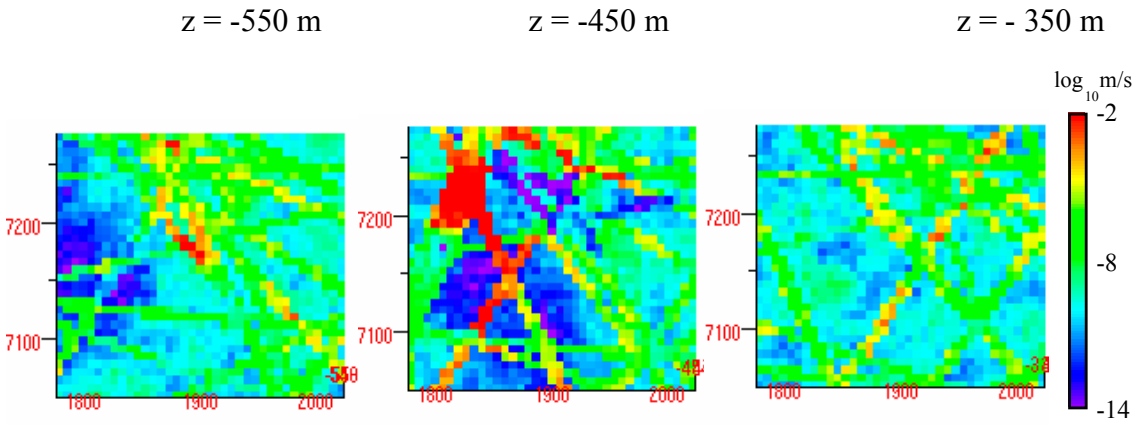

Figure 3-4. *Three horizontal cross-sections through the final conditional log hydraulic conductivity block in Figure 3-2*

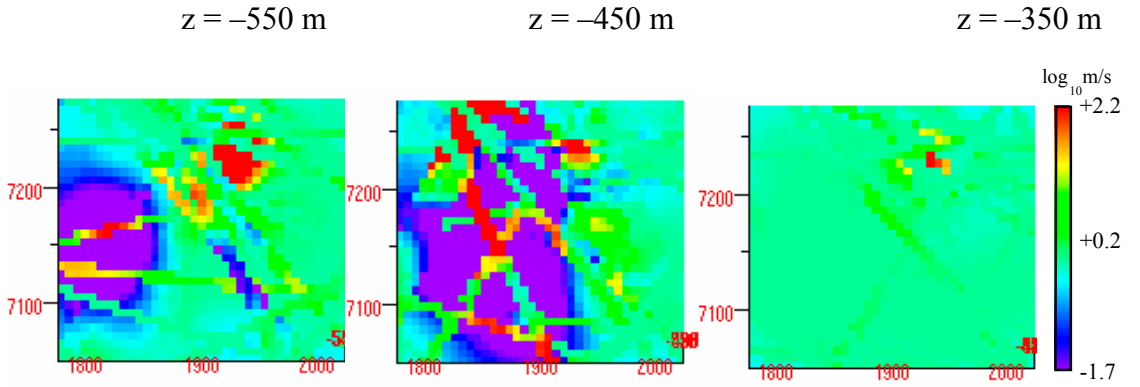

Figure 3-5. *Three horizontal cross-sections through the perturbations applied to the seed log hydraulic conductivity field in order to arrive at the final conditional log hydraulic conductivity block shown in Figure 3-2*

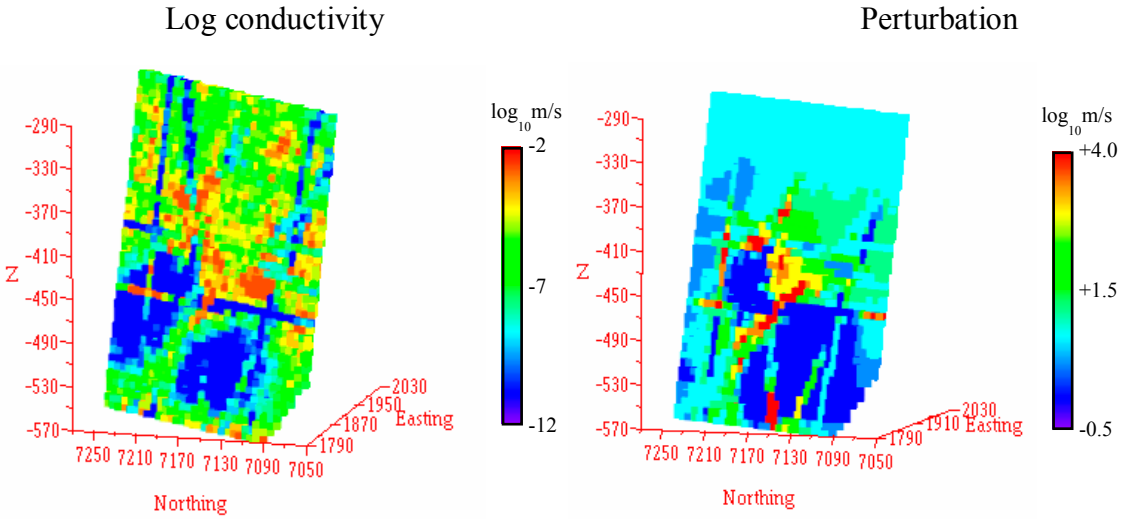

Figure 3-6. *Final log hydraulic conductivity distribution in structure #8 and perturbation applied to the log hydraulic conductivity of the seed field to arrive at the conditional realisation.*

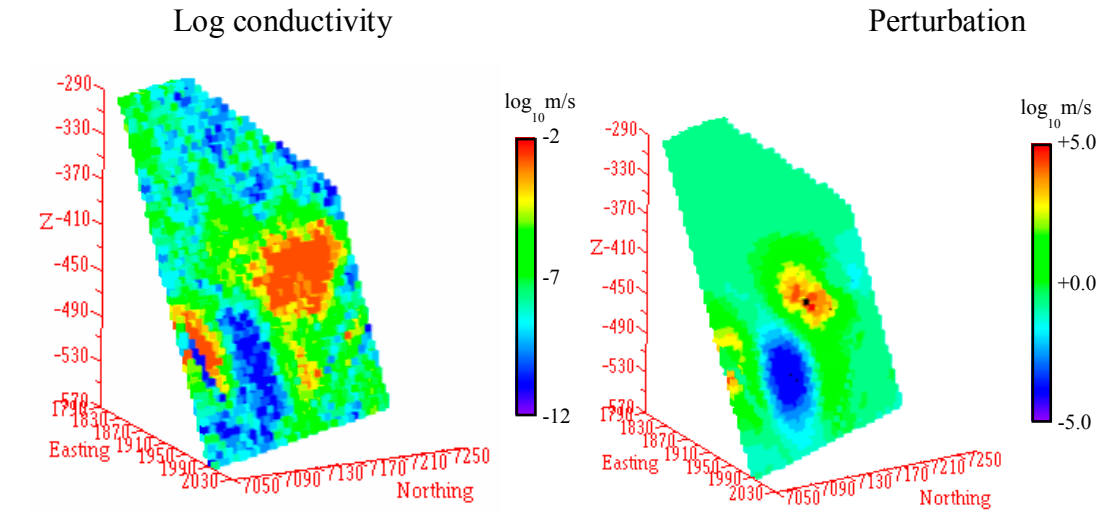

Figure 3-7. *Final log hydraulic conductivity distribution in structure #19 and perturbation applied to the log hydraulic conductivity in the seed field to arrive at the conditional realisation.*

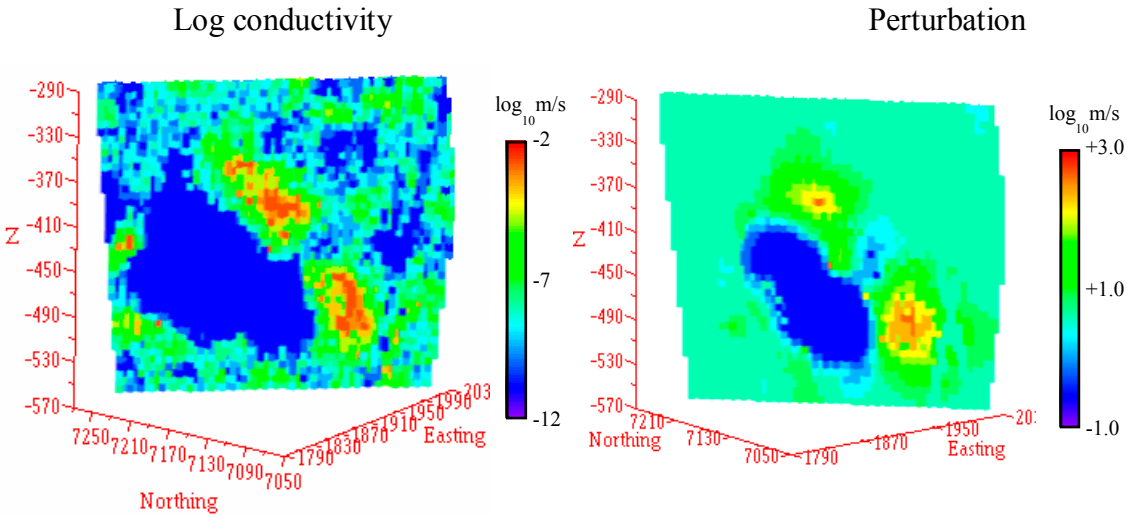

Figure 3-8. *Final log hydraulic conductivity distribution in structure #20 and perturbation applied to the log hydraulic conductivity in the seed field to arrive at the conditional realisation.*

3.4 Further flow modelling and interfacing with the transport model

The flow model continued being updated as more information was available and the hydrostructural model was updated. More precisely, after verifying the plausibility of our approach with the September'98 hydrostructural model, two additional flow models were built, based on the March'99 and March'00 hydrostructural models (Doe, 2001).

The most important modifications to the September'98-based flow model are discussed next. The flow model based on the March'99 hydrostructural model, includes two new deterministic structures, #21 and #22, and considers the re-description of all structures performed by Doe (2001), including some changes in the position and orientation of the

structures, and, more importantly, it limits the extent of the structures, some of which now terminate before the boundaries of the model. Five of the interference tests carried out in the phase A tests were used to condition the flow model. The flow model based on the March'00 hydrostructural model has virtually no change in the representation of the deterministic structures, since the only new structure considered cannot be resolved given the discretisation used in the finite difference model, the most important change in this model is the use of the detailed log hydraulic conductivity information provided by the POSIVA flow logging tool in all boreholes, including the newly drilled KI0025F03.

In the last two rounds of flow model building, it was possible to generate up to ten conditional realizations.

The conditioned hydraulic conductivity realisations can be considered as the best representation of the heterogeneity within the modelling area at the discretisation scale. These realisations are then passed on to the transport model. They require a transformation to map the finite difference values onto the finite element discretisation. This mapping which is explained in the following chapters, requires of an interface to perform the transformation. Once the hydraulic conductivities have been mapped onto the finite element model, the solute transport model is informed with values for the transport parameters, and predictions and calibrations are performed.

A flow-chart of the modelling process is displayed in Figure 3-9.

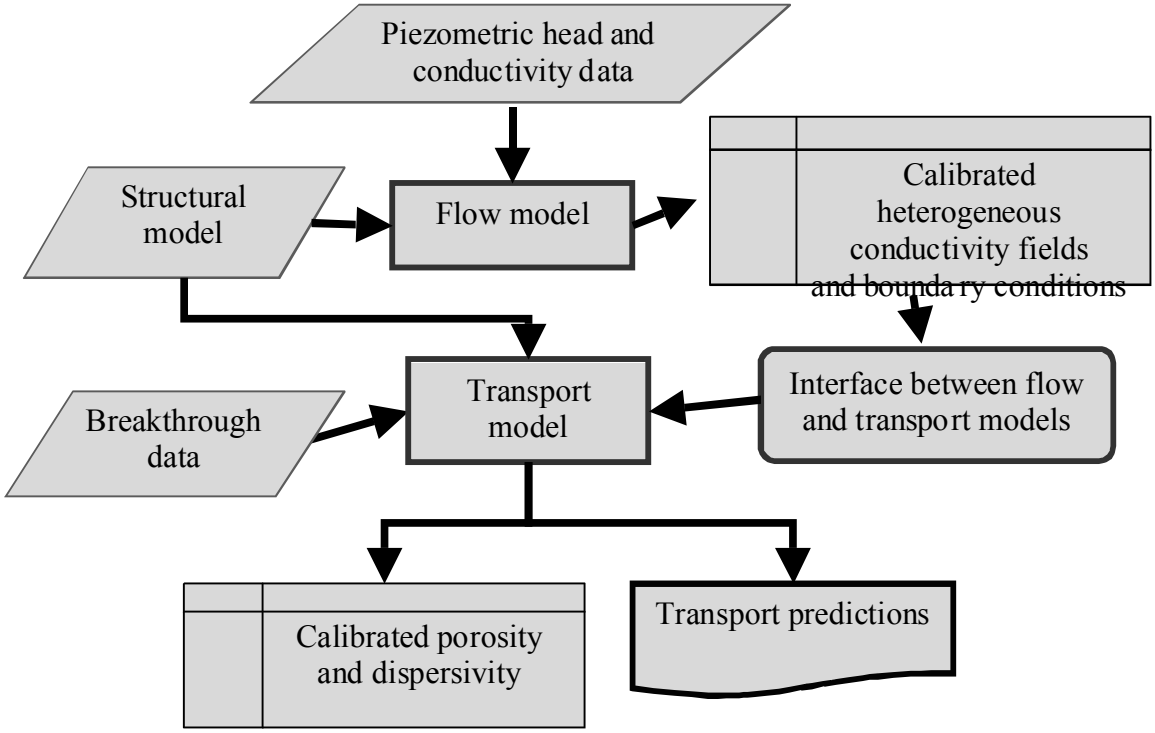

Figure 3.9. *Input data, process models, interface models and model results considered in the SC approach*

4 Flow model conclusions

It is possible to use stochastic continuum models for the characterisation and modelling of three-dimensional fractured media. Geostatistical and inverse modelling techniques can be used to generate heterogeneous realisations of log hydraulic conductivity capturing the spatial heterogeneity of hydraulic conductivity and conditional to structural geology, hydraulic conductivity measurements and piezometric head measurements. Theoretically, the stochastic nature of the approach allows uncertainty characterisation through the generation and posterior analysis of multiple realisations. Unfortunately, at the moment, uncertainty characterisation is impossible due to computer limitations. The generation of a single realisation conditioned to all information available is very costly.

The process of conditioning to the steady-state and transient piezometric head information is sequential and the evolution of the hydraulic conductivity field as more data are incorporated can be used to evaluate the relevance of some structures or the need to consider additional unexplored structures. The fact that the conditioning process to transient piezometric head is not capable to match some of the experimental measurements needs to be further explored. It may be due to a weakness of the conditioning algorithm or to some inconsistency between the model and the observed conditioning measurements. An analysis in more detail of why the model cannot be made to reproduce some of the experimental drawdowns must be carried out.

Although in the beginning all structures in the seed conductivity field are assigned hydraulic conductivity values with the same mean and standard deviation, the conditioning process alters both means and standard deviations and stands out some structures among the others. Most noticeable structure #5 increases its average log hydraulic conductivity from –6.5 to –4.6 $\log_{10}$m/s. The analysis of the evolution of the structure mean and standard deviation as the conditioning progresses can also be studied and be helpful in the better understanding of the joint behaviour of the block.

5 Transport model

In TRUE Block Scale Project, five sets of tracer tests have been made, starting with A-4 and A5 tests, followed by B1 and B2 phases, and finally phase C tests, where sorbing tracers were used. This report is focused on the work made using the Stochastic Continuum approach applied to Phase C tracer tests. The modeling work in phase C tests consisted of two steps: first, a blind prediction of the tracer tests using the models already developed with the information of previous phases was made, and second, using the breakthrough data check why the models did not perform well and improve model's performance. In this chapter we present a concise description of the modeling efforts made to represent the medium using the Stochastic Continuum approach, viewing its capabilities to predict and model the different tracer tests and its limitations and drawbacks. The blind prediction has been also made using a semianalytical approach by interpreting each tracer test separately, because this method cannot account for all tracer tests together. In the Stochastic Continuum approach (numerical approach), all tracer tests have been taken into account simultaneously.

5.1 Description of transport three-dimensional model

In this section, the conceptual model, the numerical model and some relevant information in the analysis of the tracer tests is presented.

5.1.1 Transport conceptual model

Solute transport is assumed to take place in both, deterministic structure planes (defined by the hydrostructural model) and background fracturing (structures not included in that model). This view can be justified by considering that background fractures may form connected pathways.

In addition, due to the characteristics of the site, it is also assumed that the heterogeneity plays an important role at the site, in that the hydraulic conductivity of the matrix and the transmissivity of the structure planes displays a large variation in space. Heterogeneity comes from many sources: different infilling in the structures, background fracturing (not defined in the structural model), variations in lithology, etc. For this reason, we consider that the conductivity (transmissivity in the structures) is a heterogeneous random field. This means that we will work with several equally likely representations of the actual field.

The transport processes considered are dispersion, diffusion, retardation (due to sorption, e.g.), first order decay (radioactive decay) and sinks and sources, and in the final steps matrix diffusion. Comparing with flow equation, additional parameters in the transport equation are dispersivities, molecular diffusion, retardation coefficient, porosity, thickness, input concentration function and first order decay coefficient (radioactive decay).

5.1.2 Transport numerical model

– Domain

The transport area model extends from 1860 m to 1960 m Easting, from 7140 m to 7240m Northing and from –500 m to –450 masl. This extension has been chosen as an area that includes the area of interest (the injection and pumping sections), plus an additional extent to reduce boundary effects, but maintaining it small enough, to allow small size elements in the area of interest. To reduce unwanted boundary effects, boundary heads have been taken from flow simulation. The grid is finer close to the pumping/injecting sections and gets coarser as it approaches to the boundaries (Figure 5.2)

– Structures

The structural model of Doe (2001) is used to include the structure planes (with their actual size) that belong to our model domain.

Structures #23 and #24 have not been included in the transport model because neither they were in the flow model. However, flow model was conditioned to steady state heads and drawdowns coming from interference tests, so the calibrated conductivities should have been automatically modified by the effect of these structures reflected on drawdown data, so up to certain extent, the effect of these structures is included in the model.

Due to the large number of structures, some simplifications have been made to allow its inclusion in the transport model (in the first part of this report the simplifications made in flow model have been explained). The representation of the structures in both models is not exactly the same because the differences between the flow (finite differences) and transport (finite elements) codes employed, see figures 2.1 and 5.1.

The included structures are #5, #6, #7, #8, #13, #15, #18, #19, #20, #21 and #22 taken from the structural model. The structure planes are treated as 2D features embedded into a 3D medium. Structure number 18 is introduced exactly as the equation plane defined in Doe (2001). The rest of structures are approximated by at least one vertical plane (Figure 5.1).

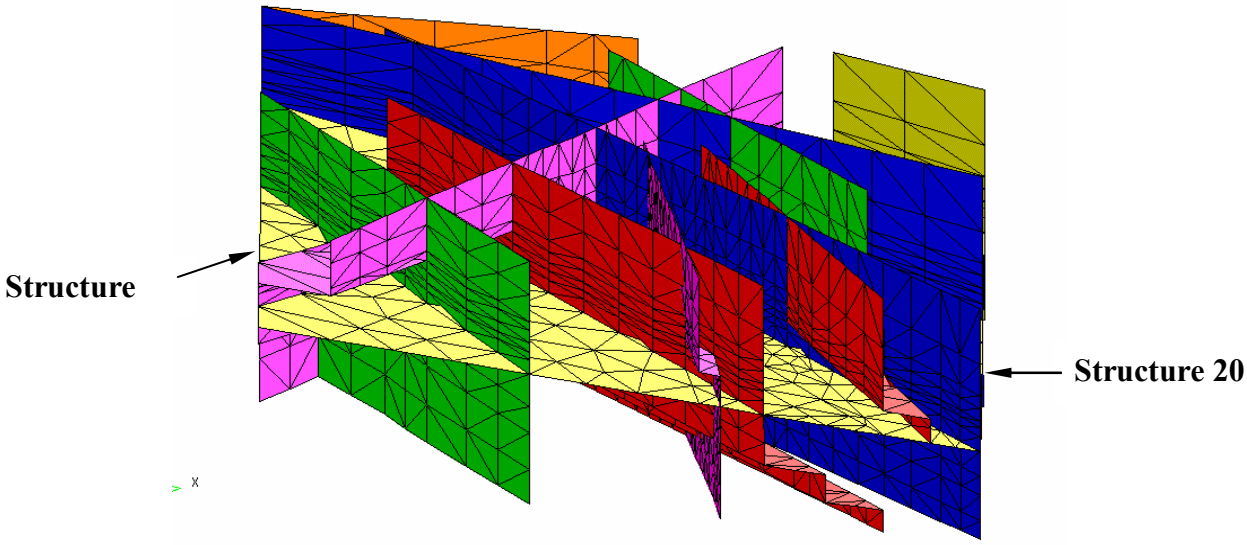

Figure 5-1. *Structure planes, treated as 2D planes.*

(depending on the inclination of the structure), as seen in Figure 5.1. The extension of the structure planes is coherent with the report of Doe (2001).

– Grid

The grid was generated in two steps. In the first step, a two-dimensional grid is generated including all the features with the code 2DUMG (Bugeda, 1990). Whit this grid, the three-dimensional grid is generated using code TRIDI (Vives, 1996). The final finite element grid consists of 4620 nodes and 11869 elements (Figure 5.2), whose size ranges approximately between 8 m^3 and 400 m^3 (finer in the interest area, coarser in the boundaries).

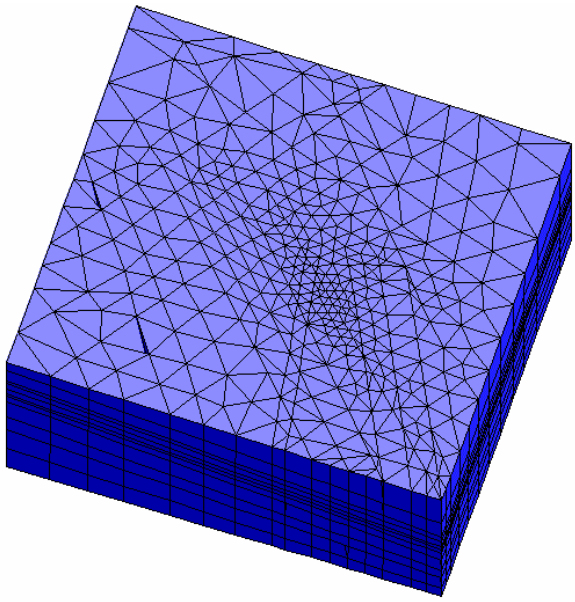

Figure 5-2. *Finite element grid*

– Hydraulic conductivity

We took the calibrated conductivities obtained with the flow model. As the grids used for solving flow and transport are not the same (finite differences/finite elements), the conductivity values from the flow model have to be transformed. The transformation is divided into two parts.

- First, the fracture values are transformed. For every 2D element of the finite element grid, we identify which cells (of the finite differences grid) are "inside" the finite element. Then, we take the geometric average of those values times the "thickness" of the finite difference cell as the transmissivity value of the 2D finite element. If the size of the finite element is smaller than the finite differences cell size, the value of the cell to which the element belongs to, is assigned to it.
- Second, once the assignment of the transmissivity of the deterministic structures has been finished, the conductivity values of the cells in the finite difference model, associated to fractures, is changed to the geometric average of the surrounding cells associated to matrix. Now, a similar procedure is applied to assign the conductivity values to the three-dimensional finite elements. The geometric mean of the hydraulic conductivities of all cells inside a finite element is assigned as the conductivity of the element. If the element is smaller than the grid cell, the hydraulic conductivity of the cell that contains it is taken as the hydraulic conductivity of the element.

Due to the different type of grids (FD vs FE), some difficulties were found at the first steps of transport modelling work. We had some problems due to the different approaches employed solving flow and transport equations (finite differences/finite elements). The main effect of these differences is the smoothing of the conductivity spatial variability and the different connectivity between structures in both grids (due to the way the two approaches manage the structures, different types of connectivity are seen, and this may have an important effect when the difference in conductivity between matrix and structures is large). Whatever approach we use, this process leads to a smoothing of the conductivity field, mainly, where the grid gets coarser. However, we expect that the smoothing is not important in the refined areas.

In the Stochastic continuum model we do not look for a unique conductivity field, but for fields that allow an accurate representation of the flow data. For this reason, it is usual to have several fields and make predictions with all of them. In our case we have obtained five conductivity fields and we have made one transport simulation with each one in phases B-2 and C. In the rest of tracer tests we worked with only one realization of the conductivity field.

- Boundary conditions
  - Flow: The flow boundary conditions are prescribed heads that are interpolated from the results of the UPV flow model, under steady state flow hypothesis and with pumping rate equal to the pumping of each tracer test. That is, a different prescribed head will be used for each one of the analysed tracer tests. This decision has been made because the transport model is smaller in size, so the pumping may have a larger effect on the transport model boundaries than in the flow model ones. At the pumping and injection points a prescribed flow rate is used.

  - Transport: At the injection point, the input is modelled as a mass flow (Q x cinj, where Q is the injection flow rate and cinj is the injected concentration function). A similar condition is set at the inflow boundaries, Q Cext, where Cext=0 (clean water comes at inflow boundaries).

- Transport parameters:

The values of dispersivities, molecular diffusion, retardation coefficient, porosity, thickness, and first order decay coefficient (radioactive decay) were initially taken from previous reports, but some of them have been calibrated using breakthrough curves during the different phases of TRUE BLOCK SCALE project (PT-4, A4, A5, B1, B2).

All the numerical tracer tests predictions/calibrations were made using TRANSIN-III code (Galarza et al., 1996).

5.1.3 Overview of in situ tracer tests

As mentioned before, this report is mainly focused of Phase C tracer tests. However, for the sake of completeness, a brief description of all the predictions/calibrations made in TRUE Block Scale Project with the Stochastic continuum approach is presented in this section. During the TRUE Block Scale Project, several sets of tracer tests were performed, involving different structures, different injection and pumping sections and tracers, as a previous work to characterize the medium, before the sorbing tracer tests of phase C were done.

Some of those tests have been predicted or have been used to calibrate flow and/or transport models.

These tests were grouped and sequentially made. The sequence was:

Phases A4, A5 First modeled tracer tests. Two steps were made in this phase. First, blind predictions were attempted. Second, used to calibrate transport parameters.

Phase B1 The breakthrough data of this phase was used to calibrate transport parameters and check transport model

Phase B2 Same as Phase B1

Phase C First, blind prediction was attempted. Second, model responses were improved using the breakthrough data.

To make the blind predictions of phases A4 and A5, we needed to assign reliable values to transport parameters, because otherwise, the model output may differ significantly from the observed data. The way of obtaining reliable parameters was to calibrate some available transport data collected in similar circumstances to tracer testa A4 and A5. We calibrated first one of the PT-4 tracer tests, to obtain these reliable transport parameters for our model, and then we started with the prediction/evaluations phases whose main characteristics are displayed in Table 5.1 (involved injection/pumping sections, pumping rate, etc.).

Table 5-1 . Characteristics of the predictions/evaluations phases.

	PHASES				
	A4	A5	B1	B2	C
INJECTION POINTS	KI0025f03P5 (R)	KI0025F02P6 (R)	KI0025f03P5 (R)	KI0025f03P5 (R)	KI0025f03P5 (R)
	KI0025f03P6 (R)	KI0025f03P6 (R)	KI0025f03P6 (R)	KI0025f03P6 (R)	KI0025f03P7 (R)
	KI0025f03P7 (R)	KI0025F02P5 (R)	KI0025F02P3 (R)	KI0025f03P7 (R)	KI0025F02P3 (D)
		KI0025F02P3 (R)		KI0025F02P3 (D)	
		KA0063AS4 (R)			
PUMPIMG POINT	KI0023BP6	KI0025f03P5	KI0023BP6	KI0023BP6	KI0023BP6
PUMPING RATE	2.4 l/m	2.6 l/m	1.2 l/m	2.06 l/m	2 l/m
PREDICTION (P)-CALIBRATION (C)	P	P	C	C	P

D: Dipole, R: radially convergent.

The Phase A tests, A-4 and A-5, were performed as radially convergent tracer tests with two different pumping points (KI0023B:P6 and KI0025F03:P5) and very similar pumping rates, about 2.5 l/min. In test A-4 the tracer was partially recovered at the pumping well in only two of the three cases. No measured breakthrough curve was obtained from the injection at section KI0025F02:P3, and also the numerical model prediction was very small. In A-5 test no concentration was measured at the pumping well in one of the five injections (injecting at section KI0025F03:P7) and the numerical prediction was below the detection limit.

In all cases, the peak times of the predictions and the actual measurements were, in general, good, but the recovery was smaller in the predictions than in the measurements, except in two of the injections where it was the opposite case. To enhance these results, we improved the translation of the conductivities values from the flow model to transport model, obtaining better results.

After Phase A, only one pumping section was selected (KI0023B:P6) to use in the next tracer tests stages (B1, B2 and C). Phase B1 tests were used to test again the transport model, improve the transport parameters and look at the discrepancies between model and data. Phases B-2 and C are explained in detail in the next sections.

5.1.4 Injection functions

As we had to make many simulations (several times the number of tracer tests times the number of generated conductivity fields), it was important to speed up the calculations. For this reason, the injection functions were slightly modified to have a good approximation with a good computational performance.

The injection functions that we received from the experimental team describe normalized concentration versus elapsed time at the injection section, as shown in Figure 5.3 (C1 Br-82 test injection).

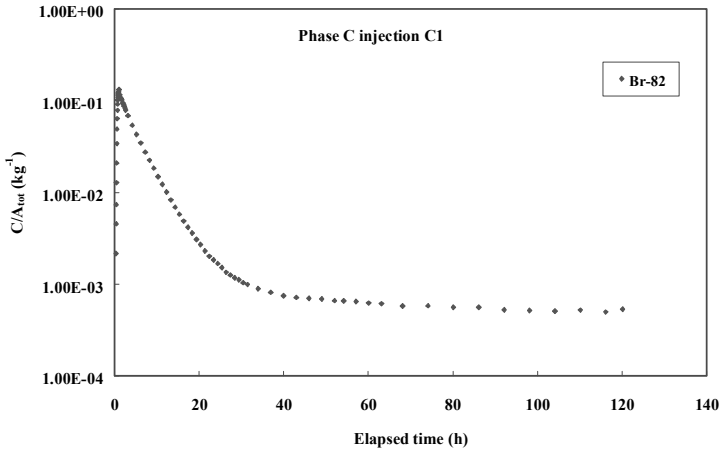

Figure 5-3. *Original injection function. C-1 test, Br-82 injection.*

As we said in section 5.1.2, the injection of the solute is modeled as mass flow at the injection point, $Q \cdot c_{inj}$, where Q is the injection flow rate and c_{inj} is the injected concentration function. When the injection curve is plotted in semilog scale, the data follows almost a straight line (Figure 5.4). Due to the solution algorithm employed by TRANSIN-III, it is much more efficient from the computational point of view, to have the injection data at constant time intervals. For this reason, we approximated the actual injection curve as one straight line (using least squares), as shown in Figure 5-4, and then we took the injection data from this approximation at constant time steps.

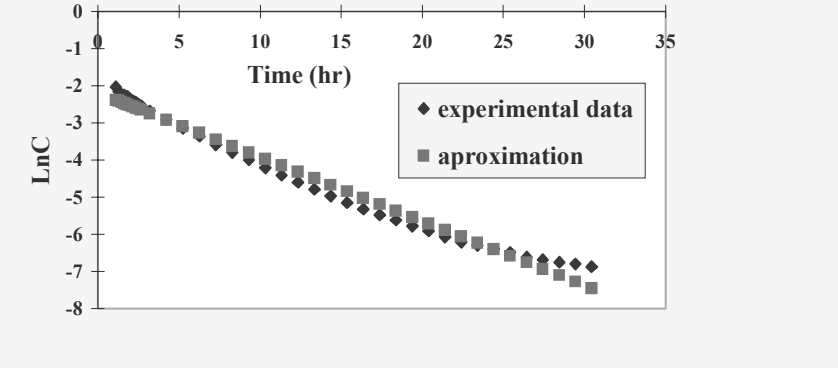

Figure 5-4. *Example of approximation of the injection curve for the transport model*

Due to this approximation, the total injected mass will differ a little bit. This slight difference in injected mass (approximated vs actual) was corrected by multiplying the injection function by a constant factor (quocient between injected masses). The rest of the injection functions and their approximations are shown in Appendix 3. It was checked that the computed concentrations were very similar using this approximation and using the actual injection function.

5.1.5 Calibration using Phase B-2 data

Both flow and transport parameters have a large uncertainty due to several reasons: measurements difficulties, large variability, scale problems, etc. For these reasons, it is convenient to calibrate any model prior to make any prediction. Phase B2 data was used to improve and check transport model capabilities and to make a detailed calibration before performing the Phase C predictions, (where sorbing tracers were used and the retardation coefficient –due to sorption- was a new uncertain parameter).

We have calibrated the transport parameters, (block and structure porosities and dispersivities), using some tracer tests from phase B2, where the conditions were very similar to those of phase C: same structures involved, similars injection and pumping rates, same injection points (KI0025F03:P5, KI0025F03:P7 and KI0025F02:P3), and same pumping section (KI0023B:P6).

The sections and structures involved, pumping and injection rates can be seen in Table 5-2. The location of the injection and pumping points in the model is shown in Figure 5-5.

Since we have employed 5 different heterogeneous conductivity fields, we decided not to calibrate a different set of transport parameter values for all them (this would have led to 5 different sets of transport parameters). The methodology that we adopted was to

calibrate the transport parameters using one of the fields and make simple simulations for the rest of fields with that set of calibrated transport parameters, i.e. the only differences between the five realizations stand on the flow parameters (conductivity field and boundary heads). The calibrated curves are shown in figures 1, 2 and 3 of Appendix 4, (tracer measured breakthrough and predictions are plotted together as concentration versus elapsed time), for the B2D, B2G and B2B tracer tests. Except may be for the tailing, at least in two of the tree cases the fit is quite good. In the test B2B the fit is worse, because we did not recover the injected mass. This is probably because the injection point is too close to the boundaries of the model.

Table 5-2 . Characteristics of B2 and C tracer test phases

Test	Inject.section	Involved Structures	Qinj ml/min	Qp ml/min	Flow geom.	Tracer
B-2b	KI0025F02:P3	21	1.6	2060	Rad Conv	NaReO4
B-2d	KI0025F03:P7	23,20,21	10	2060	Dipole	Gd-DTPA
B-2g	KI0025F03:P5	20,21	45	2060	Dipole	Helium, Naphtionate
C-1	KI0025F03:P5	20,21	45	2000	Dipole	Br-82, Na-24, K-42, Ca-47, Rb-86, Cs-134
C-2	KI0025F03:P7	23,20,21	10	2000	Dipole	Re-186, Ca-47,Ba-131, Cs-137
C-3	KI0025F02:P3	21	1,8	2000	Rad Conv	H-3, Na-22, Sr-85, Rb-83, Ba-133

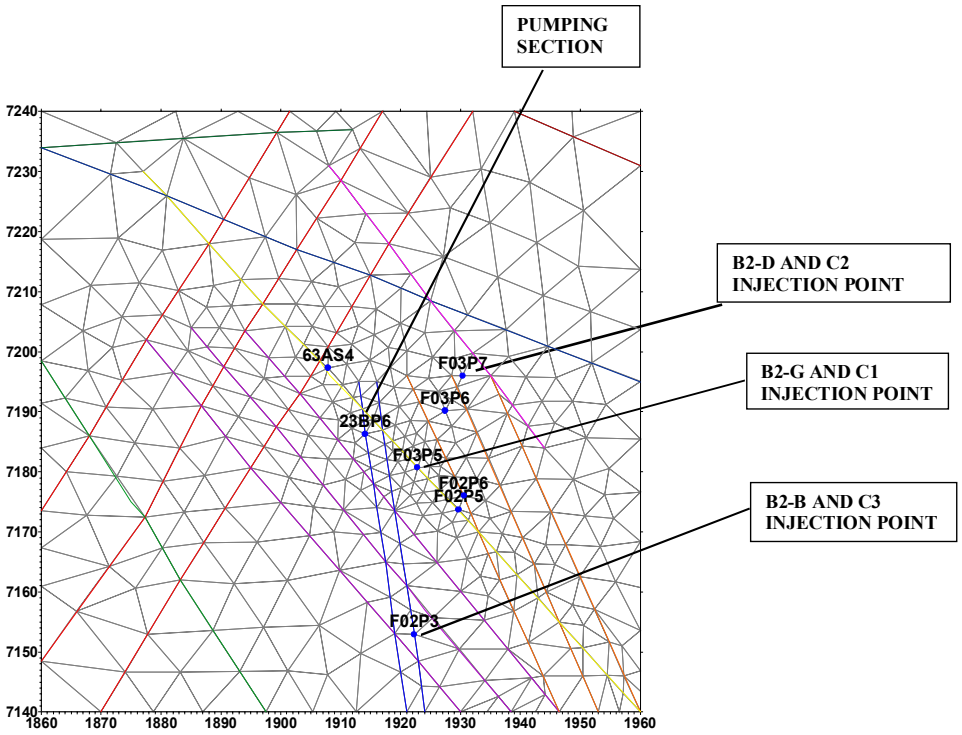

Figure 5-5. *Bi-dimensional grid and injection and pumping sections (plan view at z=–450masl, borehole names are shortened to its last 5 characters, i.e., F03P5=KI0025F03P5).*

It should be noticed that we have calibrated the three tests with a very similar parameters. Calibrated transport parameters are shown in Table 5-3.

Table 5-3 . Calibrated tranport parameters from B-2 tracer tests.

Test	Disp. Long (m)	Disp. Tra (m)	Por. block	Por fract.
B-2b	0.4	0.2	1 E-4	0.5 E-4
B-2d	0.4	0.2	1 E-4	0.5 E-4
B-2g	0.4	0.2	1 E-4	0.5 E-4

The simulations with the 5 conductivity fields are shown in figures A4-4 and A4-5 of Appendix 4. Only in one of the realizations we obtained breakthrough curve for B2B test because in the rest the mass was lost through the boundaries.

5.1.6 Phase C Test description

Three different injections with radioactive sorbing tracers were performed in the Phase C of the tracer Test Stage. On the basis of the results obtained from Phases A (Andersson et al., 2000a) and B (Andersson et al., 2000b) tests, a number of injection sections were selected for injection of sorbing tracers, which involve different structures and pathways as seen in figure 5.5. The used tracers (whose main sorption mechanism is ion exchange) have been selected to cover a wide range of retardation values, ranging from very sligthly adsorbent tracers (such as Na, Ca and Sr), to moderately adsorbent (such as Rb, Ba) and significantly or strongly adsorbent (such as Cs). All the tracers injected at one point were released simultaneously in a "cocktail". In each injection, at least one conservative non-sorbing tracer is present in the cocktail.

Phase C tests are divided into three groups according to their injection point: C-1, C-2, and C-3. Pumping was performed at section KI0023B:P6 with a pumping rate of 2.00 l/min in all of them.

In test C1, the injection section was KI0025F03:P5, crossing the structure #20, with a injection rate of 45 ml/min. Since the distance between injection and pumping sections is the shortest, short-lived isotopes of Na and Rb has been chosen so that the more long-lived isotopes can be used for the larger distances. The used tracers and their properties, are shown in Table 5-4.

In the C-2 test, the injection section was KI0025F03:P7, which is crossing the matrix in our model and crossing the #23 structure in the structural model, with a injection rate of about 10 ml/min. Structure #23 is not included explicitly in the numerical model (neither flow nor transport), but the hydraulic effect of this structure should be reflected in the conductivity fields, because they are conditioned to flow data (that is affected by this structure).The tracer inventory can be seen in Table 5-4.

In the C-3 test, the injection section, which crosses the same structure as the pumping section (structure #21), was KI0025F02:P3, with a injection rate of 1.8 ml/min.

The tracer inventory for this injection set can be seen in Table 5-4.

Table 5-4 Injected tracers and their properties

Test	Tracer	Chemical	t½ (days)	Kd (m3/Kg)*
C1	Br-82	Br-	1.47083333	
C1	Na-24	Na+	0.625	1.40E-06
C1	Ca-47	Ca2+	4.54	5.20E-06
C1	Rb-86	Rb+	18.7	4.00E-04
C1	Cs-134	Cs+	751.9	6.00E-03
C2	Re-186	ReO4-	3.78	
C2	Ca-47	Ca2+	4.54	5.20E-06
C2	Ba-131	Ba2+	11.5	2.00E-04
C2	Cs-137	Cs+	10950	6.00E-03
C3	H-3	H2O	4489.5	
C3	Na-22	Na+	949.73	1.40E-06
C3	Sr-85	Sr2+	64.9	4.70E-06
C3	Rb-83	Rb+	86.2	4.00E-04
C3	Ba-133	Ba2+	3832.5	2.00E-04

- **Table 6.1 in Byegard et al. (1998)**

5.1.7 Retention processess

The sorption is included in the transport equation and is handled through the retardation coefficient, R, wich depends on the adsorption equilibrium constant K_d [L^3/M], the porosity ϕ, and the solid bulk density, ρ [M/L^3]. Linear sorption is assumed.

$$R = 1 + K_d \rho \frac{1-\phi}{\phi} \qquad [1]$$

During the predictions of Phase C tracer tests, we were not able to include the effect of matrix diffusion in our three-dimensional model. However, we realized that the efect of matrix diffusion could be important. For this reason, we decided to approximate the effect of matrix diffusion with an "effective" retardation coefficient, instead of using equation [1]. To compute it we compared the results obtained with a semianalytical code including and not including matrix diffusion.

We used TRAZADOR code (Benet et al., 1992), that employs analytical methods to solve the transport equation with matrix diffusion process. The final computation of this "effective" retardation coefficient was done through the following steps. First, the tracer tests B2b, B2d and B2g were calibrated using a two-dimensional analytical model (one of the different possibilities of TRAZADOR code) that accounts for advection, dispersion and matrix diffusion. Once the transport parameter values were calibrated for those tests, and using TRAZADOR code, we simulated the breakthrough curve without adsorption, and the same with adsorption (retardation only in the matrix because we argue that the adsorption takes place mainly in the matrix), using the values from Technical Report TR-98-18 (shown in Table 5-4).

Finally, the chosen "effective" retardation factor for TRANSIN, was:

$$R = \frac{\text{tpeak of adsorbing tracer}}{\text{tpeak of conservative tracer}} \qquad [2]$$

The obtained values of the retardation coefficient using this expression are presented in Table 5-5.

5.1.8 Radioactive decay

All the tracers used in this phase were radioactive isotopes of different elements. The isotopes and their half-life-times can be seen at Table 5-4. Since the measured breakthrough curves of all the tracers were corrected by the radioactive decay, this value has been set to zero in the numerical model.

Table 5-5: Effective retardation coeficcient calculated expression [2]).

	Retard. coeff. [2]		Retard. coeff. [2]		Retard. coeff. [2]
C1		C2		C3	
Br	1	Re	1	HTO	1
Na	1.1	Ca	1.3	Na	1.2
Ca	1.2	Ba	12.6	Sr	1.4
Rb	12	Cs		Rb	5.4
Cs	85				

5.2 Predictions of phase C

As we used TRAZADOR code to obtain the "effective" retardation coeficient, we decided to make also predictions using this code. For this reason, we have two groups of predictions, one using the three-dimensional finite element model and one using an analytical solution. Both groups of predictions are presented in this section.

5.2.1 Predictions of phase C using the three-dimensional model

As we use the stochastic continuum approach, we will present the predictions using five realizations of the conductivity field (all the fields fit some drawdown tests as explained in the flow section). As it will be seen in the results, the behaviour of the predicted breakthrough curves can be very different with the five realizations, due to the preferential pathways that the solute may take depending on the conductivity values of each realization (remember that the boundary heads change also with the conductivity field). All these predictions were done using the effective retardation coefficient of Section 5.1.7, and the transport parameters from the B-2 phase calibration (block porosity of 10^{-4}, structures porosity of $0.5x10^{-4}$, longitudinal dispersivity of 1 m, and transversal dispersivity of 0.5 m). In this section we will discuss the different fits obtained in the tracer tests.

The breakthrough data curve of Br-82 stands between the curves of the five realizations made with the model. We may say that the actual curve shows a smaller dispersion than the model curves. Observe that the peak time also stands between the peak times of the different realizations. In addition, the tail of the breakthrough data has a larger slope than the tail of the model curves. This may suggest that there is the need of include matrix diffusion.

The breakthrough data curve of Ca-47 also stands between the computed ones, except for the tail. It shoul be also observed that not only it has a larger slope than the computed breakthroughs, but it also displays an unexpected increase at the last times, that the model cannot account for. As we will see in the next section, the fit will be improved in the evaluation, because matrix diffusion is added to model the tailing of the data curves.

The breakthrough data curve of Rb-86 test displays a behaviour quite constant (Figure A4.6.3). It has a small variation (it ranges from $3 \cdot 10^{-4}$ to $2 \cdot 10^{-3}$ approximately) while the computed curves show a larger variation. However, except for the tail, the data stands between the breaktrhough curves of the five realizations of the model. As for the previous tracer, this will be improved after including matrix diffusion in the model.

For the tracer Na-24, the appearance of data and pedictions are very similar. The predictions seem to have a larger dispersivity, but the peak time in the data is quite close to the predictions. It should be noticed that as the injection point is the same for all these tracers, (phase C1, injection at section KI0025F03:P5), even though the five realizations have a different behaviour, it is the same for all the tracers. That is, the realization whose breakthrough starts first for one tracer, starts first for all the tracers, and so on. As we will see later, when the injection point is changed, this pattern is not followed, and the realization that leads to the first arrivals for all the tracers in phase C1 is not the same as in the other phases, because the involved flow paths change when the injection point is changed.

As in the previous cases, the breakthrough data curve of Re-186 lies between the curves of the five realizations. Observe that the behaviour of the five realizations has changed, because the injectios was made at a different point. For instance, realization S11 led to the biggest peak concentrations at all points of phase C1, now it is realization S03. The data of Re-186 has a behaviour that cannot be represented by the model: the jump in concentration values at about 110 hours. However, some of the realizations are able to represent the breakthrough adequately.

The behaviour of Ca-47 is not well represented by the model at the starting times, the arrival of the data is too sharp for the model. However, the tail is well defined by all the realizations.

In phase C3 only one realization leads to a breakthrough curve, because in the other realizations, most of the mass dissapears through the boundaries. This is due to the closeness of point KI0025F02:P3 to the boundaries of the transport model and the boundary heads on it. Once again we see the big differences on behaviour of the five realizations when the injection point is changed. The comparison between the data and the model results is quite similar in the three tracers in which a model breakthrough curve was obtained. In all the cases the start of the data is sharper than the model results, the model breakthrough is also wider (probably need to reduce dispersivity) and in two cases (Na-22 and Sr-85), the peak times are shorter in the model than in the reality. In the case of H^3, the peak times are the same in both computed and measured breakthroughs.

In short, we may say that the behaviour in C1 tests is good, fairly good in C2 tests, and it should be improved in phase C3 tests. As we will see in the next section, the fits cannot only be obtained with a complex numerical model, but also with a homogeneous semianalytical one. However, the advantage of the complex model stands in two points: first, it mades the attempt to match all the tracer tests simultaneously, that is, we have obtained the results with the same parameters of the medium (only changing the parameters that depend specifically on the tracer), and second, it tries to make a more accurate representation of the reality.

5.2.2 Predictions using analytical code TRAZADOR

TRAZADOR code has several possible approaches (Benet, 1992). In this case, we selected the model with a radially convergent steady state flow, with a cylindrical symmetry with respect to the pumping well. The code assumes that the tracer injected is instantaneously mixed with the fluid volume of the pumping well.

Matrix diffusion treatment depends intrinsecally on the selected flow model. In our case one-dimensional diffusion is considered for the rock matrix. The matrix is composed by particles similar to slabs where the diffusion process is perpendicular to the slab direction. The model solves the solute transport equation under steady state conditions and dispersivity proportional to flow direction. The aquifer is idealized like an homogeneous medium, isotropic and with constant thickness. The transport model used in Trazador runs is Moench two-dimensional model under radialy convergent flow conditions (Benet, 1992).

To obtain reliable transport parameters for this analytical model we started calibrating those by using breakthrough data from the tracer tests of phase B2 (as the finite element model, but the finite element model also was used and calibrated with the data from previous tests, A-4, A-5 and B-1). The prior parameters used in TRAZADOR are shown in Table 5-6.

Table 5-6. Prior parameter information to start calibration process using Trazador.

Test C	Test B2	Flow path	Distance (m)	T_o (s)	α_L (m)	$\phi \cdot b$ (m)	D_m (-)	α_m	R	M (mg)	Section Volume (ml)
C1	B2-g	KI0025F03:P5 – KI0023B:P6	15.3	9618.66	2	0.0047	0.02136	0.0021	1.0	2674	7214
C2	B2-d	KI0025F03:P7 – KI0023B:P6	19.04	29869	4	0.0213	0.0325	0.046	1.0	3003	4978
C3	B2-b	KI0025F02:P3 – KI0023B:P6	37.56	315979	1	0.015	0.0254	0.0066	1.0	3738	8424

In the calibration runs of Trazador we estimated porosity ($\phi \cdot b$, porosity times thickness), matrix diffusion coefficient (D_m), matrix relative storage capacity (α_m) (see equation [4] of Appendix 5) and dispersivity (α_L). Trazador solves the matrix diffusion process given by the equation [10] using the Laplace inversion algorithm (see Appendix 5 for more details).

$$\alpha_m \frac{\partial C_m}{\partial t_D} = D_{mD} \frac{\partial^2 C_m}{\partial^2 x_D^2} \qquad [2]$$

TRAZADOR code uses an inverse procedure to obtain the parameters that lead to the best fit (Benet et al., 1992). Finally the process converged and the code arrived to the calibrated transport parameters of Table 5-7.

Table 5-7. Final set of estimated parameters using Trazador.

Test	Flow path	Objective Function	Distance (m)	α_L (m)	$\phi \cdot b$ (m)	D_m (-)	α_m (-)	Section Volume (ml)
B2-g	KI0025F03:P5 – KI0023B:P6	0.48E+06	15.3	1	0.003	0.069	0.389	7214
B2-d	KI0025F03:P7 – KI0023B:P6	1.03E+04	19.04	0.5	0.01	0.36	3.33	4978
B2-b	KI0025F02:P3 – KI0023B:P6	796	37.56	6.18	0.0107	0.104	0.280	3738

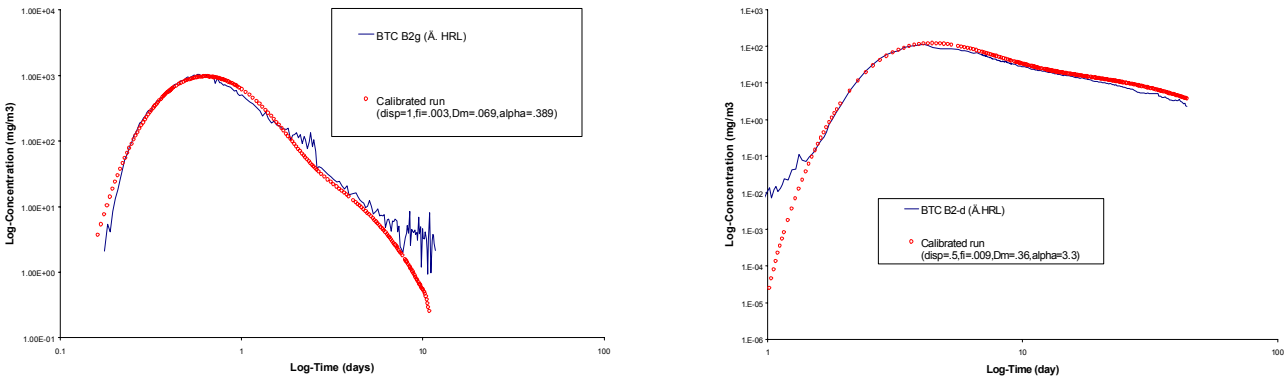

Figure 5.6. *Computed versus measured breakthroughs for tests B2g (left) and B2d (right).*

The comparison between computed and measured breakthroughs are shown in figures 5.6 and 5.7.

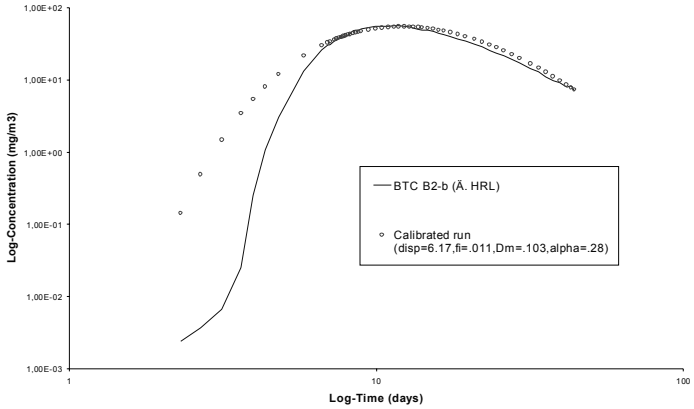

Figure 5.7. *Computed versus measured breakthrough for test B2b.*

Starting from the parameter values obtained in the calibration, we prepared the predictions. The main difference between the tracer tests used to calibrate the model and the tracer tests of phase C (to be predicted), stands on the fact that the tracers of phase C are sorbing tracers. To make the predictions we took parameter K_d from report TR-18-98. In this report two different sets of values coming from two different types of experiments were proportioned (batch sorption experiments and through diffusion experiments). Using these values, we calculated the retardation coefficient that we use in our model.

In this way, two sets of tracer parameters were obtained to start prediction process. The parameter values are shown in table 5-8.

Table 5-8. Set of tracer prior information to start the prediction process.

Test	Tracer	D_m (1)	α_m (1)	R (1)	D_m (2)	α_m (2)	R (2)
C1	Br	0.069	0.350	1.0	0.138	0.350	1.00
C1	Na	0.069	0.729	1.1	0.138	2.10	1.10
C1	Ca	0.0345	1.7505	1.2	0.069	6.61	1.20
C1	Rb	0.138	97.25	2.24	0.276	462	12.0
C1	Cs	0.069	1459	9.0	0.138	7293	85.0
C2	Re	0.3585	3.0	1	0.3585	3.0	1.00
C2	Ca	0.17925	15.0	1.01	0.17925	56.66	2.20
C2	Ba	0.17925	417	1.12	0.17925	1877	38.0
C2	Cs	0.3585	12500	2.6	0.3585	62493	2.60
C3	HTO	0.280	0.280	1	-	-	-
C3	Na	0.104	0.525	1.0	0.104	1.512	1.0
C3	Sr	0.051	1.10	1.01	0.051	6.44	1.01
C3	Rb	0.208	70	1.2	0.208	333.0	1.2
C3	Ba	0.051	35	1.12	0.051	158.0	1.12

The results of tracer predictions are shown in figures A6-1 and A6-2 of Appendix 6.

5.3 Evaluation of Phase C tracer tests

Table 5-9: Calibrated transport parameters with matrix diffusion. Porosity Φ(-), Retardation factor R (-) and Matrix diffussion coefficient Dm ()

Test	αL (m)	αT (m)	Φ block	Φ struct.	Retardation	Dm	Φ matrix
C1-Br	0.4	0.2	1 E-4	0.5 E-4	1	1.E-11	3.00E-03
C1-Na	0.4	0.2	1 E-4	0.5 E-4	2.16	1.E-11	3.00E-03
C1-Ca	0.4	0.2	1 E-4	0.5 E-4	5.33	1.E-11	3.00E-03
C1-Rb	0.4	0.2	1 E-4	0.5 E-4	334.3	1.E-11	3.00E-03
C1-Cs	0.4	0.2	1 E-4	0.5 E-4	5001	1.E-11	3.00E-03
C2-Re	0.4	0.2	1 E-4	0.5 E-4	1	1.E-11	2.00E-03
C2-Ca	0.4	0.2	1 E-4	0.5 E-4	7.5	1.E-11	2.00E-03
C3-HTO	0.4	0.2	1 E-4	0.5 E-4	1	1.E-11	3.00E-03
C3-Na	0.4	0.2	1 E-4	0.5 E-4	2.16	1.E-11	3.00E-03
C3-Sr	0.4	0.2	1 E-4	0.5 E-4	4.91	1.E-11	3.00E-03

The main difference in the model between predictions and calibration stands on the inclusion of matrix diffusion effect in our three-dimensional model. In addition, this calibration has been done using only the three-dimensional finite element code. As in the predictions, we will make some comments describing the results in all the modeled breaktrough curves. As a general statement we may say that the fit between computed and measured curves can be improved individually, that is, we can change the transport parameters adequately to obtain better fits than the ones shown in Appendix 4, but we would obtain different sets of parameters for each tracer. In the applied methodology we have obtained only an almost unique set of parameters and with those parameters most of the behaviour of the different tracers can be explained (Table 5-9). This is achieved, however, with some loss of accuracy in the fits of the individual tracers.

Another general statement is that the inclusion of matrix diffusion in the model has

improved the appearance of the model breakthrough curves, mainly at late times. Finally, in general, for tests C1 and C2, the breakthrough data stands between the curves modeled using the five realizations of the conductivity field.

In the phase C3, however, the model obtains a reliable breakthrough in only one of the five realizations, and the model peak time is only similar to the data peak time for H^3.

In the following, we will describe in some detail the results obtained in the different test and tracers.

Br-82. The peak of the data stands between the fastest and the slowest breakthrough model curves and it presents a sharper increase at the beginning. As compared with the predicted curve, it can be seen, that the tailing of the data is represented accurately (see Figure A4.9.1). In the recovery curve (Figure A4.12.1) we may see that the recovery is close to the recovery data in three of the realizations. We may also observe in this figure, the different behaviour due to the different values of the conductivities, that lead to different pathways for the tracer: In two of the realizations, some mass is lost through the boundaries. As it has been commented in the general statement, we were able to obtain better fits to the data of Br-82, but with some of the transport parameters that made some other fits even worse and we wanted to represent all the tests with a unique set of transport parameters (porosities and dispersivities).

Na-24. The data also stands between the realizations. As in most of the other curves, the sharp increase of the data at the arrival times is not modeled properly. However, the fit of the tail is also very good for this tracer, and the peak time on the realization used to calibrate the parameters is very close to the peak time of the data. Again, the improvement by including matrix diffusion in the model is notorious (Figure A4-6.4). As in the previous tracer, the recovery with the different realizations have diverse behaviours, but it is quite similar to the realization s00 (used to calibrate).

Ca-47. (Figure A4-9.5). The breakthrough data of this tracer, has an unexpected behaviour at late times (between 200 and 300 h): there is an increase of the measured concentrations that cannot be explained with the model. Even previous to this sudden increase, the tail of the data that at the beginning is well represented by the model, displays a larger slope than the model breakthrough. The behaviour at arrival times is, as in the previous cases, sharper in the data than in the model. And it is difficult to improve, because to improve it we should use smaller dispersivities, but this will affect also the tail, that is well modeled. If we compare this results with the predictions (Figure A4.6.2) it can be clearly seen the effect of matrix diffusion. We may see in Figure A4.12.3, that the recovery data is very similar to the recovery of realization s00 until the sudden increase of the Ca curve.

Rb-86. (Figure A4-9.2). As in other tracer breakthroughs, we were able to have a very good fit of the data, but to fit all the tracers with almost the same physical parameters, we loss some quality on the fit. As in the previous case, there is one strange thing in the data: there are very few measurements before the peak time, so we cannot know if the arrival is sharper in the data than in the model, as it happens in the previous cases. Comparing figures A4-9.2 and A4.6.3 we may see again the improvement in the tailing fit gained by incorporating matrix diffusion. The recovery of some of the realizations is larger than the data recovery (as opposed to some of the previously described cases), see Figure A4.12.2, but the recovery of the data has not yet ended up, so we cannot say anything definitive until we have the whole breakthrough data.

Cs.134 (Figure A4-9.4) The peak time of the data stands between the peak time of the five realizations and is very similar to the peak time of realization s00, although the peak concentration of the model is smaller than the peak concentration of the data for this realization. The slopes of the tailing for three of the five realization is very close to the slope of the data. We may say something similar to Rb-86 for the recovery. As the data recovery has not ended up, we cannot discuss the amount of measured mass in the model and in the reality. We cannot compare the model results with the predictions (as in the previous case) because we did not make this prediction, because we had some problems finding the effective retardation for this case (see Section 5.1.7).

Re-186. (Figure A4-10.1). This breakthrough data also has a sudden increase at approximately 115h that cannot be accurately represented by the model. As in all the cases, the data displays a sharper increase than the model at arrival times, but the slope of the tailing is well defined by realization s00. The rest of the realizations, as previously, cover the data and realization s00. The mass recovery (Figure A4-13.1) is larger in the reality than in all the realizations.

Ca-47 (Figure A4-10.2) As always, arrival times the data displays a sharper breakthrough than the model. The peak time of the data is well represented by three of the five realizations, and the slope of the tailings is also well represented. The recovery of the model is much larger than the observed recovery, but as this tracer has a large Kd value, it has been still monitored after this model was used.

H3 (Figure A4-11.1) As in the predictions, no model breakthrough was obtained with four of the five realizations. Only realization s00 led to a reliable breakthrough curve. In the rest of the realizations the mass was lost through the boundaries of the model.

Na-22 (Figure A4-11.2) as the rest of the cases, the data curve at starting times is sharper than the model. The model breakthrough stands always below the data, but the slope of this tailing is almost the same for both curves. The recovery (Figure A4-14.2) is a little bit less than half of the data recovery. Comparing this results with the predictions, we may see that the tailing is much better represented by the model.

Sr-85 (Figure A4-11.3) Similar observations can be made for Sr-85. Sharper breakthrough data than model at arrival times, well represented slope of the tail and slower recovery in the model than in the reality. Again, as compared with the predictions, after calibration and inclusion of matrix diffusion, the slope of the tailing is well represented.

5.4 Transport Stochastic Continuum model conclusions

As it has been shown, it is possible to use stochastic continuum models for the caracterization and modeling of fractured three-dimensional media. We have mixed a finite differences model to analyze the flow with a finite element model to analyze the solute transport behaviour. Apart from the difficulties founded due to the different nature of the two models (already mentioned in previous sections): different type and size of the discretization, different fracture treatment, etc., the model has been capable to reproduce adequately most of the tracer tests. It should be pointed out, however, that a very good reproduction of the breakthrough data can also be done with a very simple model as shown in Section 5.2. This fact does not invalidate neither the complex model, nor the simple one. The relevant question is not only reproduction of the data, that both models can do, but to make what the modeler think is a good representation of the reality, that is, physical and geometrical characteristics of the medium, that, in our opinion, the complex model can do and the simple one not.

To have a better accuracy of the transport model, the grid has been refined at the interest zone and gets coarser when approaching to the boundaries. The main problem of the transport model has been the interpretation of tracer test with injection at KI00F02:P3, that is too close to the boundaries and for this reason it has been strongly influenced by the boundary heads. Another similar problem is that we have used constant values of porosity throughout the volume (differenciating only between structures, block and matrix) but perhaps it does change significatly in space and this could perhaps allow us to have a better simulation of the breakthrough data.

References

Andersson. P., Ludvigsson, J-E., Wass, E. and Homqvist, M. 2000a. Interference tests,dilution tests and tracer tests, Phase A, Swedish Nuclear Fuel and Waste ManagementCompany, International Progress Report IPR-00-28.

Andersson, P., Wass, E., Holmqvist, M. and Fierz, T. 2000b. Tracer tests, Phase B.Swedish Nuclear Fuel and Waste Management Company, Äspö Hard Rock Laboratory,International Progress Report IPR-00-29.

Andersson, P., Ludvigsson, J.-E., Wass E., 2001. True Block Scale Project, preliminary characterisation stage, combined interference tests and tracer tests, performance and preliminary evaluation. Äspö Hard Rock Laboratory, International Progress Report IPR-01-44.

Benet, I. 1992. Desarrollo de un sistema para la interpretación automática de trazadores. Graduate thesis. Technical University of Catalonia, Barcelona

Byegård,J., Johansson, H., & Scålberg, M. 1988. The interaction of sorbing and non-sorbing tracers with different Äspö rock types. Sorption and diffusion experiments in the laboratory scale. Dept. of Nuclear Chemistry. Chalmers University of Technology, Gothenbourg, Sweden.

Bugeda, G. 1990. Utilización de técnicas de estimación de error y generación automática de mallas en procesos de optimización estructural. PhD thesis, Technical University of Catalonia, Barcelona.

Doe, T. 2001. TRUE Block Scale Project – Reconciliation of the March'99 structural model and hydraulic data. Swedish Nuclear Fuel and Waste Management Company, International Progress Report IPR-01-

Galarza, G., Medina, A. y Carrera, J. 1996. TRANSIN III: Fortran code for solving the coupled non-linear flow and transport inverse problem. El Berrocal Project, Tehnical Report 17. ENRESA.

Gómez-Hernández, J. J., Sahuquillo, A., Capilla, J. E.. 1987. Stochastic simulation of transmissivity fields conditional to both transmissivity and piezometric data. 1. Theory. Journal of Hydrology, vol. 1-4, no. 203, p. 162-174.

Gentzschein, B., 2001. Äspö Hard Rock Laboratory. True block scale experiment. Detailed flow logging of core boreholes KA2511A, KI0025F and KA3510A using a double packer system. Geosigma AB, SKB, International Progress Report IPR-01-69, Stockholm, Sweden.

Greenbaum, A., 1986. Routines for Solving Large Sparse Linear Systems. Tentacle, Lawrence Livermore National Laboratory, Livermore Computing Center, p 15-21.

Hermanson, J., 2001a. Äspö Hard Rock Laboratory. True block scale experiment. October 1997 structural model; update using characterization data from KA2511A and KI0025F. Golder Associates AB, SKB, International Progress Report IPR-01-41, Stockholm, Sweden.

Hermanson, J., 2001b. Äspö Hard Rock Laboratory. True block scale experiment. September 1998 structural model; update using characterization data from KI0023B. Golder Associates AB, SKB, International Progress Report, IPR-01-42, Stockholm, Sweden.

Hermanson, J. and Doe, T. 2000. March'00 structural and hydraulic model based on borehole data from KI0025F03. Swedish Nuclear Fuel and Waste Management Company (SKB), Äspö Hard Rock Laboratory, International Progress Report IPR-00-

Svensson, U., 1997. A site scale analysis of groundwater flow and salinity distribution in the Äspö area. Swedish Nuclear Fuel and Waste Management Co. SKB Technical Report TR 97-17.

Vives, L. 1998. Manual del TRIDI-VIII. Internal report. Technical University of Catalonia, Barcelona.

Appendix 1: Conditioning logconductivity data

Table A1-1. Co-ordinates and log conductivity conditioning data at those locations in which a fracture has been identified

x(m)	y(m)	z(m)	$\log_{10}$K(m/s)	Fracture
1953.5	7165.1	-389.6	-7.1	#6
1905.6	7248.7	-477.5	-10.7	#6
1946.0	7168.0	-472.8	-11.2	#6
1929.5	7208.5	-462.8	-6.5	#6
1984.3	7186.5	-364.8	-6.3	#7
1949.5	7196.2	-463.5	-8.0	#7
1883.5	7185.1	-488.5	-12.0	#8
1853.9	7167.9	-517.7	-8.0	#9
1863.1	7107.9	-508.4	-7.1	#10
1855.1	7236.5	-507.5	-6.7	#15
1950.1	7162.7	-392.4	-7.0	#16
1929.6	7148.4	-408.9	-11.5	#17
1903.2	7196.5	-469.0	-11.6	#18
1914.2	7185.3	-473.3	-7.6	#18
1880.2	7183.1	-491.7	-10.4	#19
1935.6	7083.5	-500.8	-6.8	#19
1893.7	7154.3	-487.4	-7.7	#19
1936.4	7153.1	-403.4	-9.6	#20
1906.5	7198.4	-465.7	-7.1	#20
1944.3	7153.9	-477.5	-8.1	#20
1916.7	7189.2	-471.6	-7.8	#20

Table A2-2. Co-ordinates and log conductivity conditioning data at those locations in which no fracture has been identified

x(m)	y(m)	z(m)	$\log_{10}$K(m/s)
1980.9	7184.1	-367.6	-8.1
1977.5	7181.7	-370.3	-9.9
1974.0	7179.4	-373.1	-9.5
1970.6	7177.0	-375.8	-8.7
1967.2	7174.6	-378.6	-9.2
1963.8	7172.2	-381.4	-7.8
1960.4	7169.8	-384.1	-9.7
1956.9	7167.4	-386.9	-10.3
1946.7	7160.3	-395.1	-9.0
1943.3	7157.9	-397.9	-9.9
1939.8	7155.5	-400.7	-10.4
1933.0	7150.8	-406.2	-11.3
1926.2	7146.0	-411.7	-10.5
1922.7	7143.6	-414.5	-7.4
1919.3	7141.2	-417.2	-8.8
1915.9	7138.8	-420.0	-8.3
1912.5	7136.5	-422.7	-9.1
1909.0	7134.1	-425.5	-9.0
1905.6	7131.7	-428.2	-9.1
1902.2	7129.3	-431.0	-10.5
1926.2	7209.8	-446.2	-7.9
1922.9	7207.9	-449.5	-9.2
1919.6	7206.0	-452.7	-10.0
1916.3	7204.1	-456.0	-9.3
1913.1	7202.2	-459.2	-9.9
1909.8	7200.3	-462.5	-8.2
1899.9	7194.6	-472.2	-11.6
1896.6	7192.7	-475.5	-9.2
1893.3	7190.8	-478.7	-8.2
1890.0	7188.9	-482.0	-9.8
1886.8	7187.0	-485.2	-12.0

1876.9	7181.2	-495.0	-8.2
1873.6	7179.3	-498.2	-7.6
1870.3	7177.4	-501.5	-9.0
1867.0	7175.5	-504.7	-7.2
1863.7	7173.6	-508.0	-8.0
1860.5	7171.7	-511.2	-10.1
1857.2	7169.8	-514.5	-8.9
1850.6	7166.0	-521.0	-7.9
1847.3	7164.1	-524.2	-9.3
1909.8	7249.7	-475.0	-9.8
1901.4	7247.7	-480.0	-10.1
1897.2	7246.7	-482.5	-12.0
1893.0	7245.6	-485.0	-12.0
1888.7	7244.6	-487.5	-9.0
1884.5	7243.6	-490.0	-12.0
1880.3	7242.6	-492.5	-11.5
1876.1	7241.6	-495.0	-12.0
1871.9	7240.6	-497.5	-10.0
1867.7	7239.5	-500.0	-11.6
1863.5	7238.5	-502.5	-12.0
1859.3	7237.5	-505.0	-11.6
1850.8	7235.5	-510.0	-9.8
1846.6	7234.5	-512.5	-11.7
1842.4	7233.4	-515.0	-12.0
1838.2	7232.4	-517.5	-11.2
1834.0	7231.4	-520.0	-11.1
1926.9	7204.6	-464.6	-8.4
1924.4	7200.8	-466.3	-9.3
1921.8	7196.9	-468.1	-11.8
1919.3	7193.0	-469.8	-11.3
1911.6	7181.4	-475.1	-9.8
1909.1	7177.5	-476.8	-8.3
1906.5	7173.7	-478.6	-9.9
1903.9	7169.8	-480.4	-11.4
1901.4	7165.9	-482.1	-11.6

1898.8	7162.1	-483.9	-12.0
1896.3	7158.2	-485.6	-10.0
1891.2	7150.4	-489.1	-10.3
1888.6	7146.6	-490.9	-10.9
1886.1	7142.7	-492.6	-10.0
1883.5	7138.8	-494.4	-11.4
1880.9	7135.0	-496.2	-11.5
1878.4	7131.1	-497.9	-12.0
1875.8	7127.2	-499.7	-11.2
1873.3	7123.4	-501.4	-9.7
1870.7	7119.5	-503.2	-11.8
1868.2	7115.6	-504.9	-9.4
1865.6	7111.7	-506.7	-7.4
1860.5	7104.0	-510.2	-10.7
1948.9	7191.5	-465.1	-11.1
1948.3	7186.8	-466.6	-11.3
1947.8	7182.1	-468.2	-11.1
1947.2	7177.4	-469.7	-11.4
1946.6	7172.7	-471.3	-11.2
1945.5	7163.3	-474.4	-11.7
1944.9	7158.6	-475.9	-10.6
1943.7	7149.2	-479.0	-11.2
1943.1	7144.6	-480.6	-11.0
1942.6	7139.9	-482.2	-11.5
1942.0	7135.2	-483.7	-10.8
1941.4	7130.5	-485.3	-11.1
1940.8	7125.8	-486.8	-10.7
1940.2	7121.1	-488.4	-11.2
1939.7	7116.4	-489.9	-11.3
1939.1	7111.7	-491.5	-11.1
1938.5	7107.0	-493.0	-11.2
1937.9	7102.3	-494.6	-11.4
1937.3	7097.6	-496.1	-11.2
1936.8	7092.9	-497.7	-9.1
1936.2	7088.2	-499.3	-10.4

Appendix 2: Perturbation of a conductivity realisation

Let $\{K\}=\{K_i, i=1,\ldots,N\}$ represent a realisation of conductivity over the N numerical cells discretizing the volume of study. This realisation is conditional, by construction, to (n_K) data values, represented by $\{K_m\}=\{K_{im}, i\in(n_T)\}$. Let $\{h\}=\{h_i, i=1,\ldots,N\}$, be the numerical solution of the groundwater flow equation on this realisation, and $\{h_m\}=\{h_{im}, i\in(n_h)\}$, be the set of (n_h) head measurements to which we wish to condition $\{K\}$. The penalty function $F=\sum_{i\in(nh)}(h_i-h_{im})^2$ will not, in principle, be close to zero, indicating that measured heads are not reproduced by the flow simulation in the given conductivity field. In such case, a perturbation $\{\Delta K\}=\{\Delta K_i, i=1,\ldots,N\}$ is added to $\{K\}$ so that the head solution in the updated field $\{K+\Delta K\}$ results in a penalty function close to zero. The perturbation $\{\Delta K\}$ is parameterised as a linear function of the perturbations at a few selected master locations (m) uniformly distributed over the volume of interest. A rule of thumb to select the master locations is to have 1 or 2 master locations per correlation length. The perturbation at any cell i is given by

$$\Delta K_i=\sum_{j\in(m)} \lambda_j \Delta K_j$$

with λ_j computed, within each fracture, by ordinary kriging with the same variogram used for the generation of $\{K\}$. To ensure that conditioning to conductivity is not destroyed by the perturbation, the set of master locations includes the conductivity data locations, i.e., $(m)\supset(n_K)$ and the perturbation at the transmissivity data locations is set constant to zero, $\Delta K_i=0$, $i\in(n_K)$. A non-linear optimisation procedure determines the perturbations ΔK_i, $i\in(m)$ that reduces the penalty function F, close to zero.

Appendix 3: Injection functions

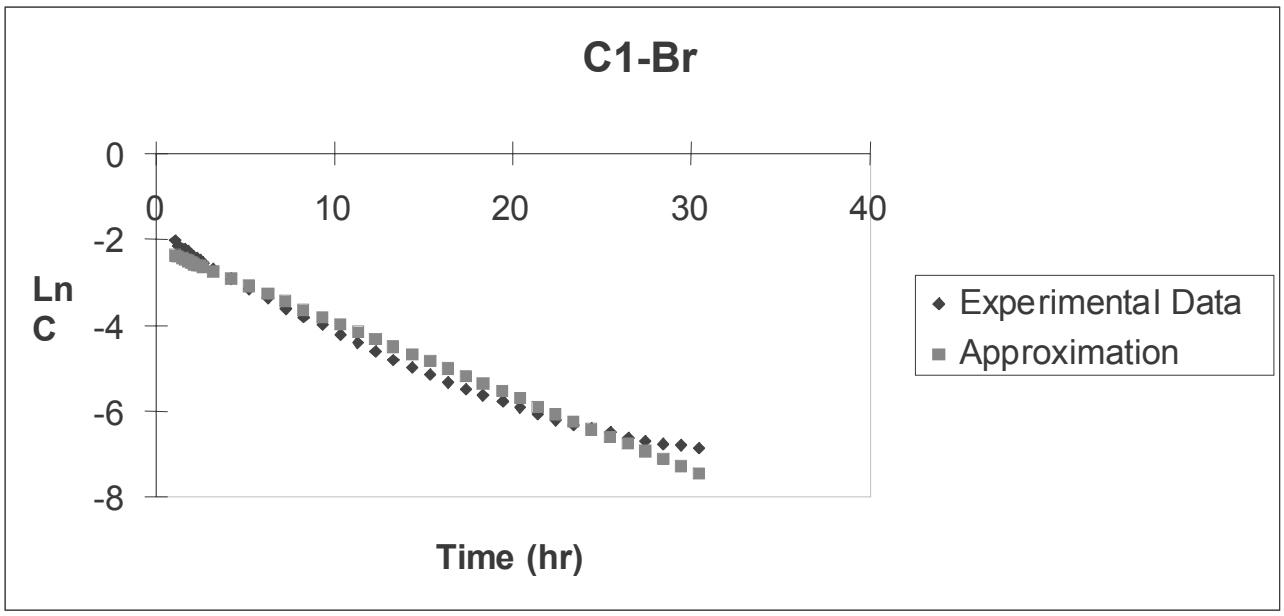

Figure A3-1. *Approximation of the observed injection curve for the numerical model. Injection of Br-82, C1 test.*

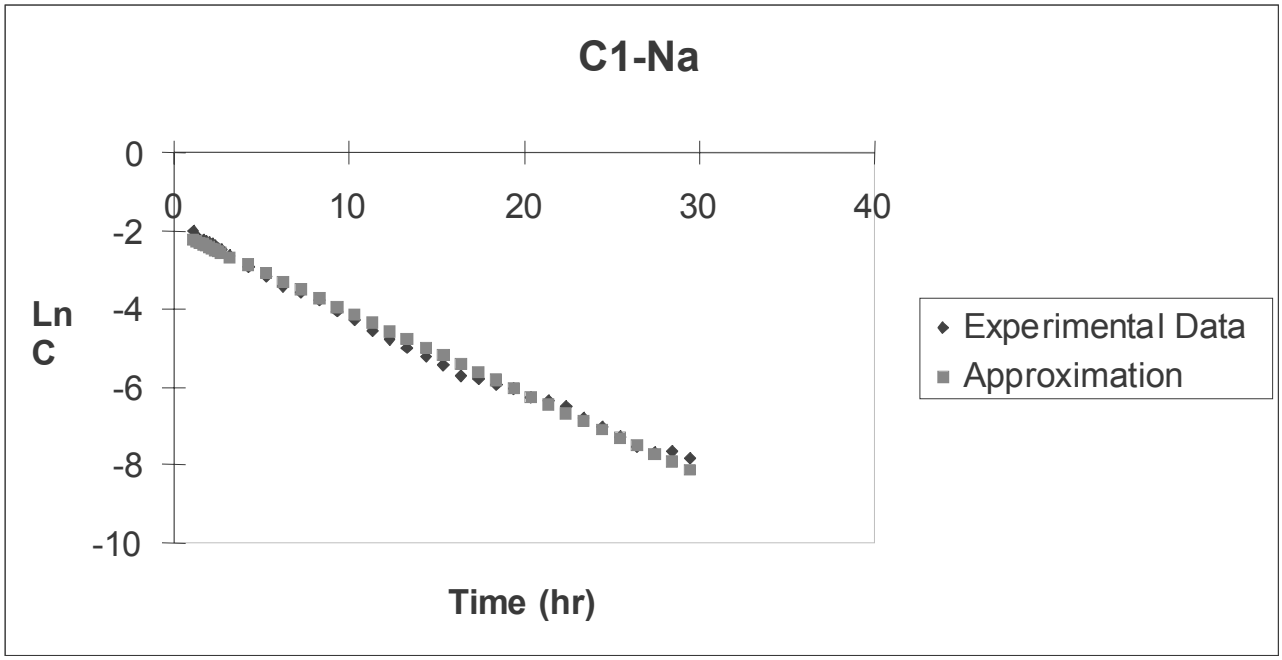

Figure A3-2. *Approximation of the observed injection curve for the numerical model. Injection of Na-24, C1 test.*

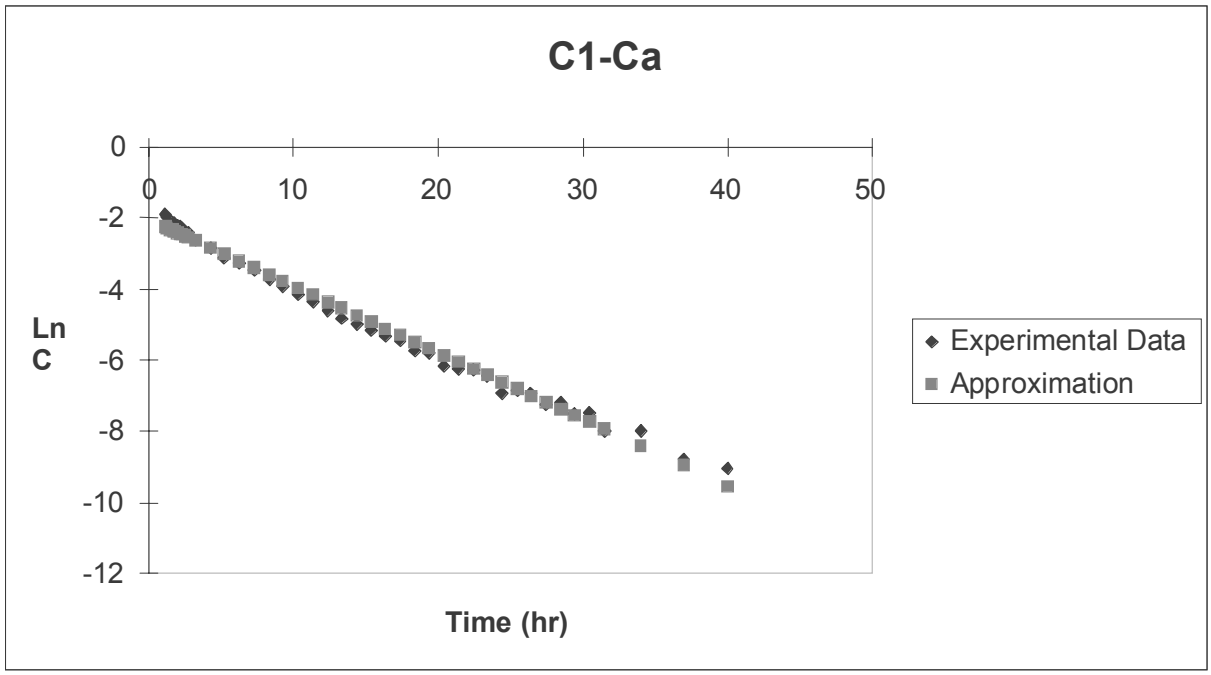

Figure A3-3. *Approximation of the observed injection curve for the numerical model. Injection of Ca-47, C1 test.*

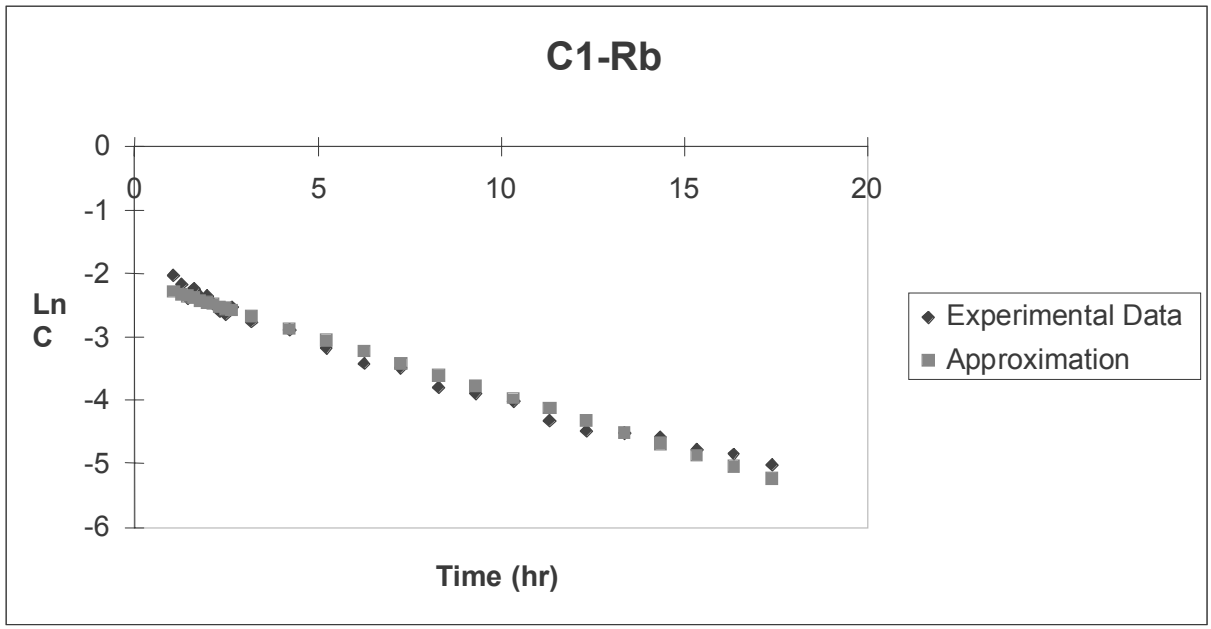

Figure A3-4. *Approximation of the observed injection curve for the numerical model. Injection of Rb-86, C1 test.*

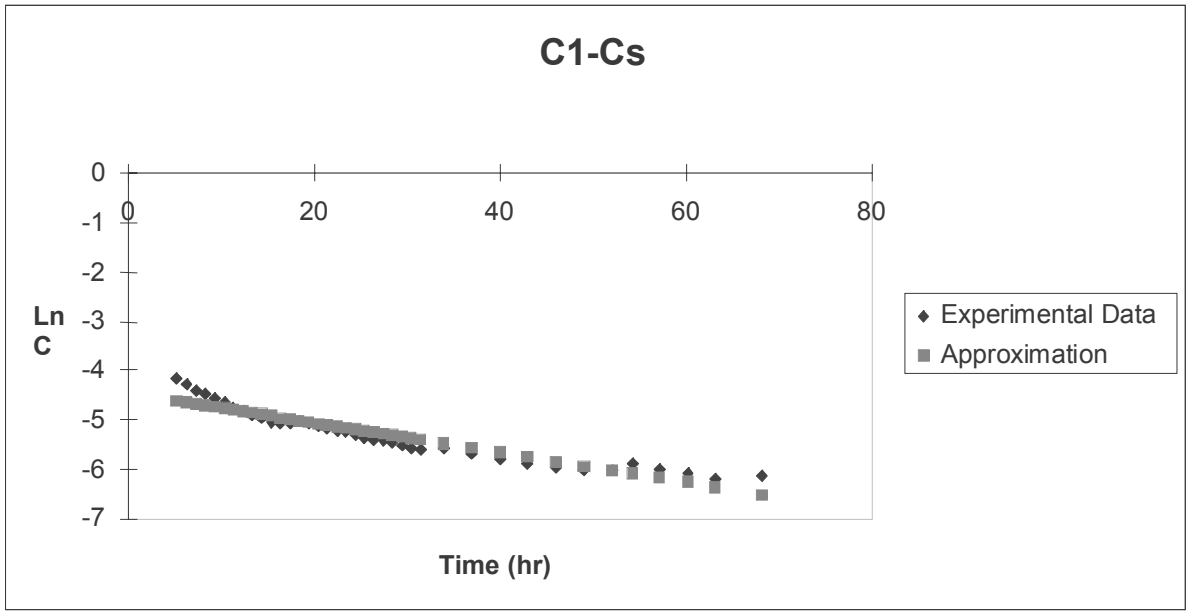

***Figure A3-5**. Approximation of the observed injection curve for the numerical model. Injection of Cs-134, C1 test.*

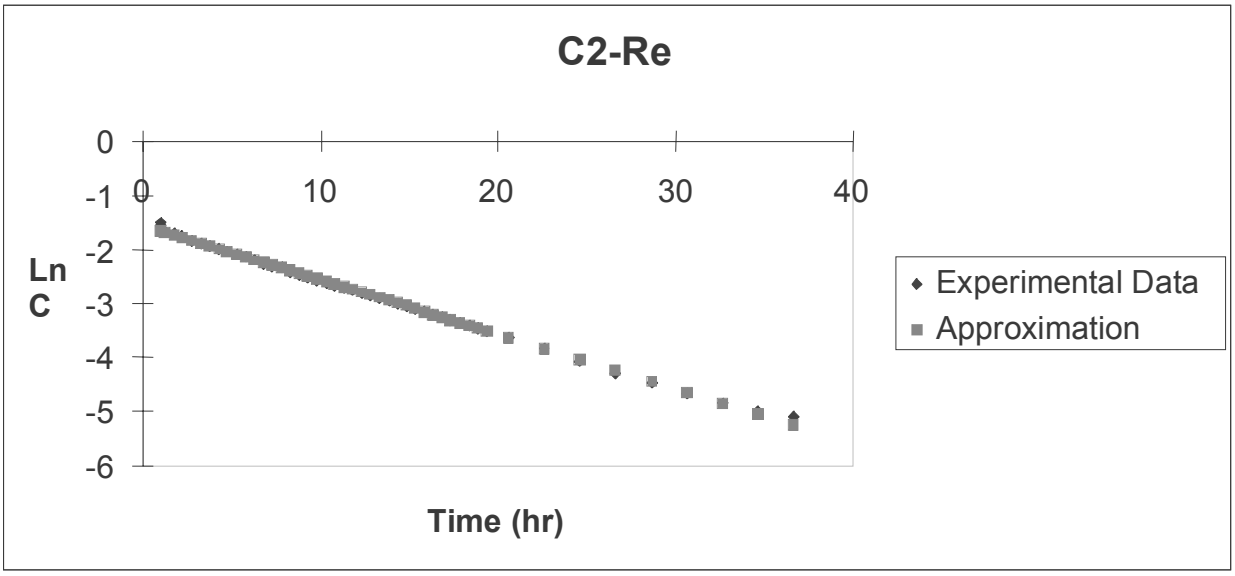

***Figure A3-6.** Approximation of the observed injection curve for the numerical model. Injection of Re-186, C2 test.*

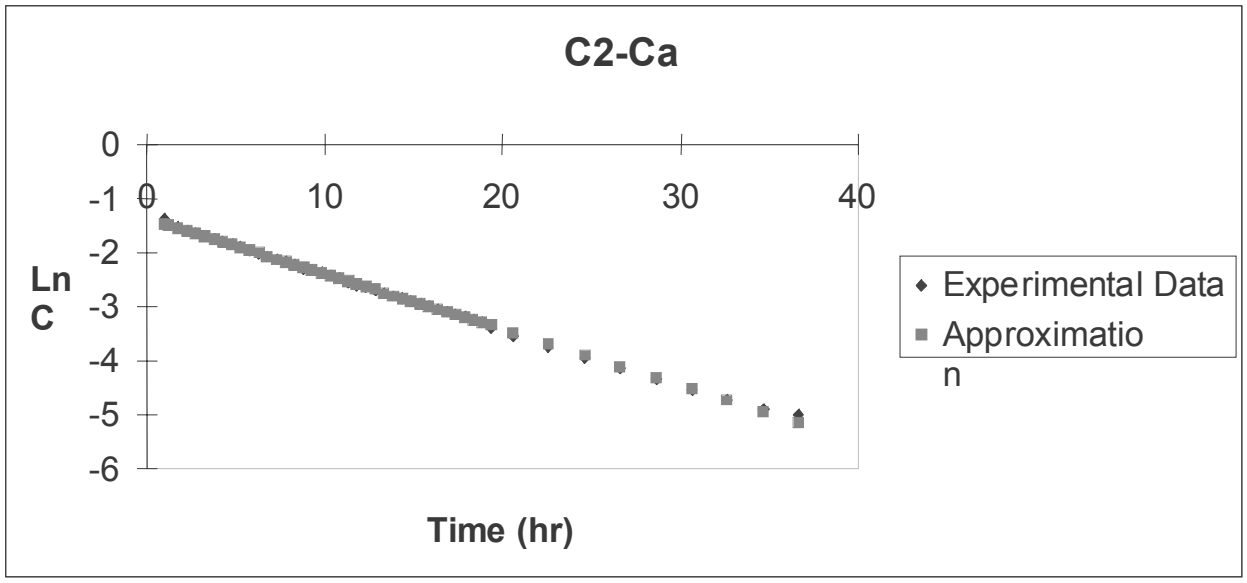

Figure A3-7. *Approximation of the observed injection curve for the numerical model. Injection of Ca-47, C2 test.*

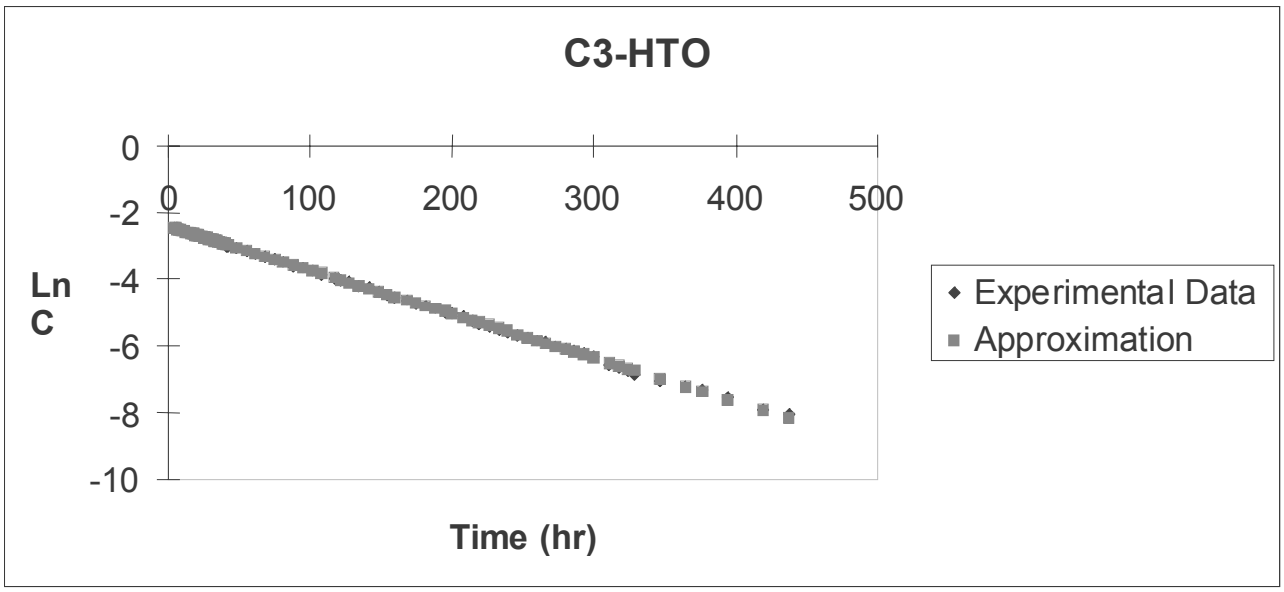

Figure A3-8. *Approximation of the observed injection curve for the numerical model. Injection of H-3, C3 test.*

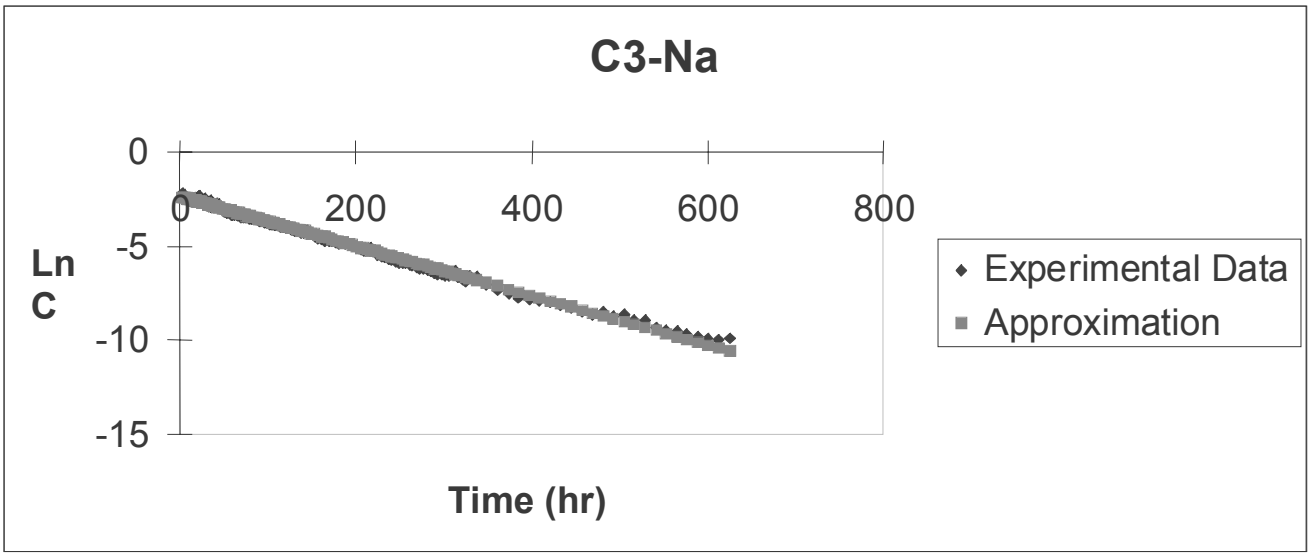

Figure A3-9. *Approximation of the observed injection curve for the numerical model. Injection of Na-22, C3 test.*

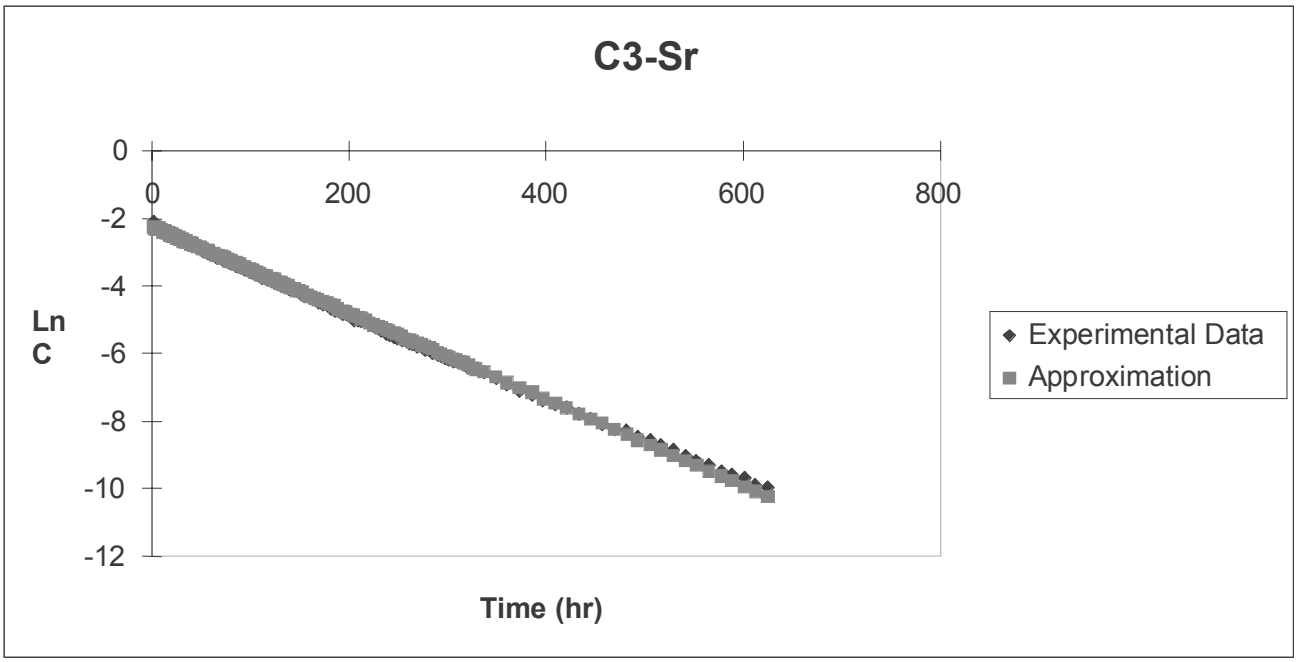

Figure A3-10. *Injection curve for the numerical model. Injection of Sr-85, C3 test.*

Appendix 4: Figures of results

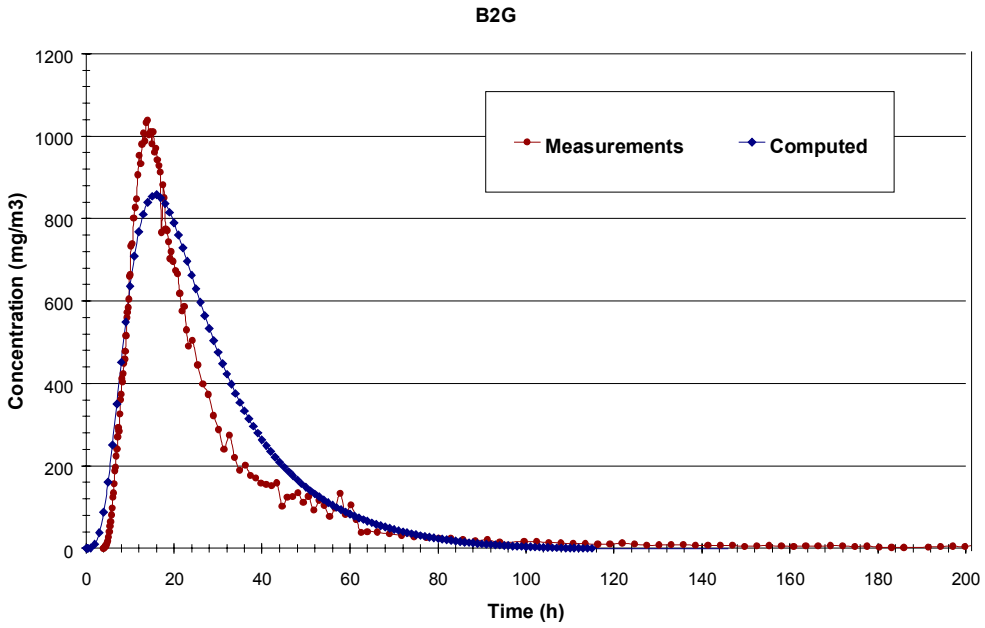

Figure A4-1. *B2-G test calibration (tracer breakthrough and predictions are plotted together as concentration versus elapsed time).*

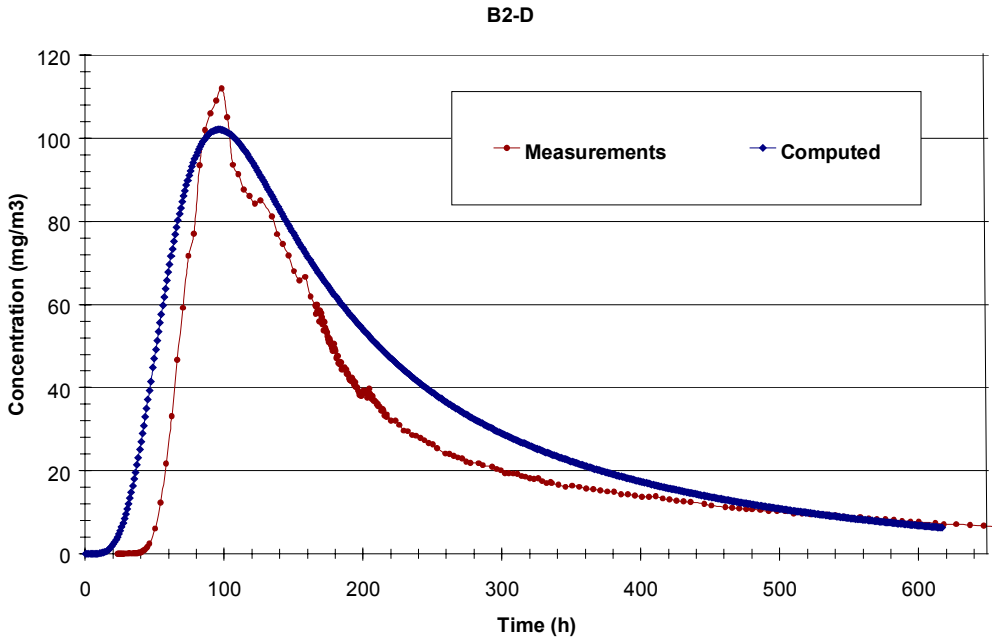

Figure A4-2*. B2-D test calibration*

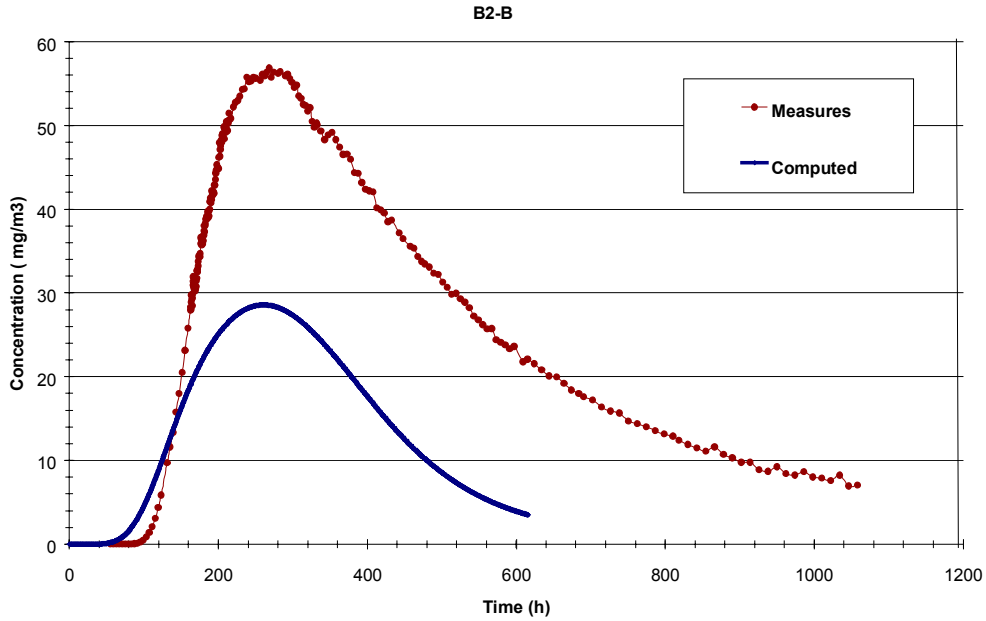

Figure A4-3. *B2-B test calibration*

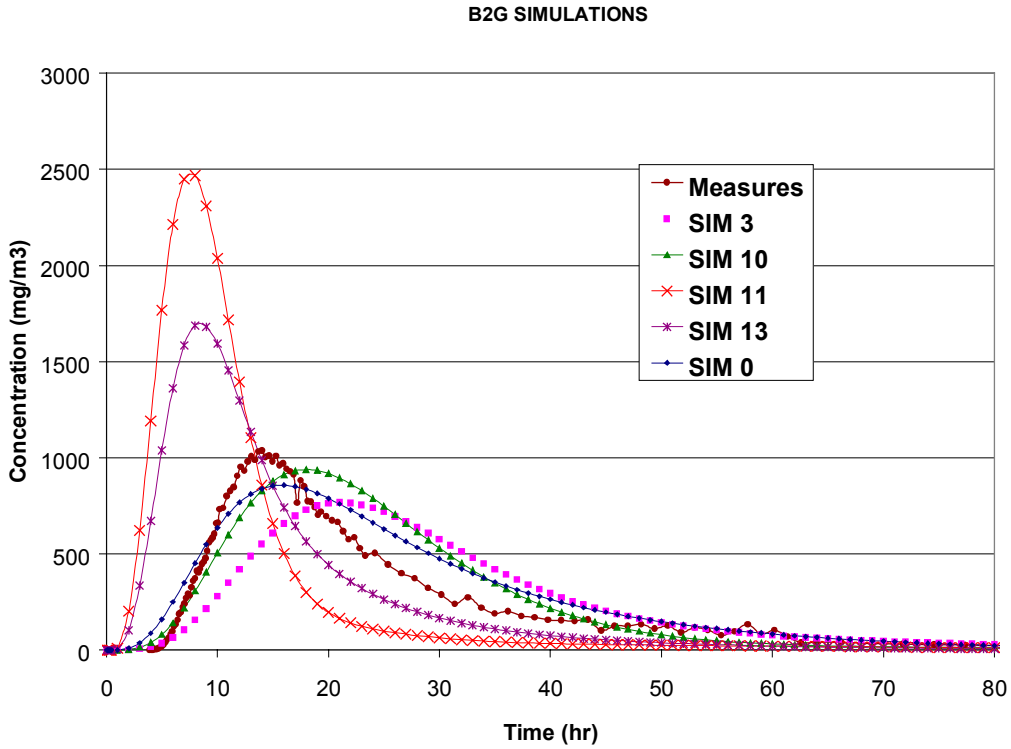

Figure A4-4. *Simulation with the 5 conductivity fields, with calibrated transport parameters for B2-G test*

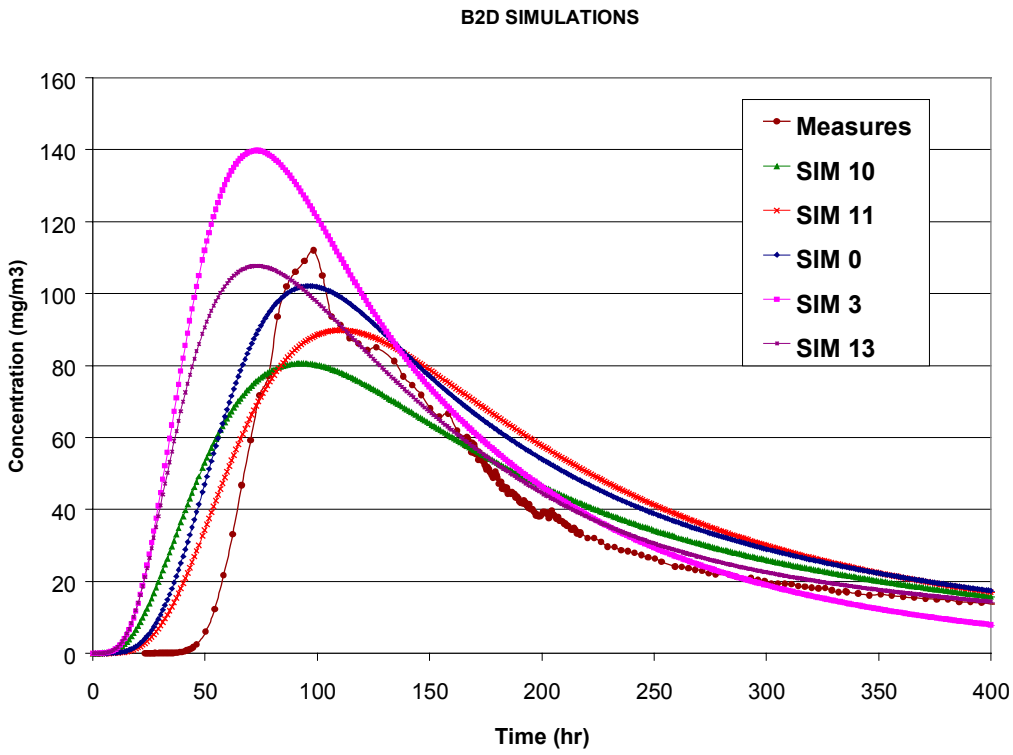

Figure A4-5. *Simulation with the 5 conductivity fields, with calibrated transport parameters for B2-D test*

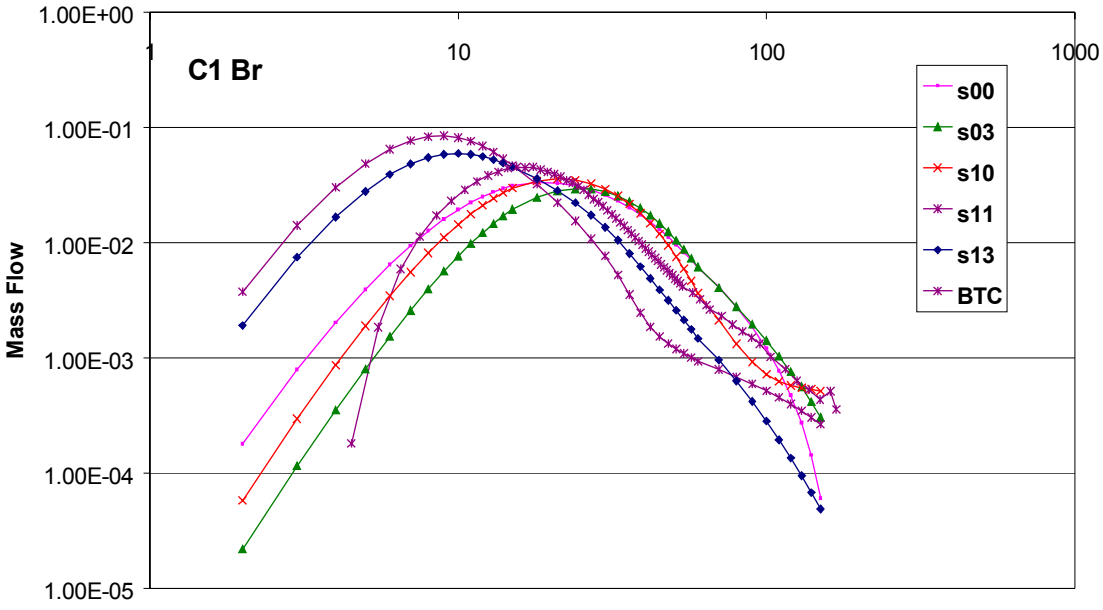

Figure A4-6.1. *Observed tracer breakthrough and predictions with the 5 heterogeneous conductivity fields for C1 test Br injection. Mass flow versus elapsed time*

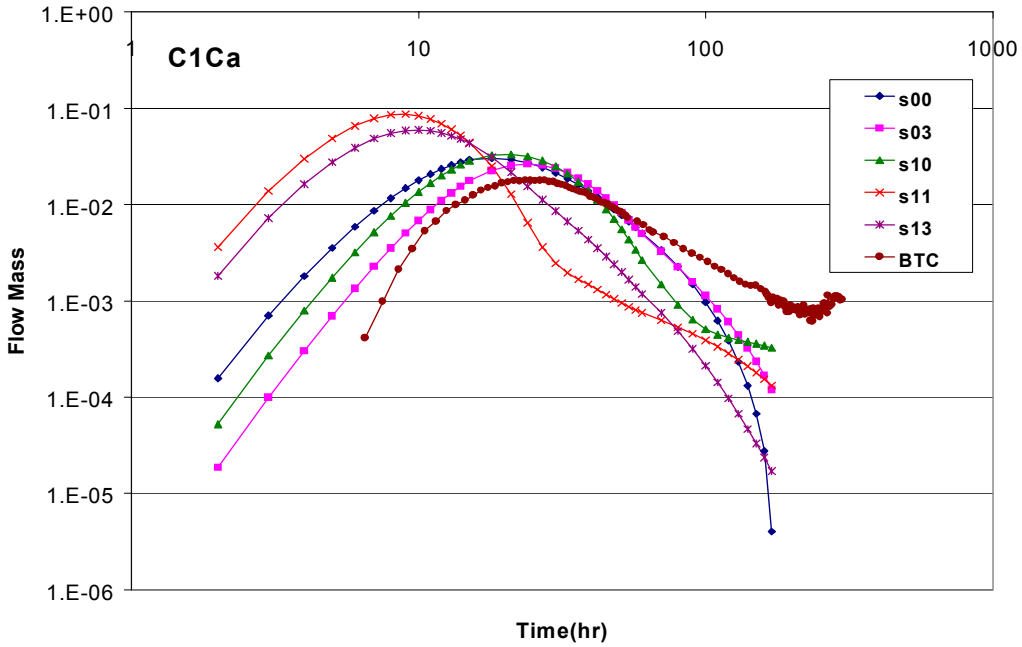

Figure A4-6.2. *Observed tracer breakthrough and predictions with the 5 heterogeneous conductivity fields for C1 test Ca injection. Mass flow versus elapsed time*

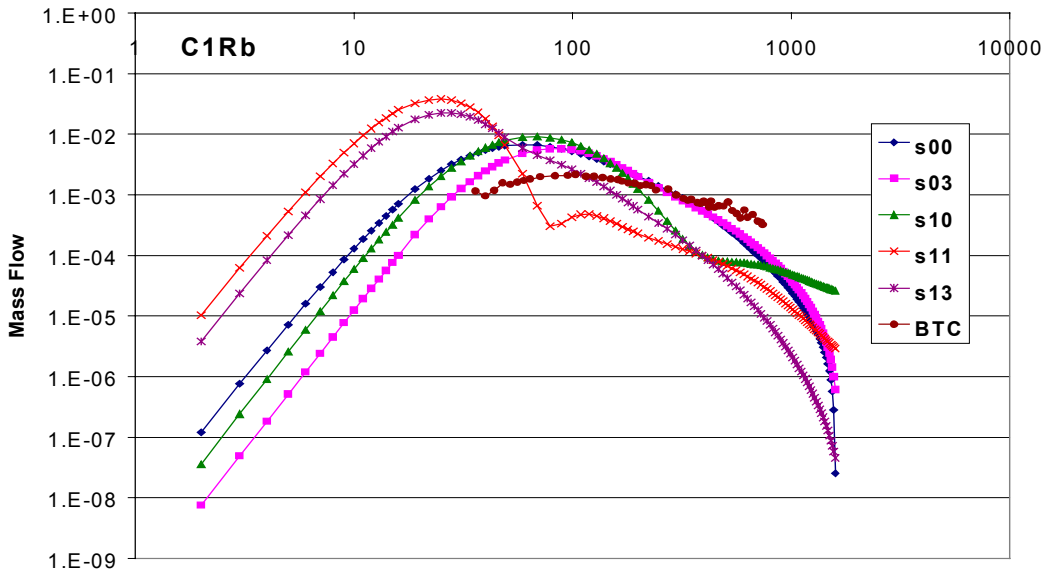

Figure A4-6.3. *Observed tracer breakthrough and predictions with the 5 heterogeneous conductivity fields for C1 test Rb injection. Mass flow versus elapsed time*

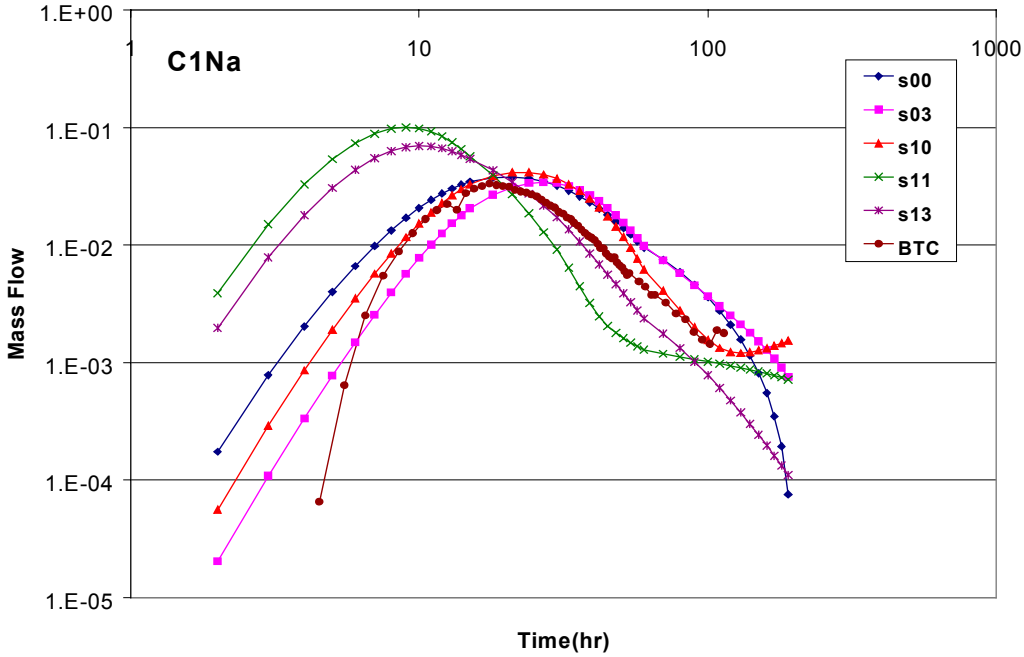

Figure A4-6.4. *Observed tracer breakthrough and predictions with the 5 heterogeneous conductivity fields for C1 test Na injection. Mass flow versus elapsed time*

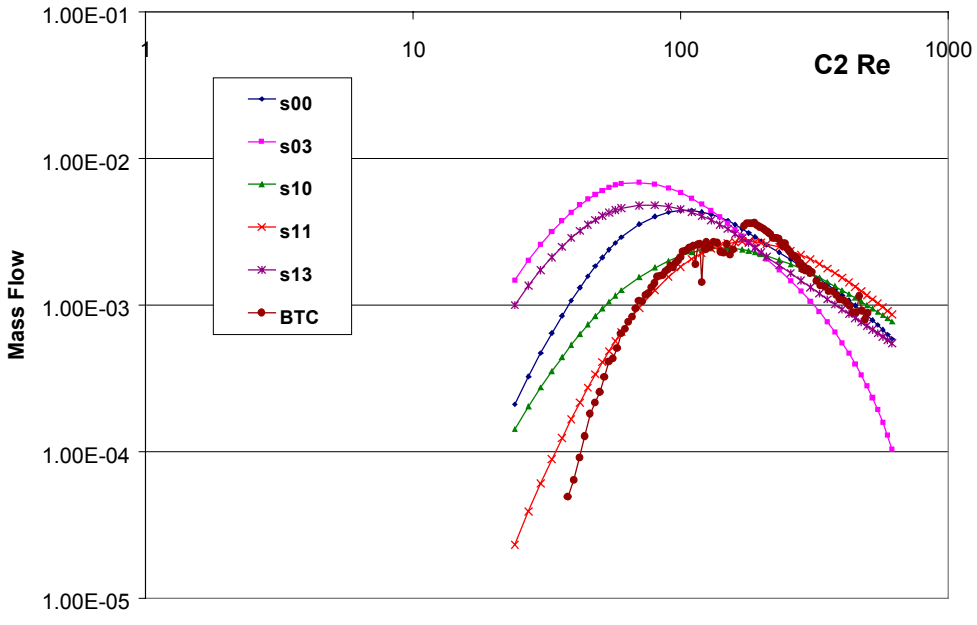

Figure A4-7.1. *Observed tracer breakthrough and predictions with the 5 heterogeneous conductivity fields for C2 test Re injection. Mass flow versus elapsed time*

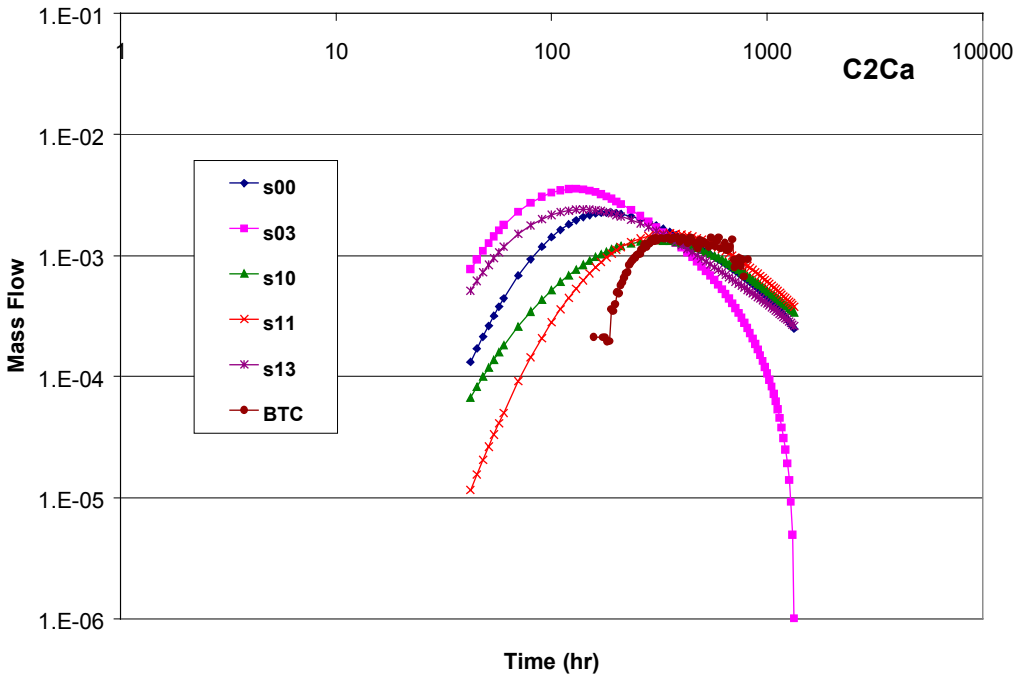

Figure A4-7.2. *Observed tracer breakthrough and predictions with the 5 heterogeneous conductivity fields for C2 test Ca injection. Mass flow versus elapsed time*

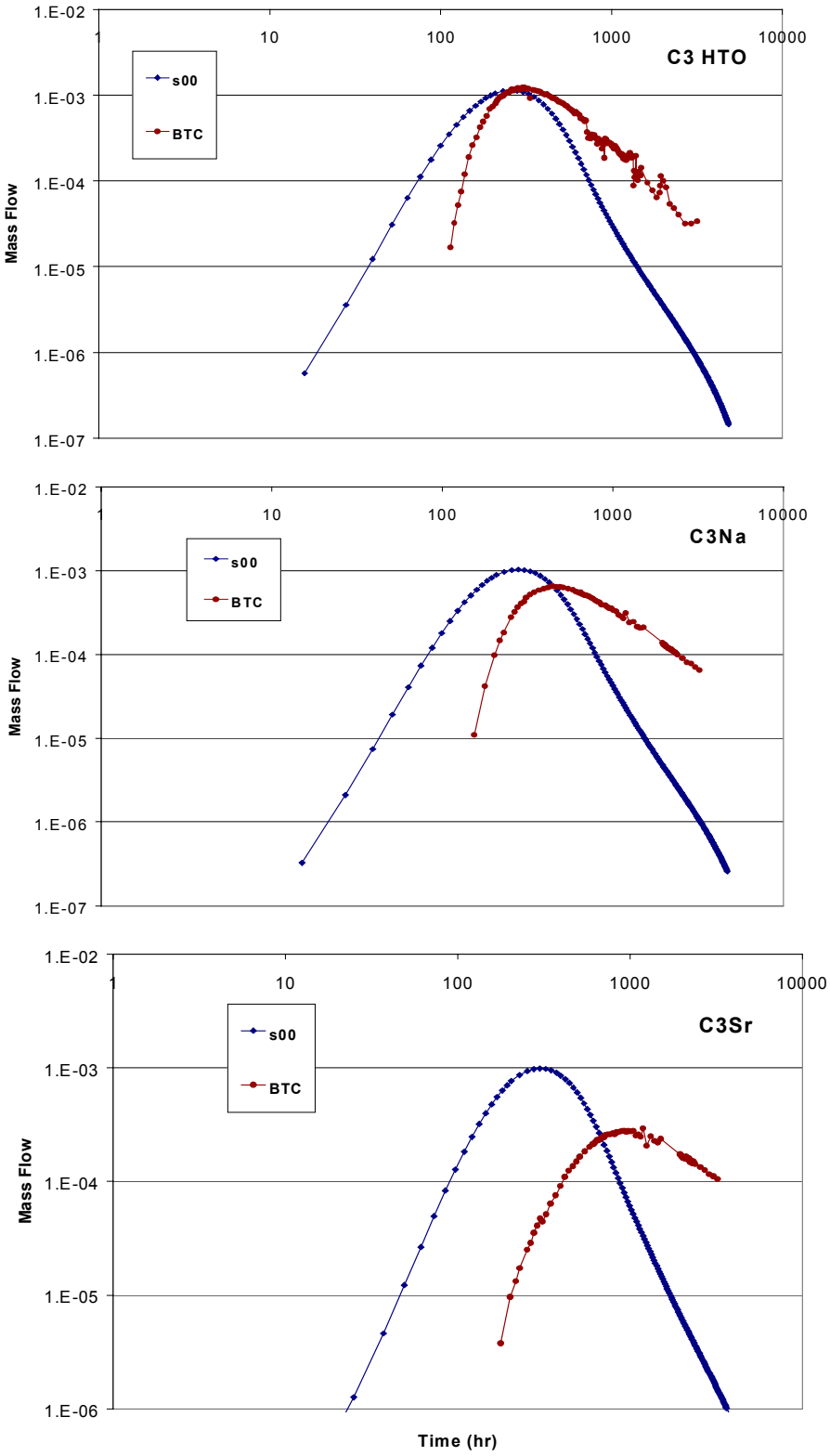

Figures A4-8.1, A4-8.2 and A4-8.3. *Observed tracer breakthrough and predictions with the unique heterogeneous conductivity field where a breakthrough was obtained in the numerical model for C3 test, HTO, Na and Sr injections.*

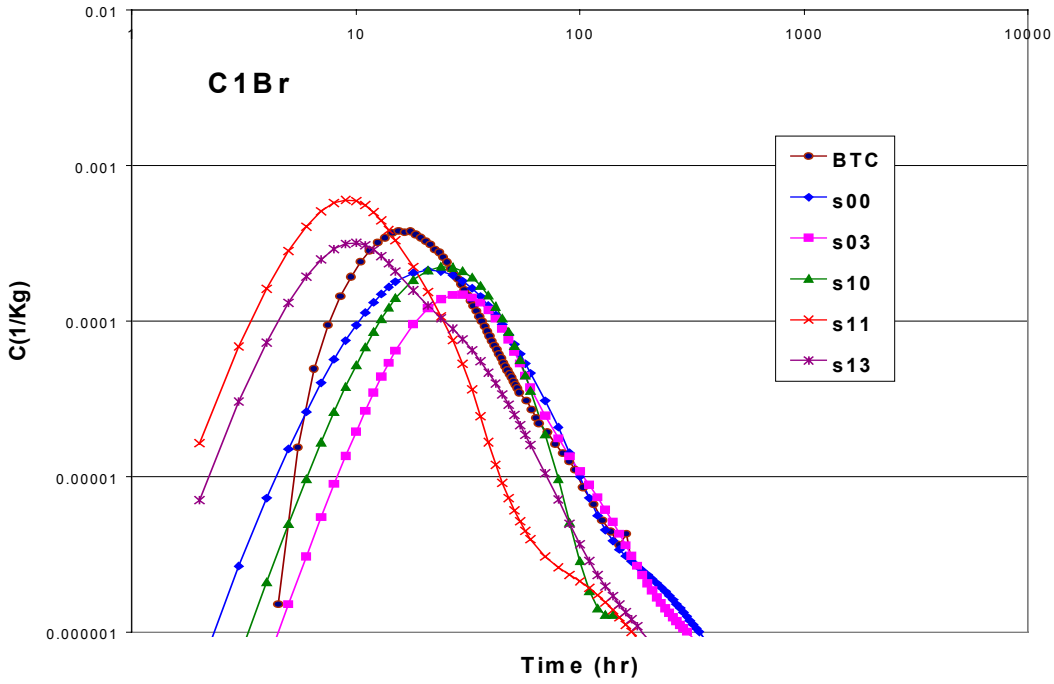

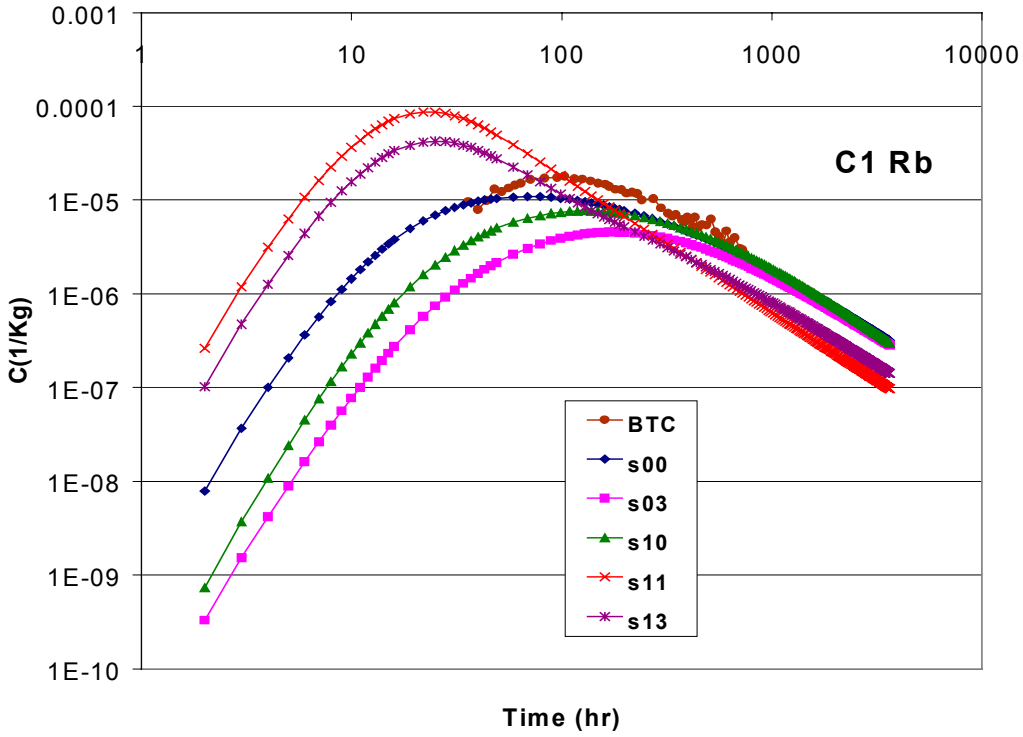

Figures *A4-9.1 and A4-9.2. Observed tracer breakthrough and calibrated curve for one of the heterogeneous conductivity fields (s00) and simulation with the other heterogeneous conductivity fields, including matrix diffusion. Test C1, Br and Rb.*

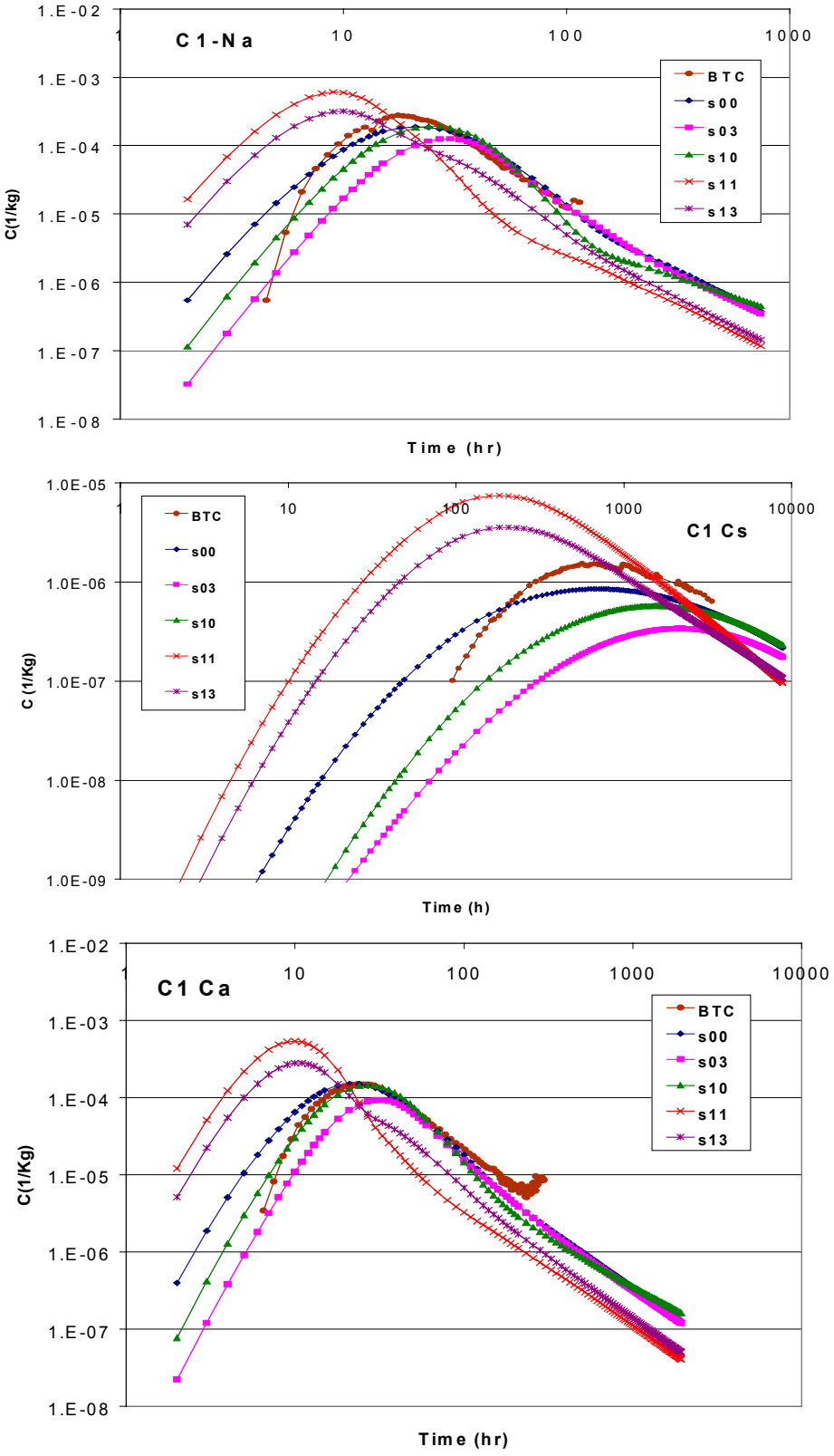

Figures A4-9.3, A4-9.4 and A4-9.5. *Observed tracer breakthrough and calibrated curve for one of the heterogeneous conductivity fields (s00) and simulation with the other heterogeneous conductivity fields. C1-Na, C1-Cs and C1-Ca.*

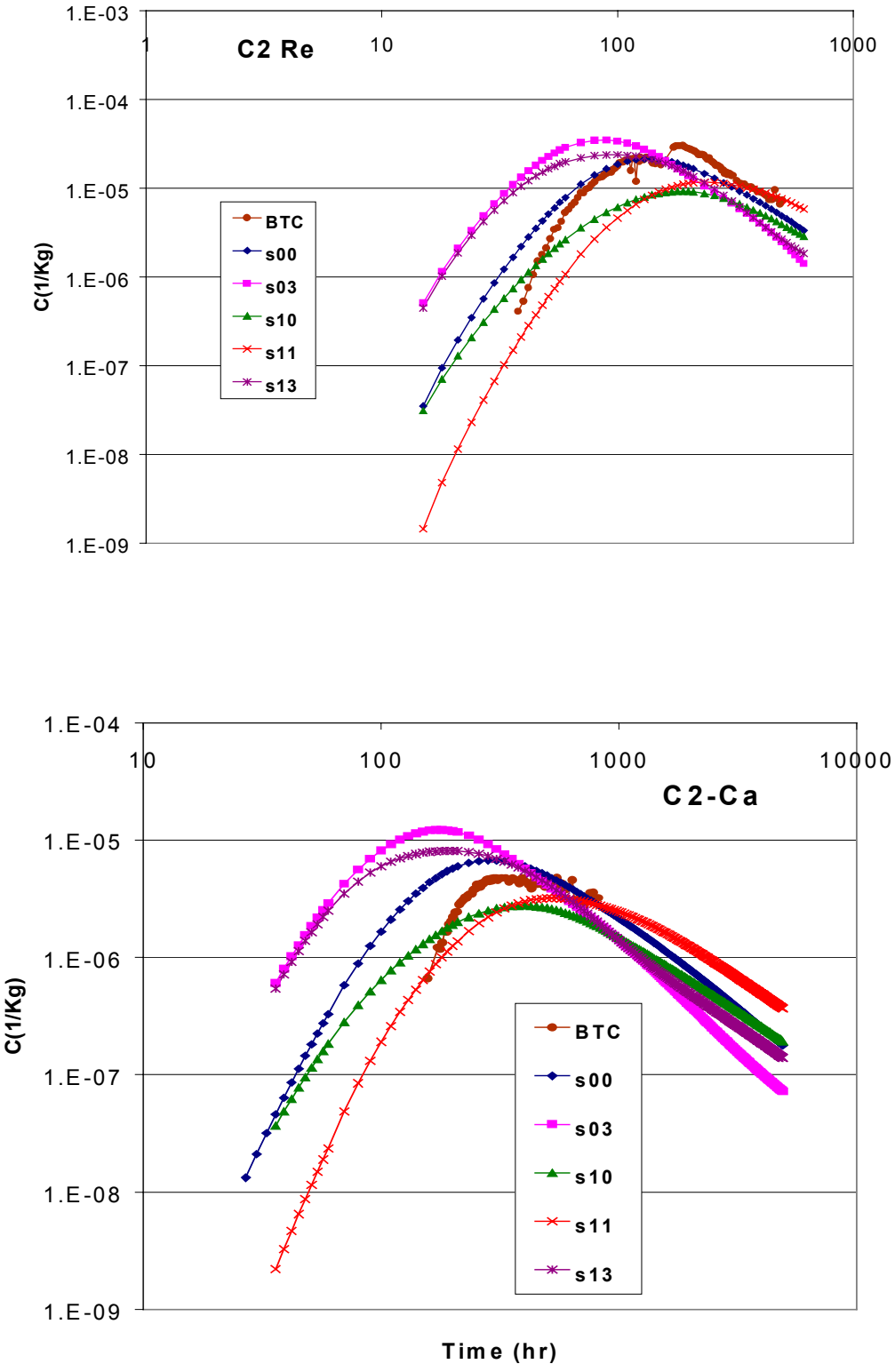

Figures A4-10.1 and A4-10.2. *Observed tracer breakthrough and calibrated curve for one of the heterogeneous conductivity fields (s00) and simulation with the other heterogeneous conductivity fields, including matrix diffusion. Test C2, Re and Ca.*

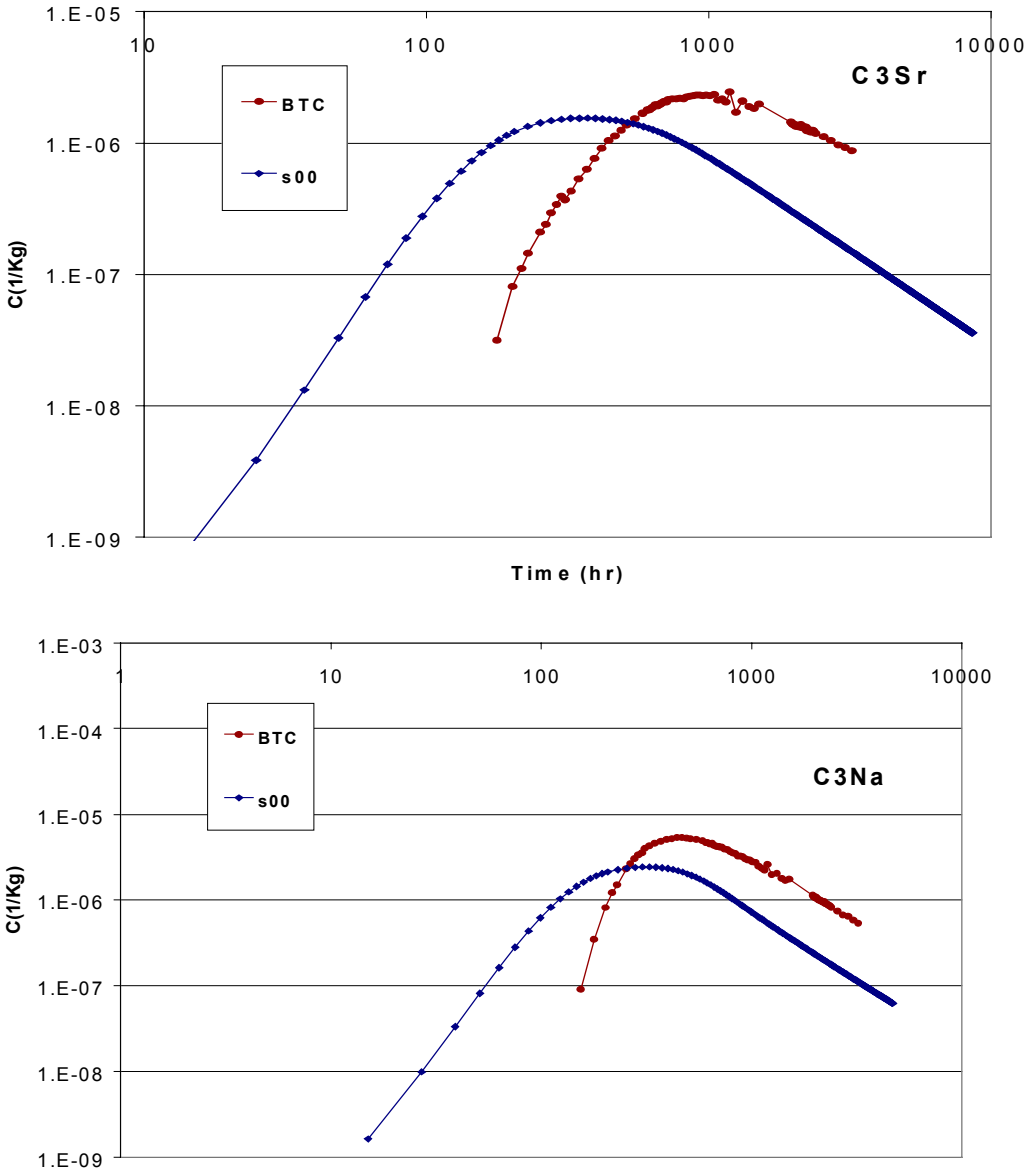

Figures A4-11.1, and A4-11.2. *Observed tracer breakthrough and calibrated curve for one of the heterogeneous conductivity fields (s00), including matrix diffusion. Test C3, Na and Sr. No breakthrough curve was obtained in the numerical model with the other four fields.*

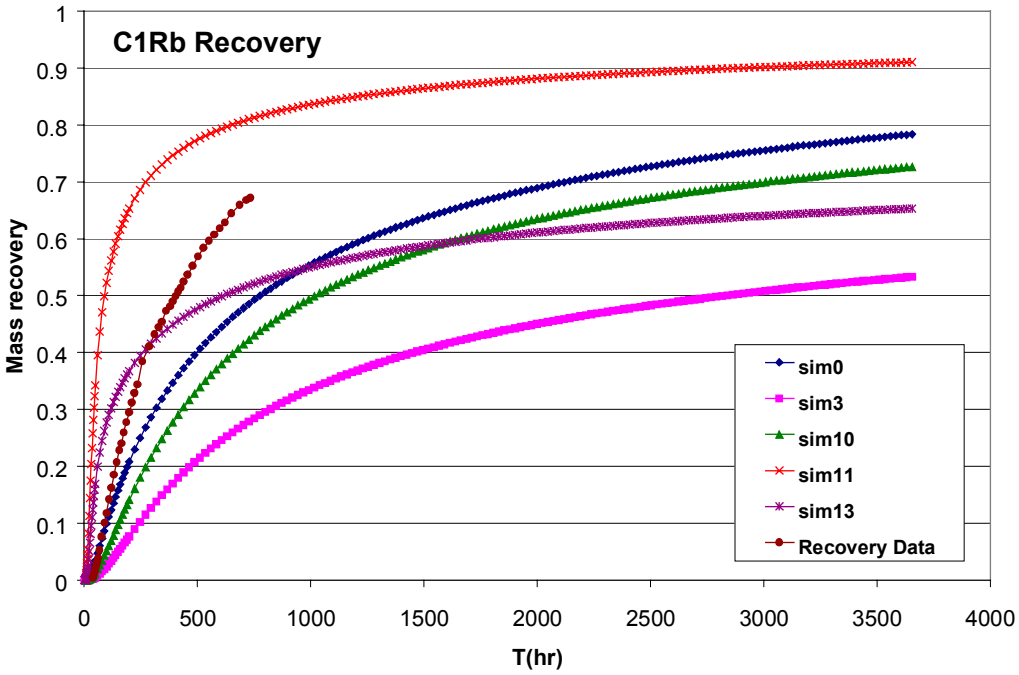

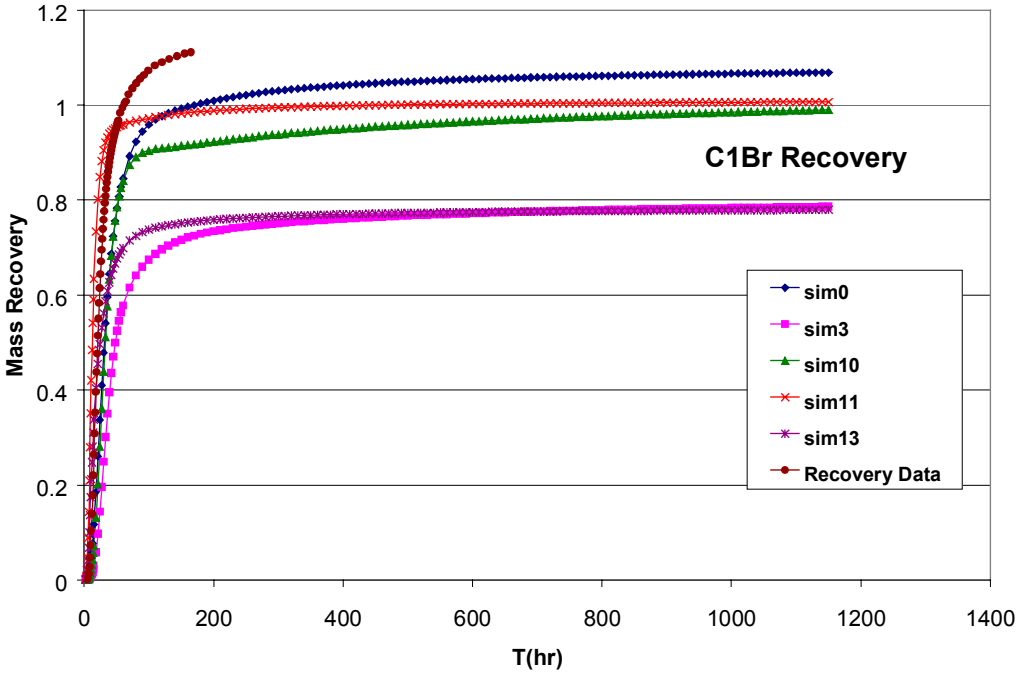

***Figures A4-12.1 and A4-12.2**: Measured and calculated recovery mass for C1 tracer test, Rb and Br (with the five K field realizations).*

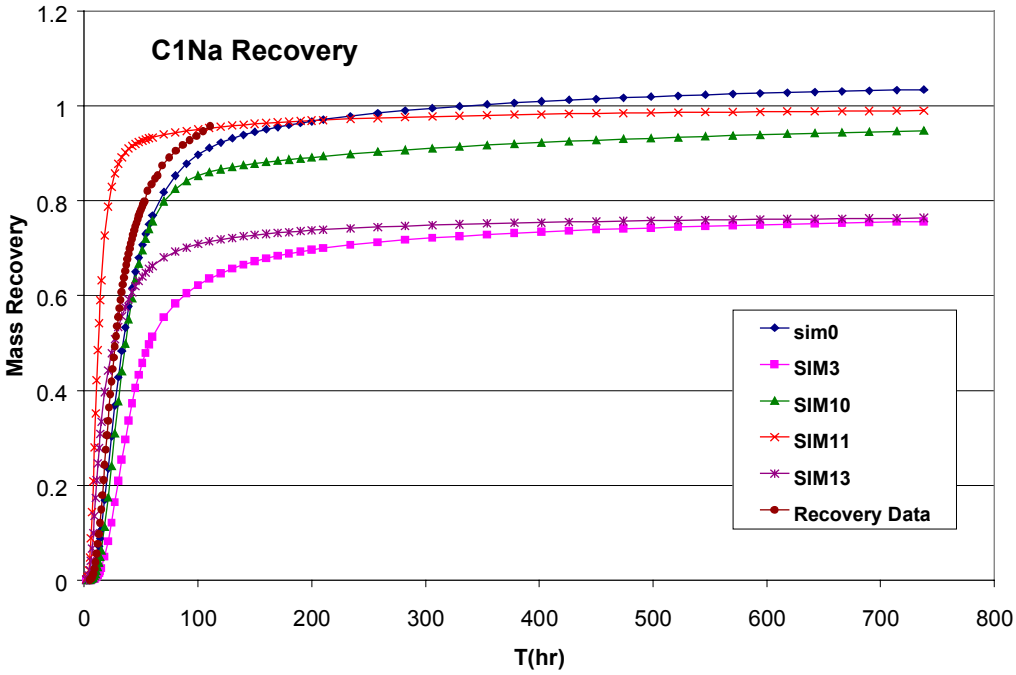

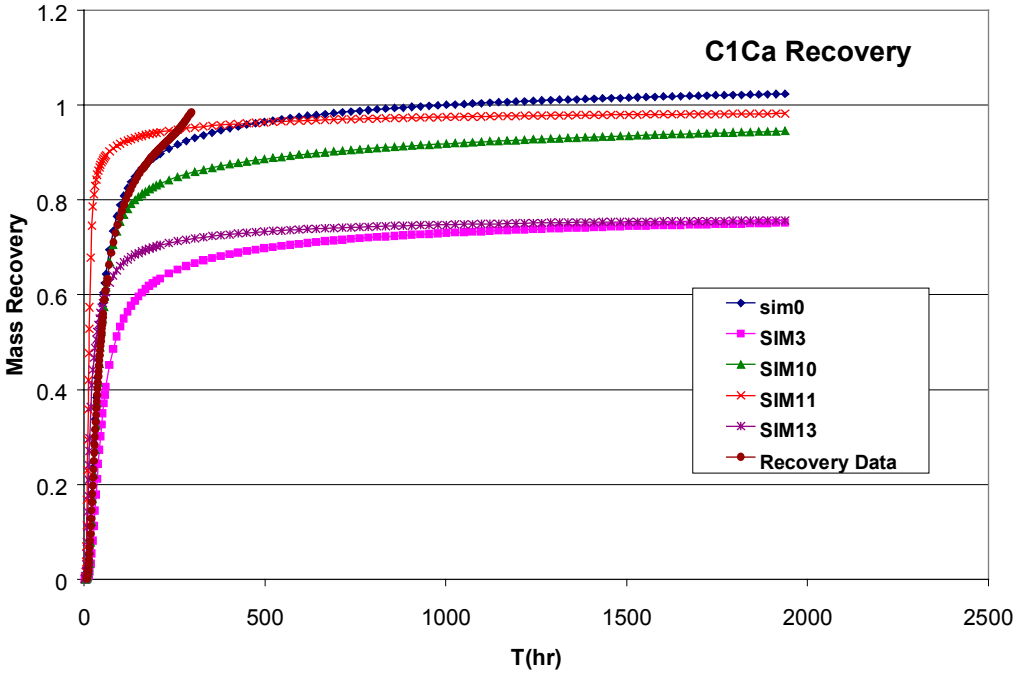

Figures A4-12.3 and A4-12.4*: Measured and calculated recovery mass for C1 tracer test, Na and Ca (with the five K field realizations).*

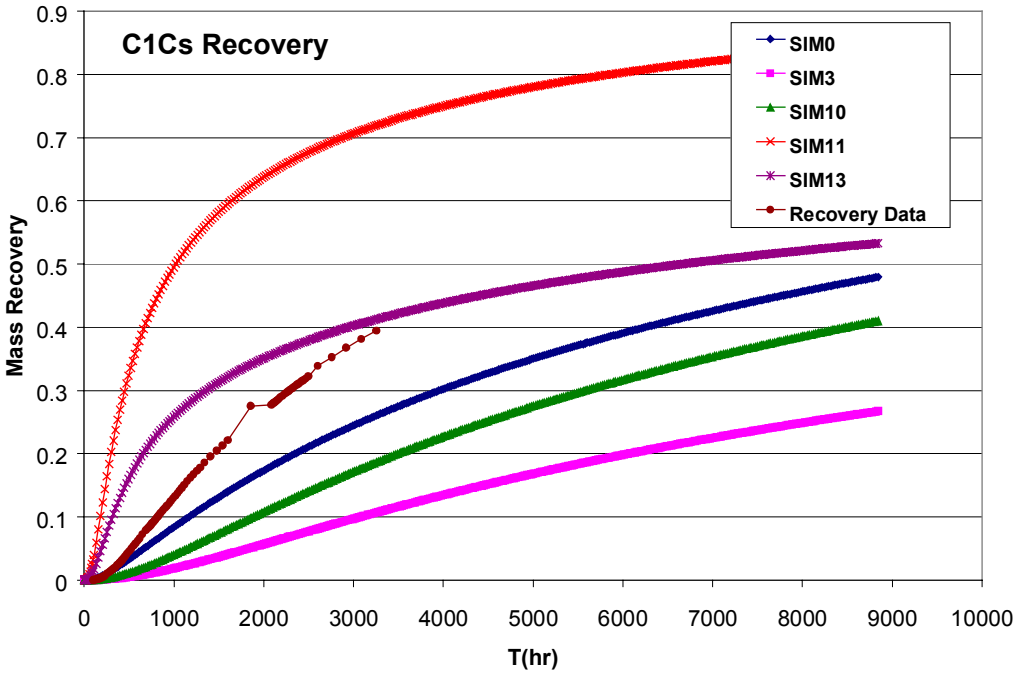

Figure A4-12.5. *Measured and calculated recovery mass for C1 tracer test, Cs (with the five K field realizations).*

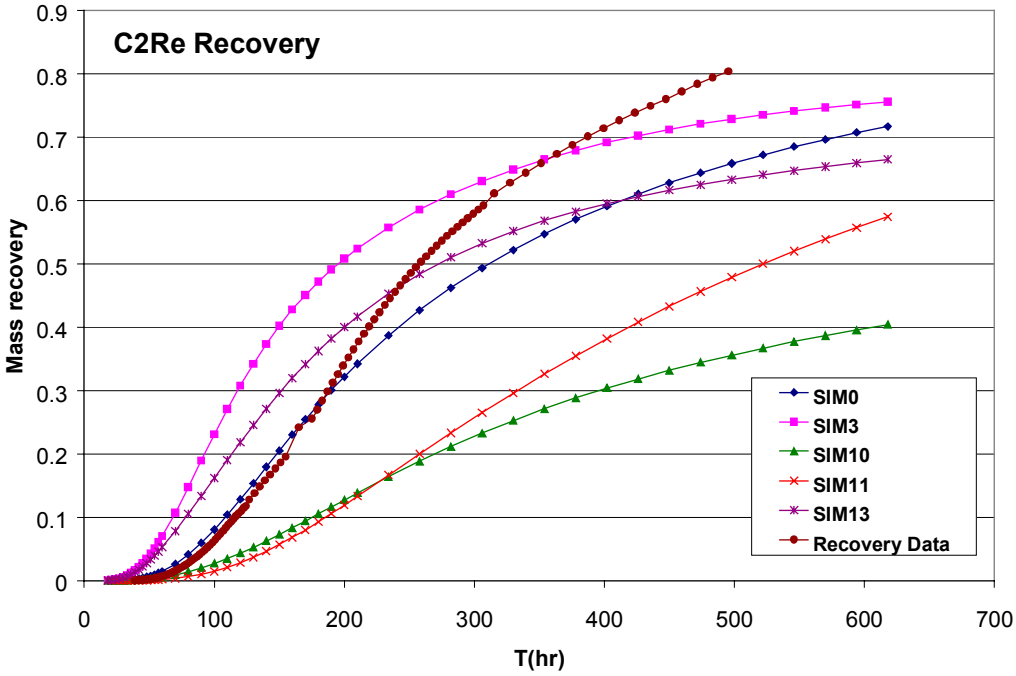

Figure A4-13.1*. Measured and calculated recovery mass for C2 tracer test, Re (with the five K field realizations)*

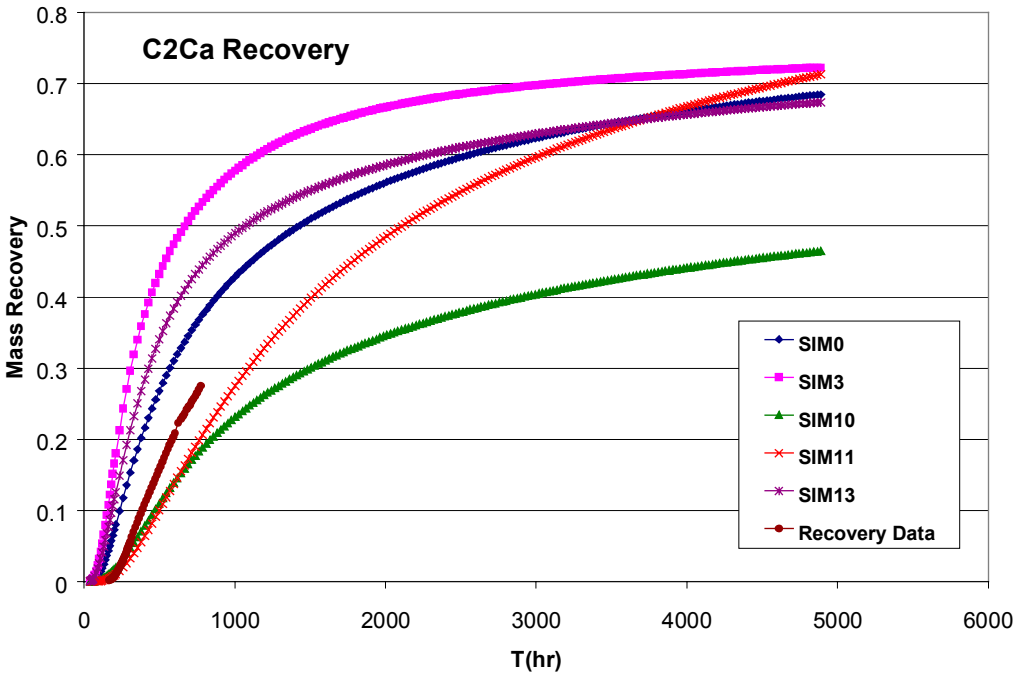

***Figure A4-13.2**. Measured and calculated recovery mass for C2 tracer test, Ca (with the five K field realizations)*

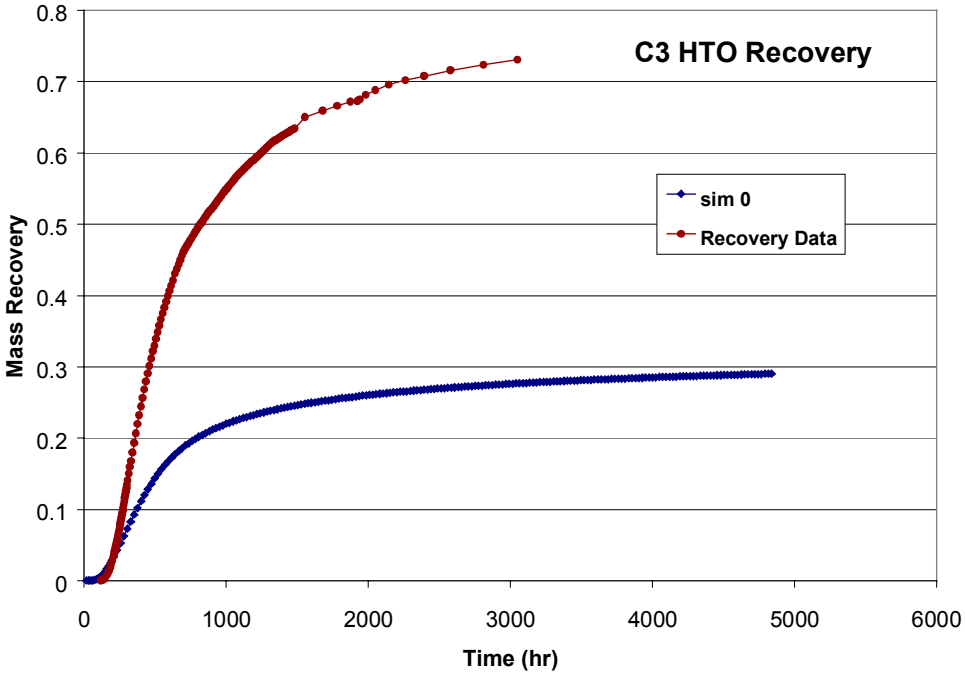

***Figure A4-14.1.** Measured and calculated recovery mass for C3 tracer test, HTO (with s00 K field realization).*

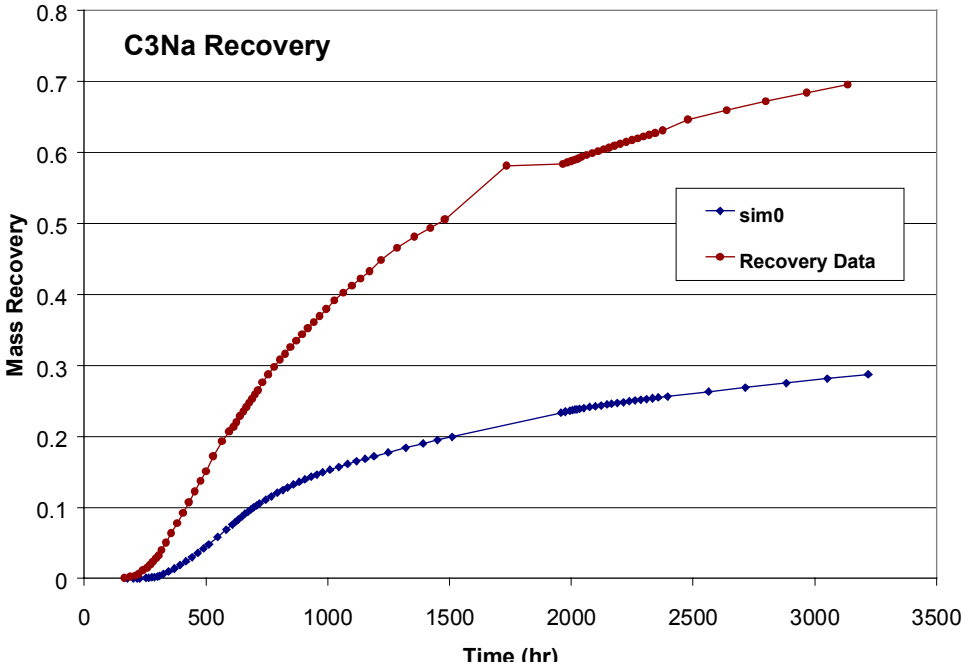

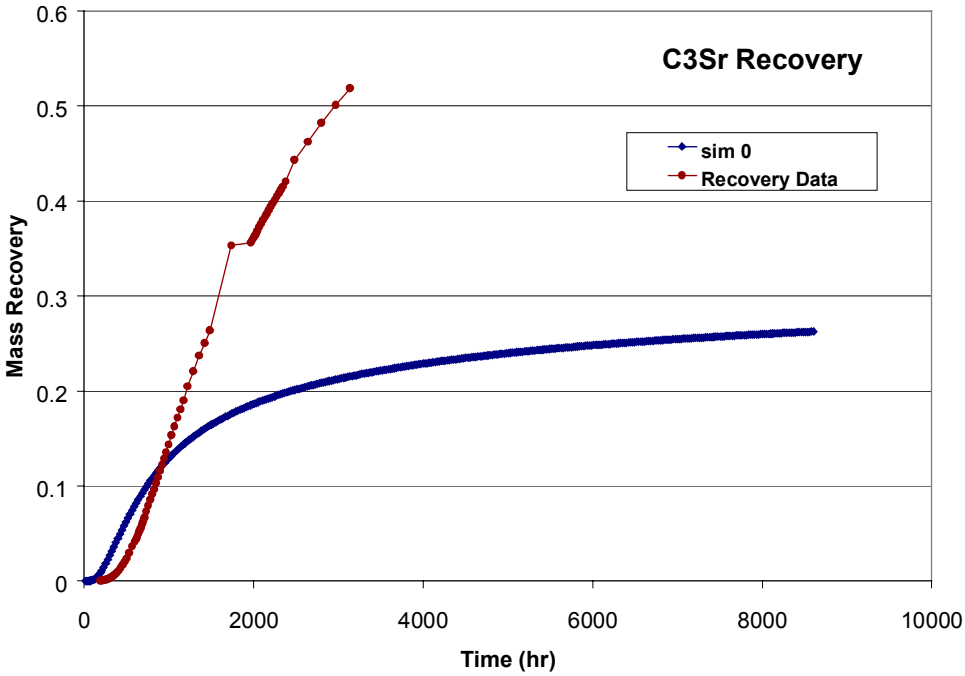

Figure A4-14.2 and A4-14.3. *Measured and calculated recovery mass for C3 tracer test, Na and Sr (with s00 K field realization, numerical tracer breakthrough was obtained only with this K field).*

Appendix 5. Trazador Code

At the start, we did not include matrix diffusion in our three-dimensional model. However we wanted to know if this effect was really important. For this purpose we make some simulations and calibration with Trazador code, that is a semi-analytical solve for transport equation under simplified assumptions (Benet, 1992).

Trazador code allows the interpretation of several types of tracer tests using analytical solutions, that is, it allows the quantitative characterization of solute transport in fractured and porous media.

The code makes the automatic of all the models. The inverse problem is based on the maximum likelihood theory (Benet, 1992). Finally, the estimation becomes an optimization problem solved by using Levenberg-Marquardt method.

This program solves several one-dimensional and two-dimensional models with analytical solution. Models included in Trazador permit to evaluate natural flow and convergent flow problems carrying adsorption, desorption and matrix diffusion.

In that case, we employed the Trazador dimensional model of Moench that includes dispersion equal to flow direction. The equation of solute transport, which is solved by Trazador, is:

$$R\frac{\partial C}{\partial t} = \frac{1}{r}\cdot\frac{\partial}{\partial r}\left(rD_L\frac{\partial C}{\partial r}\right) - v\nabla C - D\frac{\partial C_m}{\partial w_D} \qquad [1]$$

where the transport is caused by radial advection and hydrodynamic dispersion computed as:

$$D_L = \alpha_L|v| \qquad [2]$$

$$v = \frac{-q_0}{2\pi r h\phi} \qquad [3]$$

Matrix diffusion equation solved by TRAZADOR is

$$\alpha_m\frac{\partial C_m}{\partial t_D} = D_{mD}\frac{\partial^2 C_m}{\partial^2 x_D^2} \qquad [4]$$

where D_{mD} is the matrix diffusion coefficient, C_m is concentration in the matrix, and (α_m) is matrix relative storage capacity.

The tracer injection is produced under steady state conditions and several hypotheses are considered. The tracer is injected as a pulse where M is the tracer mass injected (equation [5]). The evolution of tracer mass on the boundary follows the equation [6].

$$f(t) = M\delta(t) \quad [5]$$

$$f(t) = \frac{M}{t_0}\exp\left(\frac{-t}{t_0}\right) \quad [6]$$

where t is the total test time and t_o is the renovation injection well time that is described by equation [7].

$$t_0 = \frac{SectionVolume}{Inj.flowrate(Q_i)} \quad [7]$$

The boundary conditions that Trazador code uses to solve the solute transport equation are:

$$2\pi r_L h\phi\left[D_L\frac{\partial C}{\partial r} - vC\right] = f(t) - \pi r_i^2 h_i\frac{\partial C_i}{\partial t} \quad [8]$$

$$2\pi r_w h\phi\left[D_L\frac{\partial C}{\partial r} - vC\right] = q_0 C_w - \pi r_w^2 h_w\frac{\partial C_w}{\partial t} \quad [9]$$

To solve the problem we assume that $C_i = C_w = C$ on both boundary conditions.

Finally the solution to the solute transport equation is obtained using the Hoog's et al (1992) inversion algorithm. Using matrix diffusion and Moench (1989) non-dimensional arrays the final solution is:

$$\overline{C}_D(s) = \psi\exp\left[\frac{Pe}{2}(1 - r_{wD})\right]G(s) \quad [10]$$

Appendix 6. Results using the TRAZADOR code

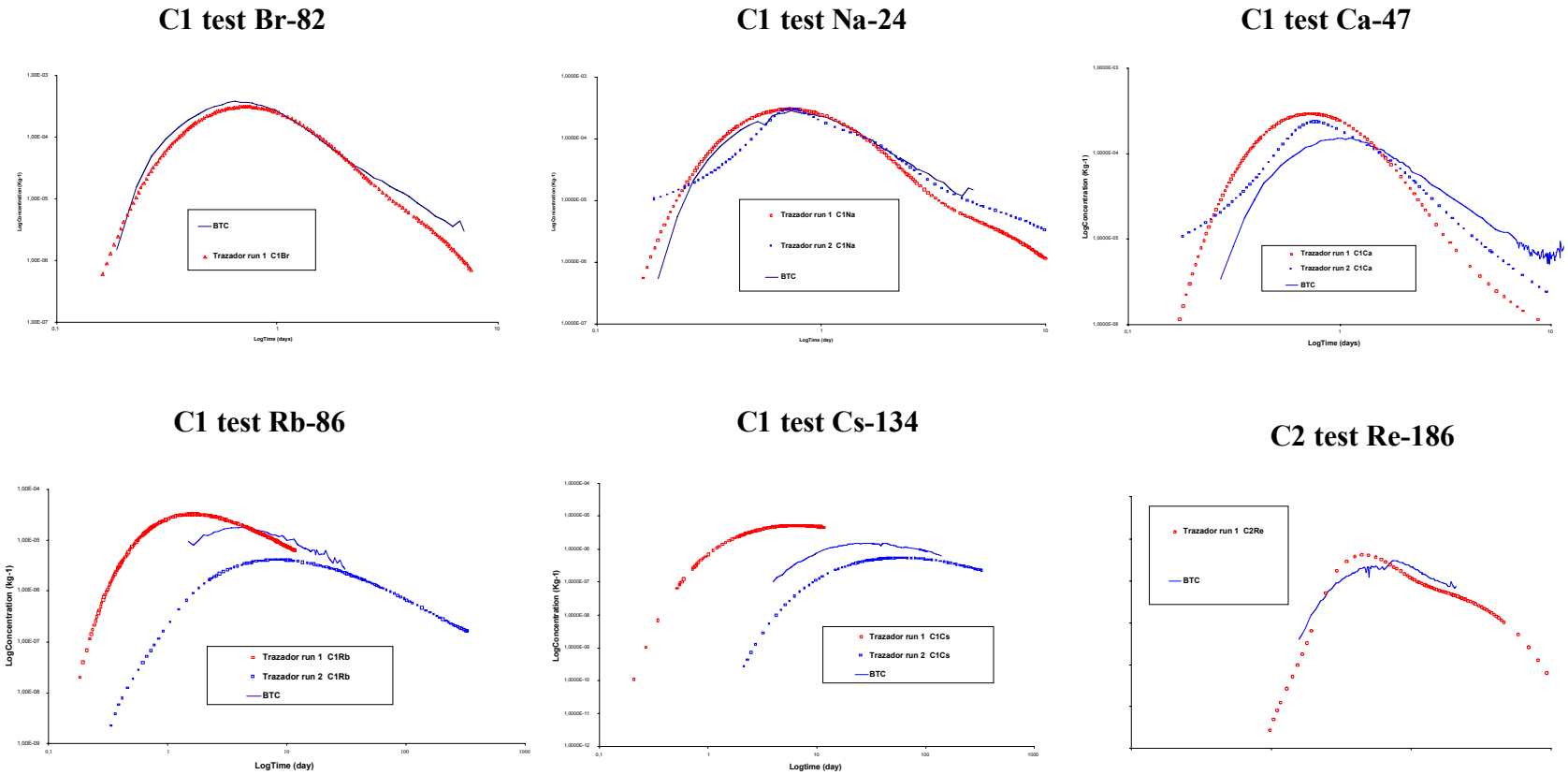

Figure A6-1. *Tracer prediction results. Red circles are run 1, blue squares are run 2, and the continuous blue line is the measurements. Plots are log-time (log-days) versus log-concentratcion (log-Kg-l)*

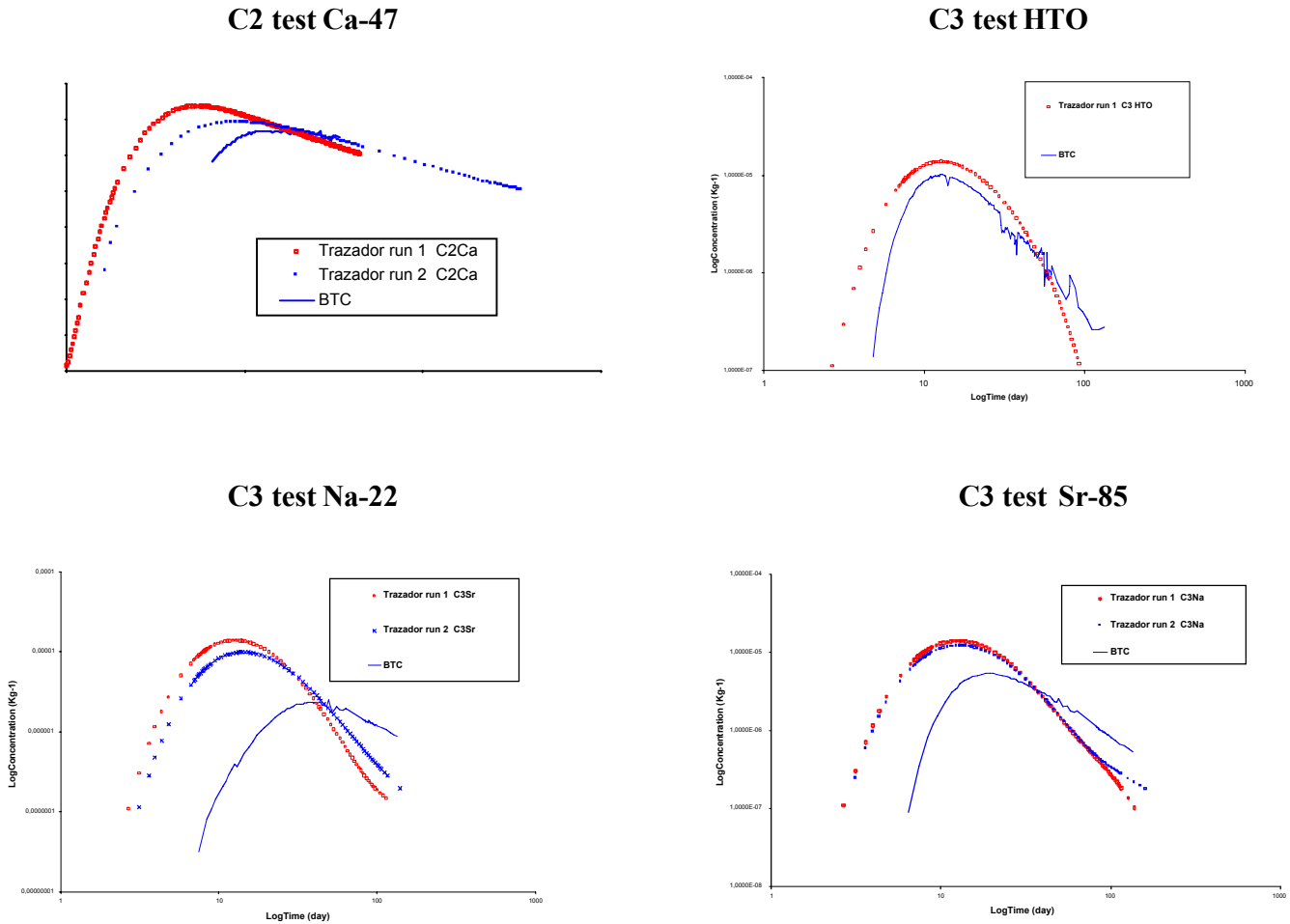

Figure A6-2. *Tracer prediction results. Red circles are run 1, blue squares are run 2 and continous blue line are measurements. Plots are log-time (log-day) versus log-concentration (log-Kg-1)*